ENHANCED GENERATION AND DETECTION OF ULTRAFAST LASER-INDUCED ACOUSTIC SIGNALS

The work described in this thesis was carried out at the Advanced Research Centre for Nanolithography (ARCNL), a public-private partnership between the University of Amsterdam (UvA), the Vrije Universiteit Amsterdam (VU), the Netherlands Organisation for Scientific Research (NWO) and the semiconductor equipment manufacturer ASML

UNIVERSITEIT VAN AMSTERDAM

The cover art was designed and hand painted by Fleur Kuijpers.

Enhanced generation and detection of ultrafast laser-induced acoustic signals

ACADEMISCH PROEFSCHRIFT

ter verkrijging van de graad van doctor
aan de Universiteit van Amsterdam
op gezag van de Rector Magnificus
prof. dr. ir. K.I.J. Maex
ten overstaan van een door het College voor Promoties ingestelde commissie,
in het openbaar te verdedigen in de Agnietenkapel
op vrijdag 28 januari 2022, te 16.00 uur

door Guido de Haan
geboren te Haarlemmermeer

Promotiecommissie

Promotor:	prof. dr. P.C.M. Planken	Universiteit van Amsterdam
Copromotor:	dr. R. Sprik	Universiteit van Amsterdam
Overige leden:	prof. dr. H.J. Bakker	Universiteit van Amsterdam
	prof. dr. ir. H.B. van Linden van den Heuvell	Universiteit van Amsterdam
	dr. E. van Heumen	Universiteit van Amsterdam
	dr. N.J. van Druten	Universiteit van Amsterdam
	dr. A.J.L. Adam	Technische Universiteit Delft
	prof. dr. I.D. Setija	Technische Universiteit Eindhoven

Faculteit der Natuurwetenschappen, Wiskunde en Informatica

Publications

This thesis is based on the following publications:

1 G. de Haan, V. Verrina, A. J. L. Adam, H. Zhang & P. C. M. Planken, *"Plasmonic enhancement of photoacoustic-induced reflection changes"*, Applied Optics, **60**(24), 7304-7313 (2021)

Presented in Chapter **4**.

2 G. de Haan, E. Abram, T. J. van den Hooven & P. C. M. Planken, *"Plasmonic enhancement of photoacoustic strain-waves on gold gratings"*, Submitted to AIP Advances (2021)

Presented in Chapter **5**.

3 G. de Haan, T. J. van den Hooven & P. C. M. Planken, *"Ultrafast laser-induced strain waves in thin ruthenium layers"*, Optics Express, **29**(20), 32051-32067 (2021)

Presented in Chapter **6**.

4 G. de Haan, J. Hernandez-Rueda & P. C. M. Planken, *"Femtosecond time-resolved pump-probe measurements on percolating gold in the ablation regime"*, Optics Express, **28**(8), 12093-12107 (2020)

Presented in Chapter **7**.

Abbreviations

The following table describes all the abbreviations used in this thesis.

Abbreviation	Meaning
AFM	Atomic Force Microscopy
Ar	Argon
Au	Gold
BBO	β-Barium-Borate
BD	Beamdump
BS	Beamsplitter
CD	Critical Dimension
CO_2	Carbion dioxide
CW	Continuous Wave
DOS	Density of States
DUV	Deep Ultraviolet
EUV	Extreme Ultraviolet
FWHM	Full Width at Half Maximum
FFT	Fast Fourier Transform
IC	Integrated Circuit
IR	Infrared
LW	Longitudinal Wave
NA	Numerical Aperture
NM	Grating Line Quasi-Normal Mode
OPA	Optical Parametric Amplifier
PGA	Phase Grating Alignment
QCM	Quartz Crystal Monitor
Ru	Ruthenium

continued on next page

Abbreviation	**Meaning**
SAW	Surface Acoustic Wave
SDG	Synchronous Delay Generator
SEM	Scanning Electron Microscopy
Si	Silicon
SiO_x	Silicon Oxide
Sn	Tin
SPP	Surface Plasmon Polariton
SPR	Surface Plasmon Resonance
SSD	Solid State Drives
TTM	Two-Temperature model
UV	Ultraviolet
WLC	White Light Continuum

Contents

1 Introduction

1.1 Nanolithography

Computer chips, or integrated circuits (IC's), are getting more advanced by the year. Recently, in a press release, Apple Inc. claimed to have fabricated the first commercially available personal computer chip with features as small as 5 nm, enabling them to print 16 billion transistors on one single computer chip [1]. This so-called M1-chip is fabricated by TSMC using new, high-precision nanolithography tools, developed by ASML [2]. As computer chips become more and more complex and as storage density increases, the semiconductor manufacturing industry is always pushing to print smaller structures.

In 1965 the co-founder of Intel, Gordon Moore, predicted that the number of transistors on a single computer chip would double every year [3]. Ten years later, in 1975, he revised his prediction by stating that the number of transistors on a single computer chip would double every two years [4]. This empirical observation is known as Moore's law and its validity is shown in Fig. 1.1.

In order to keep fulfilling Moore's Law, IC's need to get even smaller. These IC's are made using the process of optical nanolithography [5]. In nanolithography, light is used to transfer a pattern from a mask, or reticle, to a wafer. The mask acts as a blueprint of the structure which needs to be printed on the wafer. The pattern which is imprinted onto the wafer is a copy of the pattern on the mask scaled down by a factor of 4 [6]. The wafer is usually made of the semiconductor

material silicon. A schematic depiction of the sequential steps that make up the lithography process is shown in Fig. 1.2. First, a material sensitive to light, called a photoresist, is spin-coated on a Si-wafer. Afterward, light exposes the photoresist through a mask. The parts of the photoresist that are illuminated undergo a change in solubility, whereas the unexposed parts remain unaltered. The next step in the photolithographic process is called development. Here, the manufacturer can choose to either remove the exposed part or the unexposed part of the photoresist, depending on the type of photoresist that is used. If the manufacturer uses a so-called "positive photoresist", the parts of the photoresist which were exposed to the UV-light become *soluble* to the photoresist developer. If the manufacturer used a "negative photoresist", the parts of the photoresist which were exposed to the UV-light become *insoluble* to the photoresist developer.

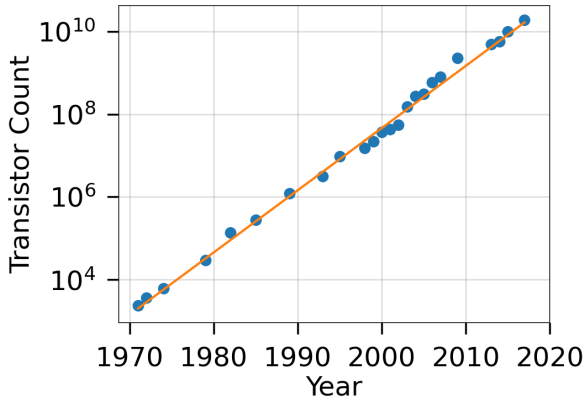

Figure 1.1: Number of transistors per microprocessor as a function of time from 1971 to 2017, demonstrating the validity of Moore's Law. Data taken from [7].

Next, the pattern of the photoresist is transferred to the material below via etching, where etching agents remove parts of the thin film which are no longer protected by the photoresist [8]. The type of material depends on the final product and can be an insulator, semiconductor, or conductor and is chosen by the manufacturer [9].

Once the pattern has been transferred from the mask to the photoresist, the sample has to be prepared for the next layer. The wafer is taken out of the lithography machine and the remaining parts of the photoresist are chemically removed. It then undergoes several processing steps such as layer deposition, etching, polishing, and ion implantation before it returns to the nanolithography machine for the next

lithography step [8]. For this, a new photoresist layer is spin-coated on the wafer before it re-enters the lithography machine where it undergoes the same steps as depicted in Fig. 1.2. This entire process is repeated many times to create computer chips or memory chips.

The smallest feature size which can be printed on a wafer is called the critical dimension (CD). The CD is therefore a measure of the printing resolution and is determined by the Rayleigh criterion [5], which, applied to nanolithography is,

$$CD = k_1 \frac{\lambda}{\mathrm{NA}}, \tag{1.1}$$

where λ is the wavelength used for the exposure, NA the numerical aperture of the optical system, and k_1 a constant related to lithographic processing variables such as the choice of the mask and the photoresist. From Eq. 1.1 it is clear that the CD can be minimized by either decreasing λ, by increasing the NA and by optimization of k_1. The value of k_1 has been minimized to approximately 0.25 [10].

The numerical aperture of any optical system is determined by the geometry of the focusing optics [11]. In some nanolithography systems, the NA has been increased to 1.35 using special immersion lenses [12]. Here, they place a liquid between the focusing optics and the wafer with a refractive index higher than 1, allowing for a numerical aperture greater than 1 [13].

The exposure wavelength λ has been decreased substantially since the beginning of nanolithography starting at 463 nm, reaching all the way down to the most common exposure wavelength today of 193 nm, which lies in the deep ultraviolet regime (DUV) of the electromagnetic spectrum [12, 14]. With an exposure wavelength of 193 nm and a numerical aperture of 1.35, this makes it possible to create structures with a CD of 38 nm [12].

In order to keep up with Moore's law, the semiconductor industry is making another step in decreasing the exposure wavelength, all the way from 193 nm (DUV) to 13.5 nm, which lies in the extreme ultraviolet regime (EUV). This exotic wavelength of 13.5 nm is generated from a highly excited Sn plasma [15–18]. The Sn plasma is generated by illuminating liquid Sn droplets with an extremely high intensity CO_2 laser [19]. The reduced exposure wavelength of 13.5 nm, combined with a numerical aperture of 0.33 allows the production of 7 nm features [20], or even smaller [21].

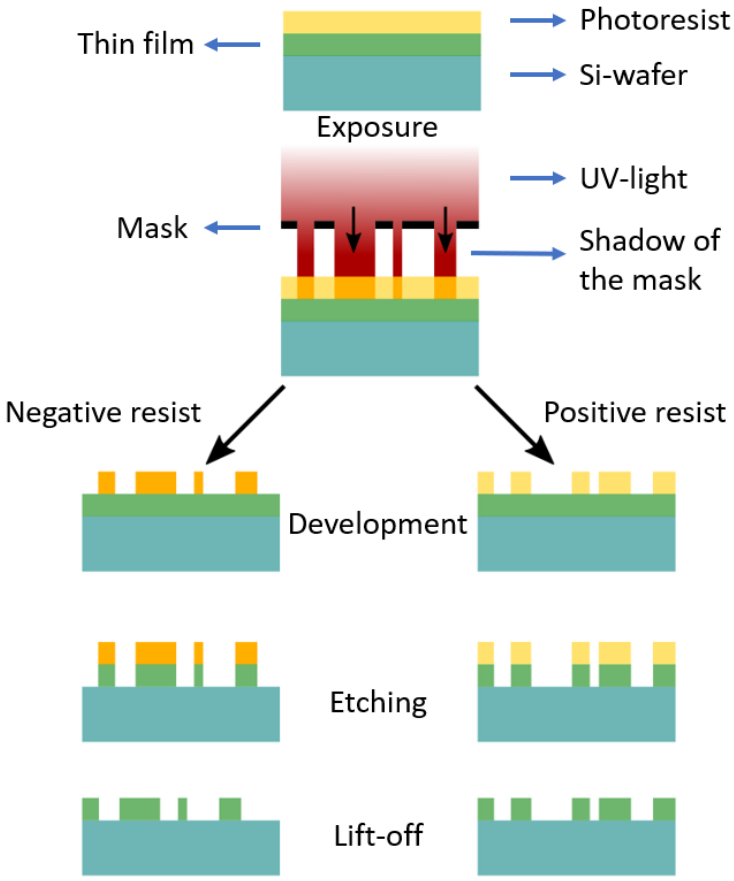

Figure 1.2: Schematic illustration of the steps required in a photolithographic process.

1.2 Metrology and signal strength

To decrease the feature sizes further, chip manufactures have devised ways to stack multiple structured layers on top of each other [22], creating three-dimensional computer chips. An example of a 3D chip is the 3D-NAND flash memory, which is a crucial component for modern-day Solid State Drives (SSD). In such a 3D stack, vertical interconnects are manufactured to ensure inter-layer communication. However, due to the many steps taking place in the lithographic process, the vertical interconnect is manufactured layer by layer, see Fig. 1.3. It is of crucial importance for the functionality of the 3D stack, that the vertical interconnect is not interrupted (Fig. 1.3). This requires that each layer is positioned exactly

above the layer below.

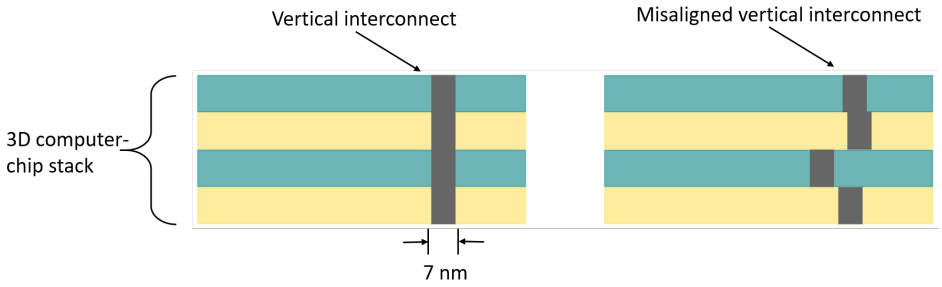

Figure 1.3: Schematic depiction of the side view of a layer stack. Here we show the importance of correct alignment of each layer on top of the one below for the fabrication of a functioning vertical interconnect.

As mentioned before, the wafer is removed from the lithography machine after a layer has been printed to undergo further processing. After this, it re-enters the lithography machine to define the next layer. In order to ensure that the vertical interconnects printed on the top layer align correctly with the vertical interconnects of the layer below, it is crucial that the wafer is placed in the exact same orientation/position with respect to the exposure beam as with the previous layer. To ensure correct alignment of the wafer, accurate positioning of the wafer is necessary on a (sub)-nm scale.

To measure the wafer position, multiple (20-40) so-called "alignment markers" are printed on the wafer [6]. These alignment markers usually consist of a set of 4 gratings: two with the grating lines oriented along the X direction and two with the grating lines oriented along the Y direction. When the two gratings which are oriented in the same direction have a slightly different pitch, unambiguous determination of the marker position is possible using the Nonius principle [23]. To detect the gratings, the wafer is scanned laterally on a wafer-stage, relative to a metrology light source, which consists of multiple wavelength lasers [6]. When the light source strikes one of the gratings, the $+1^{\text{st}}$ and -1^{st} order diffracted beams are detected and interferometrically combined. When the alignment marker is scanned across the light source, a phase change occurs between the $+1^{\text{st}}$ and -1^{st} order diffracted beams. After interferometric re-combination of the diffracted orders, this phase can be recovered. It can be derived from the Fraunhofer diffraction equation that the phase change of one diffracted order $\Delta\phi$ is related to a shift of the grating position Δx by [24],

$$\Delta\phi = 2m\pi\frac{\Delta x}{d}, \tag{1.2}$$

where m is the diffracted order (+1, -1) and d is the grating pitch. A schematic drawing of the alignment sensor is shown in Fig. 1.4. After projecting the spatial interference pattern of the $+1^{st}$ and -1^{st} order diffracted beams on a reference grating, the transmitted light through this reference grating is measured as a function of wafer position. From the measured intensity of the light transmitted through the reference grating, the center position of the grating can be determined with a sub-nm accuracy [25]. This technique is called phase-grating alignment (PGA).

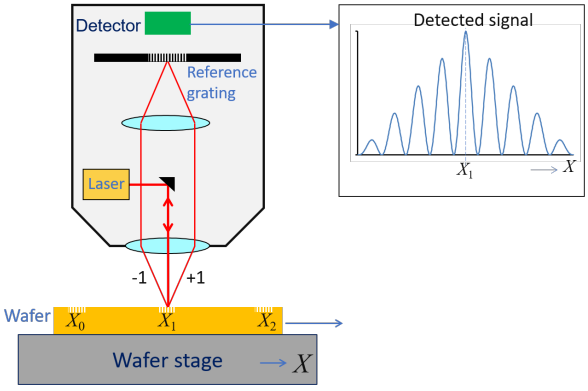

Figure 1.4: Schematic drawing of the alignment sensor used to align the wafer. The interference of the $+1^{st}$ and -1^{st} order diffracted beams is projected on a reference grating and the transmission of the grating is measured as a function of wafer position. This figure is based on figures from [6].

Using this technique, it is possible to achieve sub-nm accuracy with diffraction efficiencies as low as 10^{-5} [6]. One of the downsides of the PGA technique is that light has to be able to penetrate the layers in order to reach the alignment gratings and the diffracted light has to propagate back up through these layers to be detected. This puts a constraint on the types of materials the can be used during the lithographic process since they need to be optically transparent to detect the alignment markers [6]. This poses a challenge in nanolithography because, for example, on top of a 3D-NAND stack a thick opaque hard-mask layer is deposited to protect the patterns during the etching process. This means that the alignment markers can no longer easily be detected by the sensor.

Fortunately, materials which are opaque to light are often transparent to sound.

Therefore, it has been proposed to use laser-induced ultrasonic waves to detect the buried grating [26,27]. In Fig. 1.5 we show the different steps involved in this process.

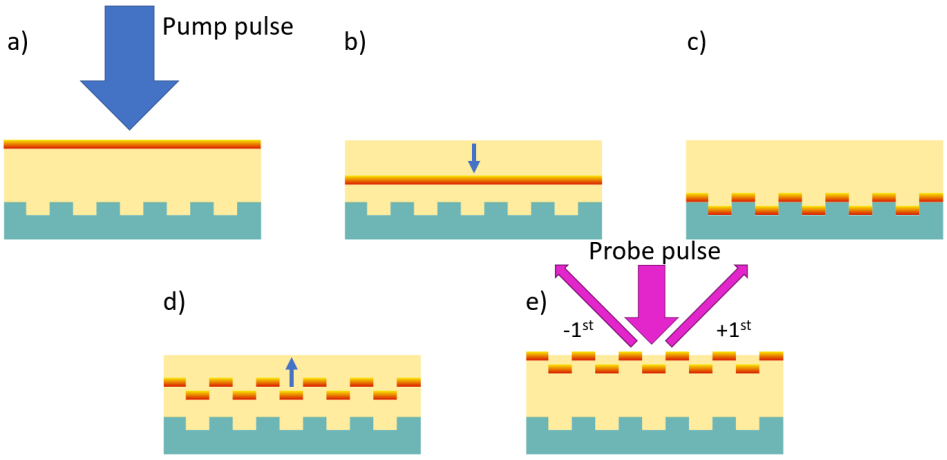

Figure 1.5: (a) Excitation and rapid heating of the surface layer by a femtosecond pulse, causing a strain wave to form. (b) Propagation of the strain wave to the buried grating. (c) Strain wave reflection from the buried grating. (d) Acoustic copy of the buried grating traveling to the surface. (e) Probe pulse diffraction from the acoustic grating-induced surface-displacement and/or changes in the optical constants.

When a strong femtosecond ultrafast laser pulse (pump pulse) is incident on a metallic layer, the free electron gas will absorb the energy and consequently heat up. The electron gas energy will diffuse deeper into the material while simultaneously converting to lattice heat through electron-phonon coupling. The depth and speed of the lattice heating depend on the material parameters, as will be discussed more in chapter 2. The rapid heating of the lattice sets up a thermal stress inside the material (a), which generates a traveling strain wave (acoustic wave). This strain wave will propagate through the entire layer with a flat wavefront (b). When the acoustic wave reaches the buried grating, the acoustic wavefront will acquire the shape of the buried grating, essentially transforming the acoustic wave into an "acoustic replica" of the buried grating (c). This acoustic copy will then travel back towards the surface where it will physically deform the surface and change the permittivity of the material, both in a spatially periodic manner (d). The resulting grating can then be detected via diffraction of a second, weak, optical pulse (probe pulse) (e).

It has been shown that laser-induced acoustic waves can be used to detect buried

gratings underneath several layers of metals and dielectrics [28]. This technique even works with buried gratings with a sub-nm amplitude [29] and duty cycles as low as 1 % [30]. However, the diffraction efficiency of light diffracted off the acoustic wave reflected by the buried gratings is usually smaller than about 10^{-8}, which is not sufficient for industrial applications. Therefore, in this thesis, we report on techniques to enhance the generation and detection of laser-induced acoustic waves for the detection of buried gratings.

1.3 Thesis outline

This thesis focuses mostly on techniques that can potentially enhance the generation and detection of laser-induced ultrasonic waves.

Chapter 2 describes the theory required to understand the generation of laser-induced acoustic waves. We start with an explanation of the two-temperature model, which describes the thermal response of metals after irradiation with an ultrashort laser pulse. Afterward, in order to apply the two-temperature model to extremely thin layers, we describe the absorption of the incident light using a three-layer model. This is followed by a brief description of how a thermal distribution in a metal layer converts to a time-dependent thermal stress, which launches a strain wave. Finally, we finish with the theory behind surface plasmon polaritons (SPPs) and the resonant conditions required to launch them. An understanding of SPPs is required since, in the context of this thesis, they are used to enhance the detection and generation of acoustic waves.

In Chapter 3, we discuss the experimental methods used in the work described in this thesis. A detailed description of the optical equipment used, such as the ultrafast amplified femtosecond laser and the optical parametric amplifier, is given. This is followed by an explanation of the optical pump-probe measurement technique, which is used in the optical experiments described in this thesis. The generation of a transient-grating by crossing two laser beams is discussed, accompanied by a discussion on laser-induced reflection and diffraction changes. Moreover, the techniques used to manufacture and characterize the samples are described, such as thin-layer deposition and scanning electron microscopy, atomic force microscopy, and ellipsometry.

In Chapter 4, we show surface plasmon resonance (SPR) enhancement of acoustic-wave-induced reflection changes. A grating structure is illuminated with a strong pump pulse, which generates multiple types of acoustic waves, such as longitudinal waves, surface acoustic waves, and grating line normal modes. All of these acoustic waves locally change the density of the material, which directly influences the surface plasmon resonance conditions. Furthermore, we speculate that the ampli-

tude of the grating lines is altered by the acoustic waves, which also changes the SPP resonance conditions. In doing so, we measure an enhancement of the surface acoustic wave-induced reflection changes when measuring *on* the resonance and an enhancement of the optical reflection changes caused by other acoustic modes, on the *slopes* of the resonance.

In Chapter 5, we show efficient excitation of ultrasonic strain waves on a gold grating by using surface plasmon polaritons to enhance the coupling of the light to the grating. We measure strain-wave-induced reflection changes of up to 0.7 %, using a 400 nm central wavelength probe beam. We demonstrate that the magnitude of the reflection changes scale quadratically with the pump fluence. We tentatively attribute this to non-linear changes in the interband transition energy as a function of strain via strain-induced changes to the band structure. Using a model which describes the frequency-dependent permittivity of gold as a function of interband transition energy, we show that, to account for our measured signal strength, the interband transition energy of 2.47 eV would have to change by only 0.013 eV.

In Chapter 6, we describe the generation of extremely high-frequency acoustic waves in ultrathin ruthenium layers. We demonstrate that in ruthenium, the optical response is mostly governed by the thermo-optic and strain-optic effects. We show that in the first 2 ps after optical excitation the phase/frequency of the acoustic wave changes. This is attributed to a possible temperature dependence of the mechanical properties of ruthenium. This is supported by the fact that in the first 2 ps after excitation, the lattice temperature reaches near-melting point temperatures. Furthermore, we demonstrate that, for ultrathin layers, the speed of sound is strongly dependent on the layer thickness.

In Chapter 7, we show time-dependent measurements on nanostructured gold in the ablation regime. To launch acoustic waves with a higher amplitude, one can simply increase the power of the pump beam. However, at a certain point, the optical power is sufficient to cause damage. Therefore, in this chapter, we study the damage mechanism of high-power femtosecond laser pulses on nano-structured gold. We show how different excitation energies lead to a different optical response and a post-mortem analysis of the resulting damage using Scanning Electron Microscopy (SEM) is also shown. We show that, for the highest excitation energies, both reflection and transmission of the sample approach the substrate values within 150 ps, suggesting that the thin gold layer completely vaporizes within this timescale. This is supported by calculations that show that the absorbed energy exceeds the cohesive energy of the gold.

2 Theory

In this chapter we will discuss the physical principles behind laser-induced ultrasonics. We will first discuss what happens when a metal absorbs a high-intensity ultrafast laser pulse, using the Two-Temperature model (TTM). Afterward, we will show how the temperature distribution generates thermal stress, which leads to the generation of a strain wave. This strain wave, or acoustic wave, usually has a high frequency in the order of several GHz to hundreds of GHz. These types of laser-induced acoustic waves are used for many applications in both science and industry [26, 30–48]. Furthermore, we will discuss the excitation of a surface plasmon polariton, which is the coupling of an electromagnetic wave to oscillations of the free electron gas near the surface of a metal.

2.1 Two-Temperature Model

When a laser pulse is incident on a metal surface, the intensity distribution inside the metal layer will decrease exponentially as a function of the depth z in the metal and can be described by,

$$I(z,t) = (1-R)I_0(z,t)e^{-z/d_p}, \tag{2.1}$$

where z is the depth inside the material as defined in Fig. 2.1, R is the power reflection coefficient of the metal and d_p is the optical penetration depth. The optical penetration depth is defined as the depth at which the intensity has decreased to a value of 1/e of the value at the surface. Since optical reflections of the metal/substrate interface are not taken into account, the relation for the intensity as given in Eq. (2.1) is only valid when the layer thickness significantly exceeds the penetration depth.

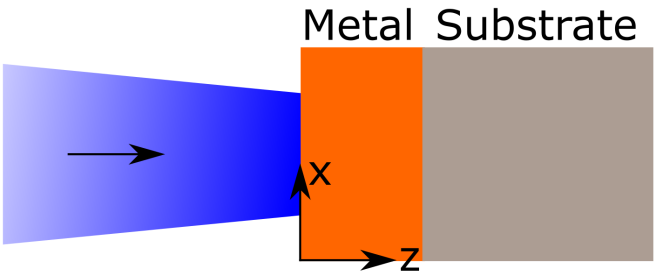

Figure 2.1: Schematic depiction of the metal on the substrate. We define $z = 0$ at the metal/air interface. The laser pulse is incident on the metal from the left.

The energy of the laser pulse is initially absorbed by the free electron gas of the metal. The electron gas energy will diffuse deeper into the metal, while simultaneously transferring the energy to the lattice via the emission of phonons. The electron-phonon coupling constant determines how fast the transfer of energy from the electron gas to the lattice occurs, and it is a characteristic parameter for every metal. The process of the absorption of the laser by the free electrons, transfer of energy to lattice, and consequently heating of the lattice, is described by the two-temperature model [49–52].

The TTM is a widely used phenomenological model based on the separation of two subsystems: the electrons and the lattice, both of which are assigned a separate

temperature, the electron temperature T_e and the lattice temperature T_l. The TTM works if the statistical thermal distribution for both the electron gas and the lattice follows a Fermi and Bose-Einstein distribution, respectively. However, although the model assumes that the thermodynamics of both the electron gas and the lattice can be described by a thermal distribution, the model allows for both to have different temperatures. The TTM thus describes the time evolution of the position-dependent lattice and electron temperatures. It is known that directly after absorption of a high-intensity laser pulse, the electron temperature is not well-defined [34, 53]. However, for most metals, after approximately 500 fs or sooner, the electron system has thermalized via electron-electron scattering and, hence, the TTM is useful to describe the evolution of the electron and lattice temperatures after these times. Under the assumption that we can neglect lateral diffusion of energy caused by in-plane temperature gradients (which are usually small), we can write down the temporal en spatial evolution of the electron and lattice temperature in one dimension as,

$$C_e(T_e)\frac{\partial T_e}{\partial t} = \frac{\partial}{\partial z}\left(k_e(T_e, T_l)\frac{\partial T_e}{\partial z}\right) - g(T_e - T_l) + S(z,t), \tag{2.2}$$

$$C_l\frac{\partial T_l}{\partial t} = g(T_e - T_l), \tag{2.3}$$

where C_e and C_l are the electron and lattice heat capacities, k_e is the electron thermal conductivity, g the electron-phonon coupling constant, and S the laser source term defined by $S(z,t) = \alpha I(z,t)$, where α is the inverse of the optical penetration depth. Unit analysis of the left-hand side of the equation shows that all terms in Eqs. (2.2) and (2.3) have the unit of $\mathrm{W/m^3}$. They thus represent the rate at which energy appears and disappears per unit of volume for the electron gas and the lattice. For example, for Eq. (2.2), the first term on the right-hand side of the equal sign describes electron gas energy loss/gain by thermal diffusion. The second term describes energy loss by energy transfer to the lattice via electron-phonon coupling, and the third term describes electron gas energy gain from a source term which, in our case, is a laser pulse.

We can numerically solve Eqs. (2.2) and (2.3) using the temperature-dependent approximations for the electronic heat capacity and electron gas thermal conductivity given by $C_e = A_e T_e$ and $k_e = k_0 T_e/T_l$, where A_e and k_0 are the electron gas specific heat constant and the electron gas thermal conductivity at 273 K, respectively [52, 54]. Typically, for metals, the electron gas heat capacity at room temperature is a lot smaller than the lattice heat capacity. This means that, often, in the first few picoseconds after excitation, electron temperatures can strongly

exceed lattice temperatures. Furthermore, when simulating the electron gas and lattice temperature distributions in multi-layer samples, a spatial change of the electron gas thermal conductivity k_0 has to be taken into account at the transition from one layer to another.

2.2 Three-layer model

As already mentioned in section 2.1, it is not valid to use Eq. (2.1) to describe the intensity distribution in a metal layer where the thickness d is smaller than the optical penetration depth d_p. This is because for optically thin layers multiple reflections inside the layer, as well as transmission of light into the substrate, must be taken into account. To determine the intensity distribution in such a layer we use a different model, the three-layer model. The physical geometry to which this model applies is shown in Fig. 2.2, where we have three materials stacked on top of each other, each with their own (possibly complex) dielectric function ϵ_i (i = 1,2,3).

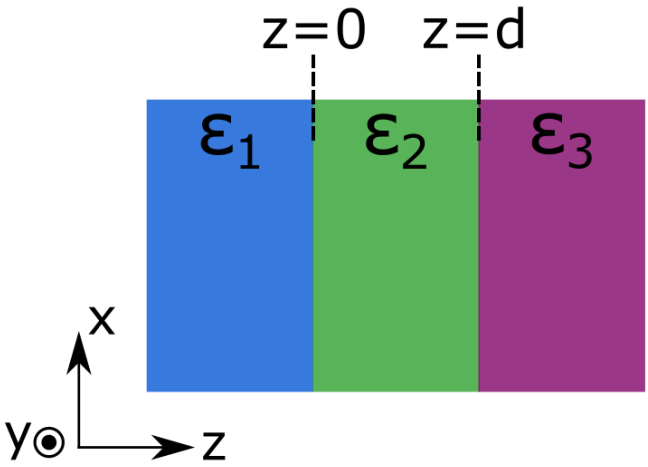

Figure 2.2: Schematic depiction of the three layers and their corresponding dielectric functions ϵ_i (i = 1, 2, 3).

In this model layer 1 and layer 3 extend to $-\infty$ and $+\infty$ in the z-direction, respectively. All layers extend infinitely in the x-y plane. Consider now a continuous electromagnetic plane wave propagating from z = $-\infty$ to z = $+\infty$ with the electric field polarized in the x-direction. At each interface in our 3-layer geometry, the wave will partially reflect off the interface and partially transmit through the interface. The reflected and transmitted parts of the electromagnetic wave will again reflect off and transmit through any interface they encounter, and so on and

so forth. This leads to a superposition of infinitely many waves within our 3 layers. We can write down the equations for the sum of all these waves in the three layers by simply using the fact that each medium allows only the presence of two wave vectors, one propagating to the left and one propagating to the right,

$$E(z) = E_0 \begin{cases} (e^{ik_1 z} + re^{-ik_1 z})\hat{\mathbf{x}}, & z < 0 \\ (ae^{ik_2 z} + be^{-ik_2 z})\hat{\mathbf{x}}, & 0 < z < d \\ te^{ik_3(z-d)}\hat{\mathbf{x}}, & d < z. \end{cases} \tag{2.4}$$

In this format r (reflection), a, b, and t (transmission) are complex numbers, and $k_i = n_i\omega/c$. Furthermore, we can calculate the absolute reflection into medium 1 and transmission into medium 3 using,

$$R = |r|^2, \tag{2.5}$$

$$T = \frac{k_3}{k_1}|t|^2. \tag{2.6}$$

Note that r and t are the reflection and transmission coefficients of the system of the metal and substrate that take all the reflections and transmissions into account. These are therefore *not* to be confused with the single-interface Fresnel coefficients.

Using Maxwell's equations to derive boundary conditions for the electric and magnetic field we find:

$$1 + r = a + b \tag{2.7}$$

$$ae^{ik_2 d} + be^{-ik_2 d} = t \tag{2.8}$$

$$k_1(1 - r) = k_2(a - b) \tag{2.9}$$

$$k_2\left(ae^{ik_2 d} - be^{-ik_2 d}\right) = k_3 t. \tag{2.10}$$

Here we have four equations with four unknowns, which allows us to solve this

system of equations. In doing so we obtain:

$$r = \frac{p^{-1}(k_1 - k_2) - p(k_1 + k_2) + 2k_2 t}{p^{-1}(k_1 + k_2) - p(k_1 - k_2)}, \tag{2.11}$$

$$a = \frac{2k_1 p^{-1} - (k_1 - k_2)t}{p^{-1}(k_1 + k_2) - p(k_1 - k_2)}, \tag{2.12}$$

$$b = \frac{(k_1 + k_2)t - 2k_1 p}{p^{-1}(k_1 + k_2) - p(k_1 - k_2)}, \tag{2.13}$$

$$t = \frac{4k_1 k_2}{p^{-1}(k_1 + k_2)(k_2 + k_3) - p(k_1 - k_2)(k_3 - k_2)}, \tag{2.14}$$

where we have introduced the factor $p = e^{ik_2 d}$ for brevity. If we know the complex refractive indices for all three layers we can calculate the electric field everywhere inside our layers. Furthermore, by using Maxwell's equations we can derive the magnetic field $B(z)$ as well. If we have both $E(z)$ and $B(z)$ we can determine the intensity distribution in our 3-layer system by calculating the Poynting vector:

$$\vec{S} = \frac{1}{\mu_0} \vec{E}(z) \times \vec{B}(z), \tag{2.15}$$

where μ_0 is the magnetic permeability of vacuum. From this we can calculate the time average (over one oscillation period) of the Poynting vector, which gives us the intensity, $I \equiv \langle S \rangle$ [55]. Here, $\langle\rangle$ denotes the time average over a single cycle. Thus, we find that the intensity distribution in a three layer system is given by:

$$\left\langle \vec{S} \right\rangle = \frac{E_0^2 \hat{\mathbf{z}}}{2\omega\mu_0} \begin{cases} \mathrm{Re}\left\{k_1 \left(1 - |r|^2 - r^* e^{2ik_1 z} + r e^{-2ik_1 z}\right)\right\}, & z < 0 \\ \mathrm{Re}\left\{k_2^* \left(|a|^2 e^{-2\mathrm{Im}\{k_2\}z} - ab^* e^{2i\mathrm{Re}\{k_2\}z} \right.\right. & \\ \left.\left. + a^* b e^{-2i\mathrm{Re}\{k_2\}z} - |b|^2 e^{2\mathrm{Im}\{k_2\}z}\right)\right\}, & 0 < z < d \\ \mathrm{Re}\left\{k_3^* |t|^2 e^{-2\mathrm{Im}\{k_3\}(z-d)}\right\}, & d < z. \end{cases} \tag{2.16}$$

Here we have assumed that $\mathrm{Im}\{k_1\} = 0$. Since in all scenarios described in this thesis layer 1 is air, this assumption is valid.

In order to use the three-layer model as a source term for the TTM, we need to calculate the amount of absorbed energy per unit volume per unit time. Using Poynting's Theorem we can write [56]

$$\frac{\partial u}{\partial t} = -\vec{\nabla} \cdot \left\langle \vec{S} \right\rangle, \tag{2.17}$$

where u is the energy density in the material. Solving Eq. (2.17) we find

$$-\vec{\nabla}\cdot\left\langle \vec{S} \right\rangle = \frac{E_0^2}{2\omega\mu_0} \begin{cases} 0, & z < 0 \\ 2\mathrm{Re}\left\{ k_2^* \left[\mathrm{Im}\{k_2\} \left(|a|^2 e^{-2\mathrm{Im}\{k_2\}z} + |b|^2 e^{2\mathrm{Im}\{k_2\}z} \right) \right.\right. & \\ \left.\left. + \, i\mathrm{Re}\{k_2\} \left(ab^* e^{2i\mathrm{Re}\{k_2\}z} + a^* b e^{-2i\mathrm{Re}\{k_2\}z} \right) \right] \right\}, & 0 < z < d \\ 2\mathrm{Im}\{k_3\}\mathrm{Re}\left\{ k_3^* |t|^2 e^{-2\mathrm{Im}\{k_3\}(z-d)} \right\}, & d < z. \end{cases} \tag{2.18}$$

We can now use Eq. (2.17) combined with Eq. (2.18) as our source term $S(z,t)$ in Eq. (2.2). However, the calculation up until this point has not taken the temporal pulse shape into account. We can correct for this by multiplying with a Gaussian envelope:

$$S(z,t) = \frac{1}{\sqrt{\pi}\tau} \exp\left[-\left(\frac{t - t_0}{\tau} \right)^2 \right] \frac{\partial u}{\partial t}. \tag{2.19}$$

Note that in Eq. (2.18), the absorbed power in the substrate becomes zero when the substrate is made of glass, for which $\mathrm{Im}\{k_3\} = 0$.

2.3 Generation of laser-induced acoustic waves in metals

Depending on the material parameters, the TTM can give quite different results for the lattice temperature distribution. The two parameters with the most influence on the lattice temperature distribution are the electron-phonon coupling constant g and the electron gas thermal conductivity k_e. In Fig. 2.3 we show the calculated temperature distributions for two different metal layers. In (a) we show the lattice temperature distribution for Ruthenium and in (b) for Gold. For both metals, we used a layer thickness of 40 nm. On the horizontal axis we show the depth inside the sample in nm and on the vertical axis we show the time in ps. The material parameters used in these TTM calculations are given in table 2.1. The source term is a laser pulse, with a central wavelength of 400 nm, a pulse length of 50 fs, and a fluence of 1.02×10^{-2} J/cm^2.

	Ru	*Au*
n	$2.98^{(a)}$	$1.46^{(b)}$
k	$5.68^{(a)}$	$1.95^{(b)}$
A_e ($\mathrm{Jm^{-3}K^{-2}}$)	$385^{(c)}$	$71^{(d)}$
k_0 ($\mathrm{Wm^{-1}K^{-1}}$)	$117^{(c)}$	$318^{(d)}$
g ($10^{16}\mathrm{Wm^{-3}K^{-1}}$)	$185^{(c)}$	$2.1^{(d)}$
C_l ($10^{6}\mathrm{Jm^{-3}K^{-1}}$)	$2.95^{(c)}$	$2.51^{(d)}$

Table 2.1: Material parameters used in the TTM calculations. (a) Measured using ellipsometry; (b) Ref. [57]; (c) Ref. [58]; (d) Ref. [52].

In Fig. 2.3(a) we have a material (Ru) with a *strong* electron-phonon coupling constant combined with a *low* electron gas thermal conductivity. The strong electron-phonon coupling results in a quick transfer of energy from the electrons to the lattice. Combined with the fact that the electrons do not diffuse far into the material due to the low electron gas thermal conductivity, this results in a high lattice temperature localized near the surface of the material after approximately 2 ps. In Fig. 2.3(b) we have a material (Au) with a *weak* electron-phonon coupling constant combined with a *high* electron gas thermal conductivity. Here, we see a very different lattice temperature distribution. Due to the slow transfer of energy from the electrons to the lattice, combined with the rapid diffusion of the electron gas energy into the material, we get a homogeneous lattice temperature throughout the sample. Furthermore, the lattice reaches its final temperature only after roughly 10 ps, much slower than in the case of Ru.

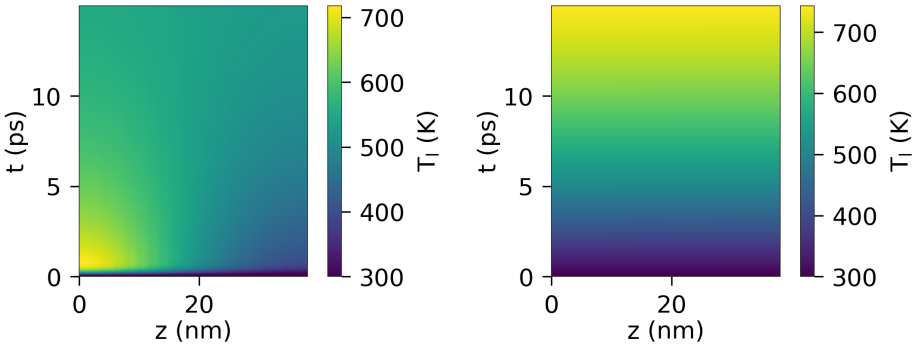

(a) (b)

Figure 2.3: Here we show the lattice temperature distribution of two different metals, calculated using the TTM. In panel (a) we used ruthenium, which has a strong electron-phonon coupling constant and a low electron gas thermal conductivity. In panel (b) we used gold, which has a low electron-phonon coupling constant and a high electron gas thermal conductivity.

This difference in temperature distribution can translate into a different temporal shape of the generated acoustic wave. The lattice temperature generates a thermal stress, given by [59, 60],

$$\sigma_z^{th}(z,t) = -3B\beta\Delta T(z,t), \tag{2.20}$$

where B is the bulk modulus and β the linear expansion coefficient. The generated stress will be either localized or homogeneously distributed throughout the sample, depending on the lattice temperature distribution.

The thermal stress will launch a strain wave that will travel through the material. Depending on the lattice temperature distribution, the strain wave will be either a traveling wave or a standing wave. If the lattice temperature is confined to a thin surface layer, such as in Fig. 2.3(a), the thermal stress will be localized as well, resulting in the excitation of a traveling strain wave. However, if the lattice temperature is distributed homogeneously throughout the layer, as in Fig. 2.3(b), the thermal stress will be homogeneously distributed throughout the layer. This will result in a standing strain wave, which behaves more like a breathing mode of the entire layer [59].

We can calculate the spatial and temporal profile of the strain wave, following the

derivation of Thomsen et. al. [60]. We numerically solve the equations of elasticity in the z-direction,

$$\begin{aligned} s_z(z,t) &= \frac{\partial u(z,t)}{\partial z}, \\ \sigma_z(z,t) &= \sigma_{str} + \sigma_z^{th} \\ &= (\lambda + 2\mu) s_z(z,t) - 3B\beta\Delta T_l(z,t), \\ \rho \frac{\partial^2 u(z,t)}{\partial z^2} &= \frac{\partial \sigma_z(z,t)}{\partial t}, \end{aligned} \tag{2.21}$$

where $s_z(z,t)$ is the strain, σ_z is the total stress, which is the sum of the thermal stress σ_z^{th} and the stress induced by the strain wave σ_{str}, λ and μ are the Lamé parameters, u is the displacement and ρ is the density of the material.

The model presented in Eq. (2.21) to calculate laser-induced strain waves takes into account only strain generated in the z-direction, which is in a direction perpendicular to the surface of the sample. However, if a surface structure is present, or if the excitation profile is periodic in space, it is possible to set up a thermal stress which has components parallel to the surface [59, 61–64]. Similarly as before, the time-dependent stress launches a strain wave that travels parallel to the surface. Such an acoustic wave, with components parallel to the surface, is commonly referred to as a surface acoustic wave (SAW). Depending on the excitation conditions and the material parameters, the properties of the surface wave can be different [62, 65]. When a SAW is launched via excitation of a periodic surface structure or by employing a periodic excitation profile, the SAW will most likely have the same periodicity as the surface profile [45, 66]. In this thesis, SAWs were generated via the excitation of a physical grating present on the surface of the sample.

2.4 Surface Plasmon Polaritons

A surface plasmon polariton (SPP) is an excitation where an incident electromagnetic wave couples to the free electron gas of a metal, propagating along the metal-dielectric interface. The free electrons will oscillate with the EM field, giving rise to surface charge density oscillations. These surface charge density oscillations are thus coupled to an electromagnetic field with a weak x-component, but with a strong z-component which decays exponentially into the metal and the dielectric. A schematic illustration of an SPP and its decaying electric field is shown in Fig.

2.4.

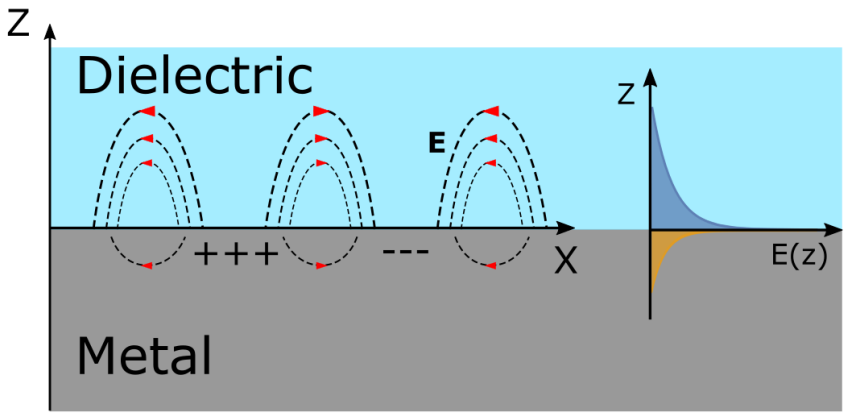

Figure 2.4: Schematic of an SPP excited at a dielectric/metal interface. Electric field lines are shown on the left and the evanescent electric field in the z-direction in the dielectric and in the metal is shown on the right.

The dispersion relation of an SPP can be derived directly from Maxwell's equations [67] and is given by,

$$k_{SPP} = \frac{\omega}{c}\sqrt{\frac{\epsilon_m \epsilon_d}{\epsilon_m + \epsilon_d}}, \tag{2.22}$$

where ω is the angular frequency of the incident light, c the speed of light, and ϵ_m and ϵ_d the dielectric constants of the metal and dielectric, respectively. If we plug in the numbers for the dielectric functions of typical metals and dielectrics, we find that the square root in Eq. (2.22) is always bigger than 1 and thus $k_{spp} > k_0$, this is also illustrated in Fig. 2.5 where we plot the typical dispersion relation of an SPP.

Therefore, if we want to overcome the momentum mismatch between the incident light and the SPP, we need to add an extra k-component to the k_x of the light. One way to do this is by employing a dielectric material that has a refractive index bigger than 1 by exciting the SPP from the glass side. Usually, a glass prism is used in the so-called Kretschmann or in the Otto configuration [67–70]. Another method to excite SPP's is by illuminating a grating [71, 72]. In doing so, we can add or subtract the grating k-vector k_g to the x-component of the incident light k-vector k_x, such that the magnitude of the sum or the difference of k_x and k_g equals the magnitude of the SPP k-vector. Thus we end up with:

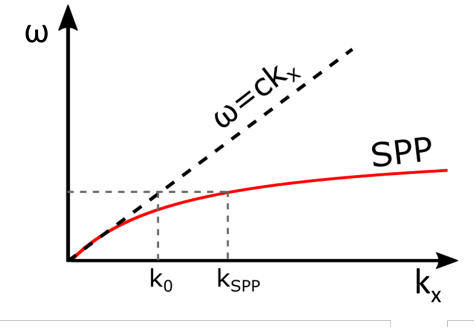

Figure 2.5: Dispersion relation of an SPP. The mismatch in momentum between incident light and the SPP of the same frequency is clearly visible.

$$|k_x \pm k_g| = k_{SPP}. \tag{2.23}$$

Here, $k_x = sin\ \theta\ \omega/c$ where θ is the angle of incidence and $k_g = 2\pi/\Lambda$, where Λ is the grating periodicity. Thus we obtain our SPP excitation condition as

$$\left|\frac{\omega}{c}\sin\theta \pm N\frac{2\pi}{\Lambda}\right| = \frac{\omega}{c}\sqrt{\frac{\epsilon_m\epsilon_d}{\epsilon_m+\epsilon_d}}, \tag{2.24}$$

where N is a positive integer, which, in the context of this thesis, equals 1. Due to the $\pm$ sign in Eq. (2.23), it is possible to, at a fixed angle θ, launch an SPP in the same direction as k_x, but also opposite to k_x, although this would require a different incident frequency.

When an SPP is efficiently launched, energy is transferred from the incident light to the SPP, resulting in a decrease in the amount of reflected light. To identify the SPP resonance one can measure the reflectance spectrum of the grating using a spectrometer. A schematic depiction of the setup used to measure the reflectance spectrum of the SPP grating is shown in Fig. 2.6. A white light source produces divergent continuous-wave radiation with wavelengths ranging from 400 to 800 nm having a random polarization. The light is collimated using a lens and passes through a polarizer which changes the polarization of the light such that the electric field is initially parallel to the grating lines. The light then passes through a $\lambda/2$ plate, which can rotate the polarization of the light. Afterward, the beam is reflected off the plasmonic grating and the spectrum of the reflected light is measured using a spectrometer. To determine the absolute reflectivity of the grating, the measured grating spectrum is referenced to the spectrum of a flat gold layer, with the same thickness. The sample is positioned under an angle of

incidence with respect to the incoming light such that, according to Eq. (2.24), the plasmonic resonance is located at a wavelength of 650 nm.

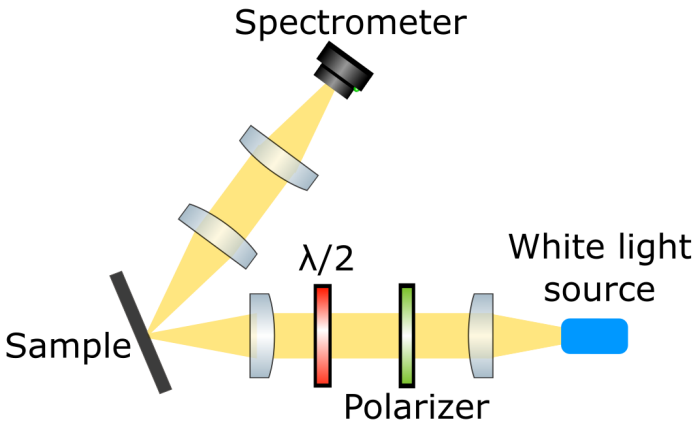

Figure 2.6: Schematic depiction of the setup used to measure the reflectance spectrum of the SPP grating.

The measured spectra can be seen in Fig. 2.7 where we plot the measured reflection spectrum of a gold grating with a periodicity of 440 nm, for different polarizations of the incident light. In this figure, 0° refers to a polarization of the electric field parallel to the grating lines, and 90° refers to a polarization of the electric field orthogonal to the grating lines. Here, we find that the excitation of an SPP is most efficient if the light is polarized perpendicularly to the grating lines.

As can be seen from Eq. (2.24), the SPP resonance frequency depends on the angle of incidence θ as well. To determine the angle of incidence required to launch an SPP efficiently, we measure the linear reflection at a specific wavelength and vary the angle of incidence by rotating the sample with respect to the incoming beam. An example of this is shown in Fig. 2.8, where we plot the normalized measured linear reflection of the laser pulses with a wavelength of 650 nm and a Full Width at Half Maximum (FWHM) bandwidth of 20 nm, as a function of θ. A clear dip is visible at an angle of incidence of $\approx 21°$, indicative of the SPP resonance.

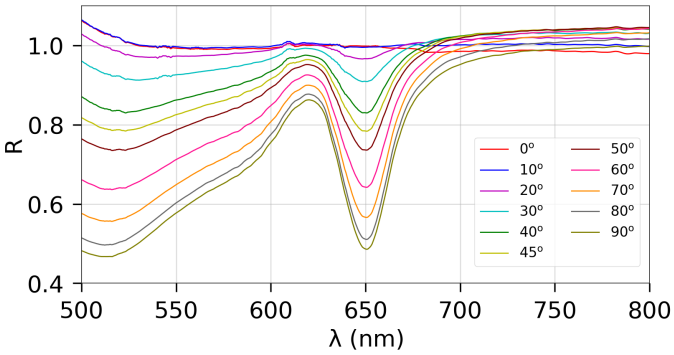

Figure 2.7: Linear reflection spectra for different laser polarizations on a gold grating with a periodicity of 440 nm, an amplitude of 47 nm, and a duty-cycle of 71 %. The grating is positioned under an angle of 21 degrees with respect to the light source such that the SPP resonance is at 650 nm. Note that the reflection increases to values bigger than 1 for some polarizations for wavelengths below 550 nm and above 675 nm, this is most likely due to low signal to noise in this wavelength regime, and potential alignment errors.

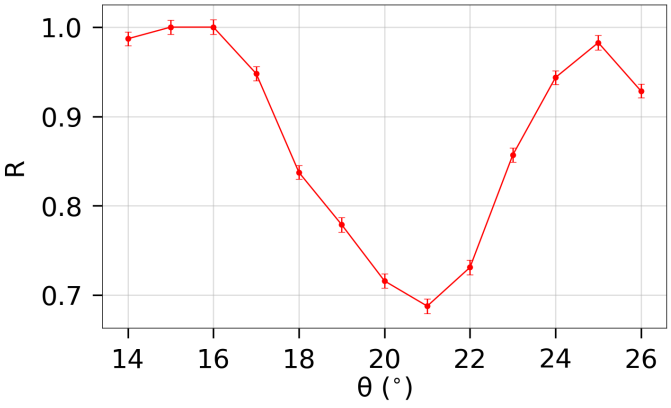

Figure 2.8: Measured normalized linear reflection of the laser reflected off the SPP grating at a wavelength of 650 nm, as a function of the angle of incidence. The SPP resonance is located at $\approx 21°$. The electric field is polarized perpendicularly to the grating lines.

3 Experimental methods

This chapter outlines the experimental methods used in the experiments described in this Thesis. First, we give a description of the laser system we used, including the OPA (HE-TOPAS). Next, we will explain how we use the laser and the HE-TOPAS to perform pump-probe experiments. After this, a description will be given on how specific samples were made using different techniques for thin layer deposition. These samples are used for time-dependent photo-acoustic measurements and high-intensity laser ablation measurements, as will be discussed later in this thesis. Furthermore, we will discuss different diagnostic techniques used on the fabricated samples. These techniques include Scanning Electron Microscopy (SEM), Atomic Force Microscopy (AFM), and Ellipsometry.

3.1 Ti:Saphhire Ultrafast laser

All of the experiments described in this thesis have been performed using a commercially available Ti:Sapphire amplified laser system (Astrella, Coherent). This laser generates a pulse train with a repetition rate of 1 kHz, a central wavelength of 800 nm, an average power of 6 W, and a pulse length of 35 fs. A functional block diagram of the laser system is shown in Fig. 3.1. A CW-pumped oscillator inside the Astrella system produces a laser pulse train with a repetition rate of 80 MHz, a central wavelength of 800 nm, a pulse length of 35 fs, and an average power of 450 mW. The pulses are stretched in time using a grating stretcher to prevent optical damage on the Ti:Sapphire crystal during the amplification stage. After the pulses are stretched, they are switched into the amplification cavity by a Pockels cell. The Pockels cell changes the polarization of the pulses by 90 degrees, such that polarizing optics keep the pulses inside the cavity. Once a pulse enters the cavity the Pockels cell turns off, preventing the pulse from leaving the cavity. The timing of the off/on switch of the Pockels cell is determined by the Synchronous Delay Generator (SDG). The SDG is the clock of the laser, which is locked to the repetition rate of the oscillator. All the timing circuits of the laser are regulated by the SDG. Furthermore, the SDG is also used for the timing circuit of the setup. The SDG, for instance, also regulates the triggering of the detectors in the pump-probe setup.

Once the pulses are trapped inside the cavity, they are amplified by passing through a Ti:Sapphire crystal. The Ti:Sapphire crystal is actively pumped by a 1 kHz repetition rate pump laser with a central wavelength of 532 nm, a pulse length of 200 ns, and an average power of 30W. The cavity is designed in such a way that 1 out of 80.000 pulses from the oscillator is amplified. The pump laser repetition rate is locked to the repetition rate of the oscillator via de SDG, ensuring that no temporal drifts occur between the oscillator and the pump laser. The laser pulses inside the cavity are trapped for 12 round trips, ensuring maximum amplification of the pulses. After 12 round trips, the second Pockels cell is turned on by the SDG. This changes the polarization of the amplified laser pulse after which the pulse is coupled out of the cavity via a mirror which reflects one polarization and transmits the other. After the laser pulse is coupled out of the cavity, it passes through a grating compressor, to reduce the pulse length as much as possible. After the grating compressor, the pulse length is 35 fs and has a central wavelength of 800 nm at a repetition rate of 1 kHz with an average power of 6 W.

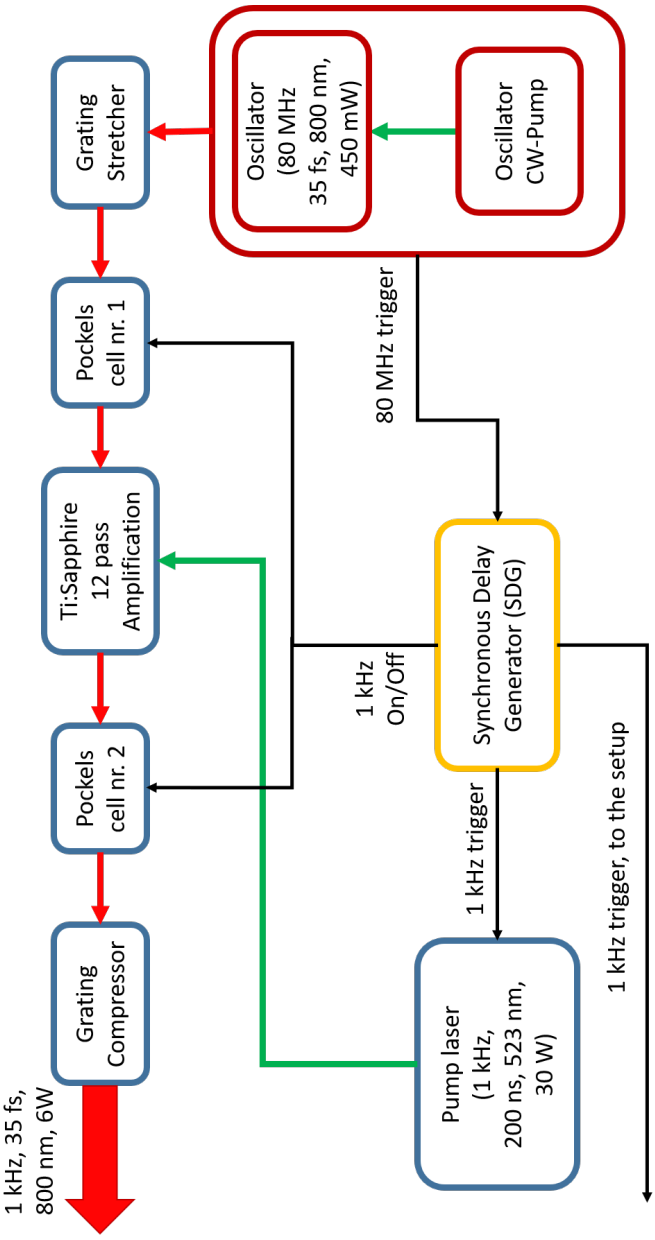

Figure 3.1: This figures depicts the functional block diagram of the laser used in our experiments.

3.2 HE-TOPAS

Approximately 80% of the power coming out of the Ti:Sapphire laser is used to power a commercially available (HE-TOPAS, LightConversion) three-stage Optical Parametric Amplifier (OPA). The OPA is a crucial part of the setup since it allows us to change the wavelength of our laser pulses. It can convert the 800 nm central wavelength laser pulses coming from the Astrella to pulses with a tunable wavelength, ranging from 1150 nm to 2400 nm. In Fig. 3.2 a schematic depiction of the beam path inside the HE-TOPAS is shown.

The beam entering the TOPAS is split by a 90/10 beamsplitter (BS-1), reflecting 90% of the incident power and transmitting 10%. The transmitted beam is split by a second 90/10 beamsplitter (BS-2), again reflecting 90% of the incident power and transmitting 10%. Finally, the transmitted beam is split one final time using an 80/20 beamsplitter (BS-3), reflecting 80% of the incident power and transmitting 20%. The transmitted beam is focused onto a sapphire crystal where a white light continuum (WLC) is generated via the process of self-phase modulation [73]. The WLC is focused on BBO-1 (β-Barium-Borate), where it overlaps in space and time with the pump beam reflected off BS-3. The delay between the WLC and the pump is regulated by an optical delay stage: delay 1. By changing the temporal overlap between the WLC and the pump pulse we can selectively enhance the desired frequency of the WLC via parametric amplification.

The process of parametric amplification splits a pump-photon with a frequency ω_p into a lower frequency signal-photon ω_s and an even lower frequency idler-photon ω_i [74]. Conservation of momentum and energy have to be full filled resulting in

$$\begin{aligned} \omega_p &= \omega_s + \omega_i, \\ \vec{k}_p &= \vec{k}_s + \vec{k}_i, \end{aligned} \tag{3.1}$$

where $\vec{k}_p$, $\vec{k}_s$ and $\vec{k}_i$ are the momentum of the pump, signal and idler photons, respectively. By introducing a "seed-frequency" when a pump photon is split, one can preselect the frequencies in which the pump photon splits. In doing so, the frequency of the signal photon will equal the frequency of the seed, thus amplifying the seed frequency [74]. Inside BBO-1 the seed frequency is supplied by the WLC. Furthermore, the configuration in BBO-1 is non-collinear. Therefore, due to the conservation of momentum, the generated idler beam and the remaining part of the pump beam are separated spatially from the generated signal beam.

After selection of the desired wavelength has taken place in BBO-1, the signal beam is incident on BBO-2. Here, it overlaps in both space and time with another

pump beam, which was split off at BS-2. This part is called the pre-amplifier stage. Again, we ensure overlap in time by adjusting the delay between the signal and the pump using delay 2. Here, the signal beam is pre-amplified to a power of approximately 50 mW. During amplification of the signal beam, an idler beam is generated which, due to the collinear arrangement in the crystal, travels in the same direction as our pre-amplified signal. Using an anisotropic crystal, the idler is separated from the pre-amplified signal beam *in time* by approximately 1 ps. After the anisotropic crystal, the remainder of the pump beam is removed using a dichroic mirror and is directed into a beam dump. The pre-amplified signal beam, and the idler beam, are finally incident onto BBO-3. Here the pre-amplified signal beam overlaps in both space and time with the final high-power pump beam, split off at BS-1. This pump beam contains approximately 90% of the total power entering the HE-TOPAS. Here the pre-amplified signal beam gets amplified to approximately 1 W. This is called the high-power amplification stage. Finally, the pump beam is split off again using a dichroic mirror, and signal and idler are separated in space using a dichroic beamsplitter.

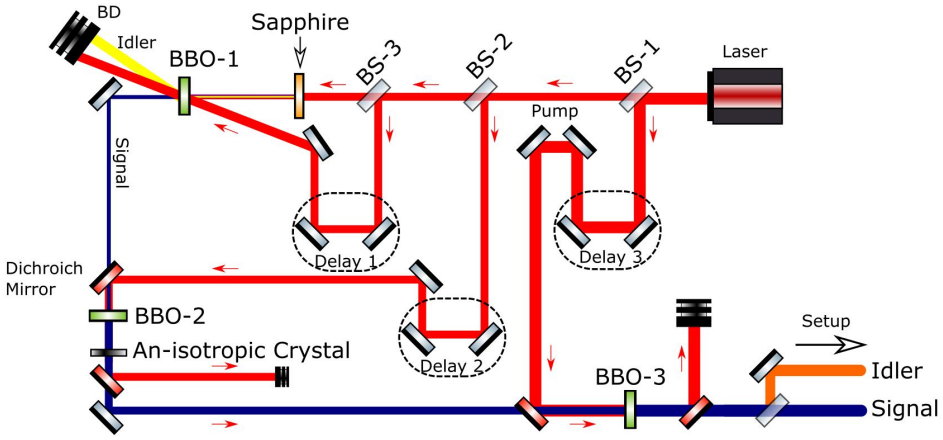

Figure 3.2: This figure shows a schematic depiction of the beam path inside the OPA. The incoming pulses have a wavelength of 800 nm. The output pulses are tunable in a wavelength range of 1150 to 2400 nm. Here, BS is a beamsplitter, BD a beamdump and BBO is a β-Barium-Borate crystal.

Using the HE-TOPAS, as described above, allows us to produce a signal beam that is tunable from 1150 nm to 1600 nm, with a pulse length of 40 fs and an average power of about 1 W. Furthermore, we also generate an idler beam which is tunable from 1600 to 2400 nm, with a pulse length of 40 fs and an average power of about 500 mW.

3.3 Pump-Probe

3.3.1 General principle

The optical experiments performed in this thesis mostly consist of pump-probe experiments. A schematic depiction of the general pump-probe scheme is shown in Fig. 3.3. A strong, high-intensity pump pulse passes through a mechanical chopper, which reduces the repetition rate of the pump by exactly a factor of two, with respect to the repetition rate of the probe, resulting in a repetition rate of 500 Hz. Afterward, the pump beam is focused onto the sample using a lens. Here, it is partially absorbed by the sample, inducing changes in the permittivity and/or topography of the sample. These pump-induced changes of the sample are subsequently measured using a weak, time-delayed, probe pulse. The probe beam can be measured either in transmission or in reflection. When the sample is excited using a transient-grating geometry, it is also possible to measure diffraction. The probe beam is time-delayed with respect to the pump beam using an optical delay line. The delay line increases/decreases the path length of the probe with respect to the pump. This allows us to measure the influence of the pump pulse on the sample at different times after excitation. In the example shown in Fig. 3.3, the probe beam is delayed with respect to the pump beam, but it is also possible to do the reverse and delay the pump with respect to the probe.

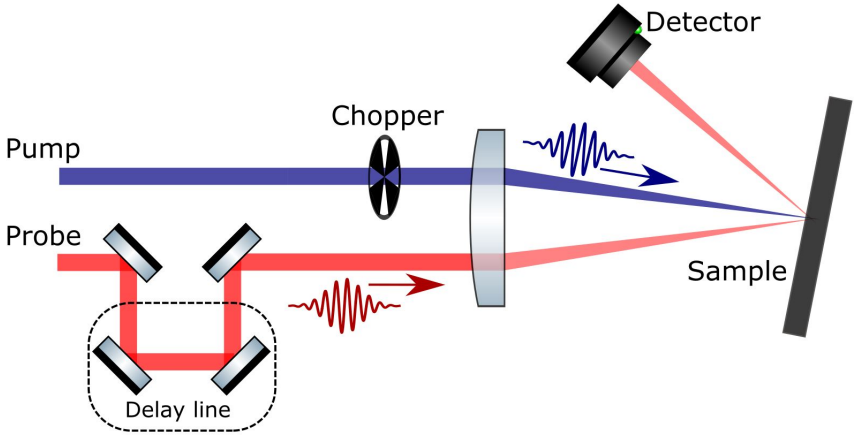

Figure 3.3: This figure shows the general principle behind the pump-probe technique. A strong pump beam, with half the repetition rate of the probe beam, excites the sample. This induces changes in the permittivity/structure of the sample. These pump-induced changes are subsequently measured using a time-delayed weak probe pulse.

As mentioned before, the repetition rate of the pump beam is half that of the probe beam, this means that for each two consecutive probe pulses incident on the sample, only one experiences pump-induced changes. The probe pulses which experience pump-induced changes are called "pumped shots" (P) and the probe pulses for which the pump beam was blocked by the chopper are called "blocked shots" (B). Using this technique we can define pump-induced changes as:

$$\frac{\Delta\xi}{\xi} = \frac{I_P - I_B}{I_B}, \tag{3.2}$$

where ξ represents either reflection, transmission, or diffraction, depending on the measurement geometry, and where I_P and I_B are the intensity of the pumped and blocked shots as measured by the detector, respectively. Details of the experimental geometry used for each experiment will be provided in the individual chapters.

3.3.2 Optical excitation of a Transient grating

Several experiments in this thesis have been performed making use of a so-called transient grating. When two laser beams are incident on a surface under an angle, they will interfere and create a spatial interference pattern. This interference pattern consists of alternating dark and bright fringes. If the light in the bright fringes changes the optical properties of the material or causes the material to expand or contract, a grating is formed from which light can diffract. Here, we will show how the periodicity of the transient grating, Λ, depends on the laser wavelength, λ, and the half-angle, θ between the two beams

In Fig. 3.4 we show a schematic view of two laser beams, with a wavelength λ crossing under an angle 2θ. In our coordinate system we can write down the equations for the electric field, assuming continuous wave beams for simplicity, polarized in the z-direction, of both beams as

$$\overrightarrow{E}_1(\vec{r},t) = E_1 e^{i\left[\vec{k}_1\cdot\vec{r}-\omega t+\phi_1\right]}\hat{\mathbf{z}} \tag{3.3}$$

$$\overrightarrow{E}_2(\vec{r},t) = E_2 e^{i\left[\vec{k}_2\cdot\vec{r}-\omega t+\phi_2\right]}\hat{\mathbf{z}} \tag{3.4}$$

where ω is the optical frequency, t is the time, E_1 and E_2 are the magnitudes of the electric fields, $\vec{k}_1$ and $\vec{k}_1$ the wave vectors, ϕ_1 and ϕ_2 the optical phase offsets $\vec{r}$ is the unit vector in Cartesian space and $\hat{\mathbf{z}}$ is the unit vector in the z-direction. We can write down the wave vectors as

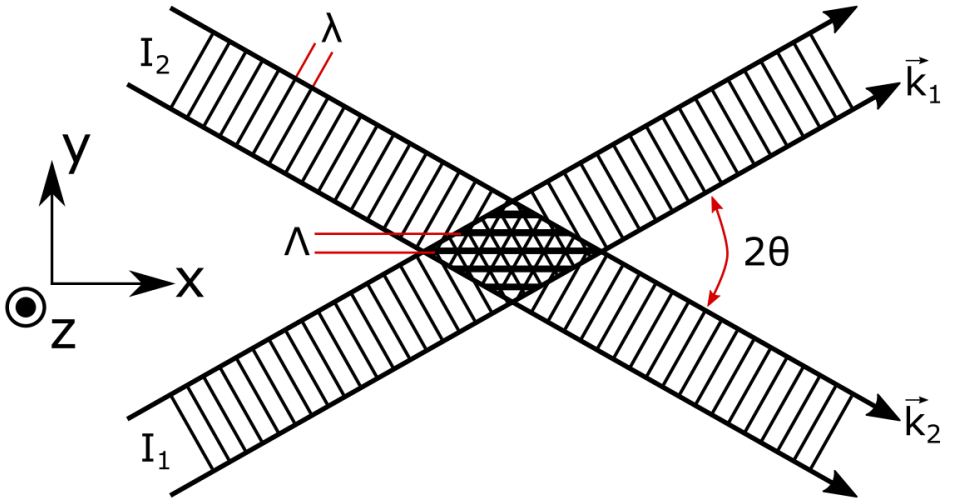

Figure 3.4: Schematic depiction of the formation of a transient grating with periodicity Λ when two laser beams with wavelength λ overlap. The half angle between the two beams is denoted by θ.

$$\vec{k}_1 = (k_{1,x},\ k_{1,y}) \tag{3.5}$$

$$\vec{k}_2 = (k_{2,x},\ k_{2,y}) = (k_{1,x},\ -k_{1,y}) \tag{3.6}$$

where we have written $\vec{k}_2$ in the components of $\vec{k}_1$ based on symmetry and the assumption that the optical wavelengths of both beams are the same. We can now write out the dot-product in the exponents of eqs. (3.3) and (3.4) to find

$$\vec{E}_1(x,y,t) = E_1 e^{i[(k_{1,x}x + k_{1,y}y) - \omega t + \phi_1]}\hat{\mathbf{z}} \tag{3.7}$$

$$\vec{E}_2(x,y,t) = E_2 e^{i[(k_{1,x}x - k_{1,y}y) - \omega t + \phi_2]}\hat{\mathbf{z}}. \tag{3.8}$$

In order to determine the electric field of the interference pattern, we need to add the electric fields of both beams. In order to simplify the arithmetic we assume that both electric field amplitudes are the same ($E_1 = E_2 = E_i$) and that the optical phases are zero ($\phi_1 = \phi_2 = 0$). Thus we find that the total electric field equals

$$\begin{aligned}\vec{E}_{tot}(x,y,t) &= \vec{E}_1(x,y,t) + \vec{E}_2(x,y,t) \\ &= E_i e^{-i\omega t} e^{ik_{1,x}x} \left[e^{ik_{1,y}y} + e^{-ik_{1,y}y}\right] \hat{\mathbf{z}} \\ &= E_i e^{-i\omega t} e^{ik_{1,x}x} \times 2\cos\left[k_{1,y}y\right] \hat{\mathbf{z}}.\end{aligned} \tag{3.9}$$

From the final part of Eq. (3.9) we see an oscillatory cosine term in the y-direction. This is the interference pattern of the two electric fields. We can split the equation for the electric field in an amplitude term and a phase term,

$$\vec{E}_{tot}(x,y,t) = E_0 e^{i(k_{1,x}x - \omega t)} \hat{\mathbf{z}} \tag{3.10}$$

where $E_0 = 2E_i \cos\left[k_{1,y}y\right]$. In order to calculate the interference pattern in the intensity we need to calculate I_{tot}. We can do so using the following identity [55],

$$I \equiv \langle S \rangle = \frac{\epsilon_0 cn}{2} \left|E_0\right|^2 \tag{3.11}$$

where ϵ_0 is the vacuum permittivity of space, c the speed of light and n the refractive index of the propagation medium. If we combine eqs. (3.9) and (3.11) we find

$$\begin{aligned}I_{tot} &= \frac{\epsilon_0 cn}{2} 2\left|E_i\right|^2 \cos^2\left[k_{1,y}y\right] \\ &= \frac{\epsilon_0 cn}{2} 2\left|E_i\right|^2 \left(\frac{1+\cos\left[2k_{1,y}y\right]}{2}\right) \\ &= \frac{\epsilon_0 cn}{2}\left|E_i\right|^2 + \frac{\epsilon_0 cn}{2}\left|E_i\right|^2 \cos\left[2k_{1,y}y\right].\end{aligned} \tag{3.12}$$

From Eq. (3.12) we see that we end up with a spatial modulation in the intensity due to the cosine term present in Eq. (3.12). Since in our discussed geometry, $k_{1,y} = \sin(\theta)\frac{2\pi}{\lambda}$ we find that the periodicity of the transient grating equals,

$$\Lambda = \frac{\lambda}{2\sin\theta}. \tag{3.13}$$

When we excite a sample with two crossed pump beams, we see from Eq. (3.13) that we can control the periodicity of the transient grating by changing the wavelength of the pump beam or the angle between the two beams.

3.3.3 Laser-induced reflection and diffraction changes

In Fig. 3.5 we show two pump-probe experiments in different measurement geometry, both performed on the same 100 nm thick gold sample. In both geometries, the pump pulse has a wavelength of 400 nm and a pulse length of about 50 fs. In Fig. 3.5(a) we show a measurement in which a single strong pump beam illuminates a flat 100 nm thick gold layer at t = 0. The pump-induced changes in reflectivity of the sample are measured using a 650 nm wavelength, weak probe beam as a function of time. On the horizontal axis, we plot the time delay between pump and probe in ps, and on the vertical axis, we plot the pump-induced change in reflection. Note that at negative time delays the change in reflection equals exactly 0 %. This is because at negative time delays, the probe pulse arrives on the sample before the pump pulse and therefore it does not measure any pump-induced changes. At t = 0 we measure a strong, quasi-instantaneous decrease in the reflection, caused by the heating of the electron gas. This so-called electron-peak is followed by a gradual decrease of the reflection change, caused by the transfer of energy from the electrons to the lattice via electron-phonon coupling. Finally, the reflection change quasi stabilizes after approximately 20 ps. This is due to the stabilization of the lattice temperature. The lattice will cool down to room temperature via heat-loss to the substrate and its surroundings on a time scale shorter than 1 ms. Both the electron- and the lattice temperature increases induce changes in the optical reflectivity of a metal layer via changes of the permittivity [75, 76].

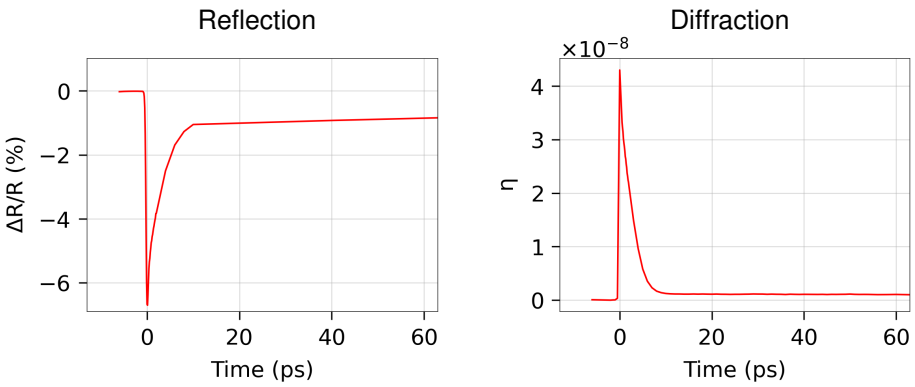

(a) (b)

Figure 3.5: Measured pump-induced reflection (a) and diffraction (b) changes after illumination with a 400 nm pump pulse on a flat 100 nm thick gold layer on a glass substrate as a function of time between the pump and the probe. The probe wavelength equals 650 nm.

In Fig. 3.5(b) we show a measurement in which the sample is excited using two crossed strong pump beams with a wavelength of 400 nm in a transient-grating geometry. The period of the grating on the surface is 6 µm. Again, on the horizontal axis, we plot the time delay between the pump and the probe in ps, but on the vertical axis we now plot the pump-induced diffraction efficiency η. We measure a strong peak in diffraction efficiency at t = 0 ps. This peak is caused by diffraction of a grating induced by the spatially periodic absorption of the laser energy by the electron gas. This creates a grating in the electron temperature, which results in a grating in the permittivity of the material off which the probe will diffract [77]. Afterward, we see a decrease in the diffraction efficiency due to energy transfer of the electron gas to the lattice via electron-phonon coupling. This results in a nearly constant non-zero diffraction efficiency, which is caused by diffraction of the probe of two types of gratings: (i) a grating in the lattice temperature which causes spatially periodic changes of the complex permittivity of the metal, and (ii) a grating formed by heat-induced expansion of the metal in the light fringes of the two-pulse interference pattern [26, 27, 78].

As can be seen in Fig. 3.5, reflection and diffraction can exhibit different behaviour in response to the same excitation. The predominant reason for this is because reflection measurements are *only* sensitive to the strain-induced changes of the permittivity, while diffraction measurements are sensitive to *both* strain-induced changes of the permittivity *and* strain-induced displacement of the surface.

3.4 Sample fabrication and diagnostics

3.4.1 Thin layer deposition

To create the thin metal layer samples used in this thesis, we employed two different techniques: thermal evaporation and plasma-assisted sputtering. Whether evaporative deposition or sputter deposition is used depends mostly on the type of material used and in particular on their physical properties such as their melting and boiling temperatures. Generally speaking, sputter coating is used for metals with a high boiling temperature.

The substrates used in most of the samples were chemically cleaned pieces of glass. The glass substrates are first cleaned in an ultra-sonic bath of water. After this, they were treated with a base-piranha solution. This is a strongly alkaline solution that will remove most organic matter from a surface. It is created by mixing water with NH_4OH and H_2O_2 in a 5:1:1 ratio at 75 C°.

In Fig. 3.6(a) we show a schematic depiction of the thermal evaporation process. The entire process takes place in a vacuum chamber with a pressure of approxi-

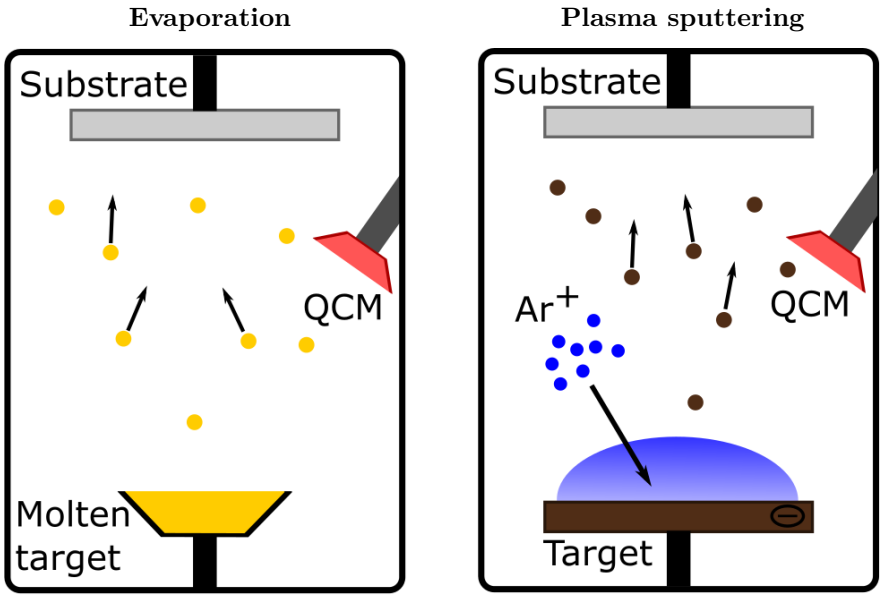

(a) (b)

Figure 3.6: (a) Schematic depiction of the thermal evaporation process. The target material is melted by running a strong current through the crucible. After reaching the boiling temperature, the target begins to evaporate and material lands on the substrate. The deposition rate is monitored using a quartz crystal monitor (QCM). (b) Schematic depiction of the plasma-assisted sputter-coating process. The target material is bombarded by charged argon ions which eject material from the target towards the substrate.

mately 10^{-7} mbar. The target material is melted in a crucible by applying a high current through the crucible. When the target material reaches a high enough temperature, atoms on the surface of the molten target will start to evaporate after which they will deposit onto the substrate positioned above the target material. The deposition rate is monitored using a quartz crystal monitor (QCM). Under normal conditions, the quartz crystal vibrates with its mechanical eigenfrequency. When evaporated atoms of the molten target strike the QCM, its eigenfrequency changes depending on how much material is deposited onto the QCM. By measuring the change of eigenfrequency as a function of time, the deposition rate can be determined via differentiation. After calibration of the crystal, the change in eigenfrequency can be related to the deposition rate. The thermal evaporation technique was used in this thesis to evaporate thin Au layers. Typical deposition

rates were around 1 Å/s

In Fig. 3.6(b) we show a schematic depiction of the plasma-assisted sputter-coater. When the substrate is loaded into the sputter chamber, a vacuum is created reaching pressures of approximately 10^{-7} mbar. After the required pressure is reached highly energetic Ar^+-ions enter the chamber, forming a plasma at a pressure of approximately 10^{-2} mbar. The target material, which is under a negative bias voltage with respect to the substrate, is bombarded by the Ar^+-ions. The Ar^+-ions impacting the target material eject particles from the target. These target material atoms will land on the substrate. The deposition rate is again measured using a QCM. Plasma-assisted sputter-coating was used in this thesis to create thin layers of Ru, with typical deposition rates of around 3-6 Å/s.

3.4.2 Scanning Electron Microscopy

After fabrication of a sample, it is important to image the surface to check for defects. One of the techniques we used to image the surface is called Scanning Electron Microscopy (SEM). An SEM uses electrons, rather than light, to image a surface. Electrons are used since this allows us to measure structures smaller than the wavelength of visible light. A strong, highly energetic beam of electrons is emitted downward from a Schottky Field Emission Gun. Afterward, the beam of electrons is focused onto the sample using electromagnetic lenses.

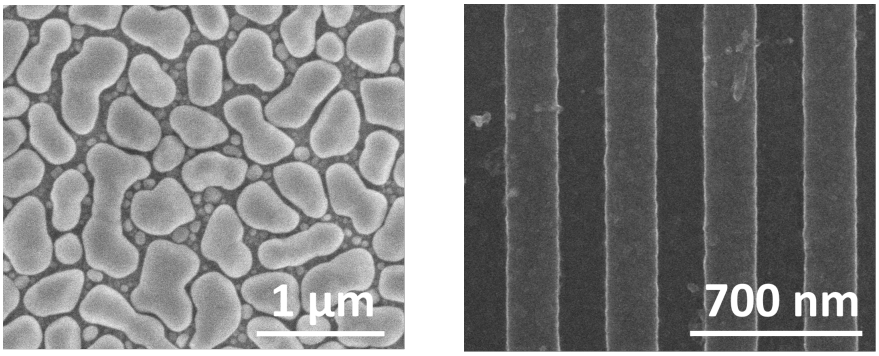

(a) (b)

Figure 3.7: SEM example images. (a) nano-structured Sn-islands on glass substrate and (b) a SiO_x grating fabricated on top of a Si substrate.

When the electrons interact with the material several types of signals are created. The material will emit secondary-, Auger- and back-scattered-electrons which are captured by either a Through-the-lens-detector [79] or an Everhart-Thornley-detector [80]. The magnitude and scatter patterns of these signals con-

tain information on the topography of the material and allow for reconstruction of the surface with a spatial resolution of 0.9 nm. Furthermore, the sample might also emit X-rays which could give chemical information about the surface [79]. Since the SEM works based on electron absorption, emission and scattering, the best images are obtained for conducting materials. If a non-conducting material is used in the SEM, the material will accumulate charge and deflect/disturb the electron beam. In this work, SEM images were obtained using the FEI-Helios 600, located in the Amsterdam Nanolab at AMOLF.

In Fig. 3.7 we show two example SEM images. In Fig. 3.7(a) we show an SEM image of a nanostructured Sn layer with an average layer thickness of 60 nm deposited on a glass substrate. In Fig. 3.7(b) we show an SEM image of a SiO_x grating with a periodicity of 440 nm and an amplitude of 50 nm fabricated on top of a Si substrate. To negate charging effects on the SiO_x, a low electron beam voltage was applied, and the sample was clamped between two conducting materials.

3.4.3 Atomic Force Microscopy

Whereas an SEM image provides quick access to surface topography, no information is provided about the height distribution of the topography. When we want to create a 3-dimensional image of the surface we use atomic force microscopy (AFM) to do just that.

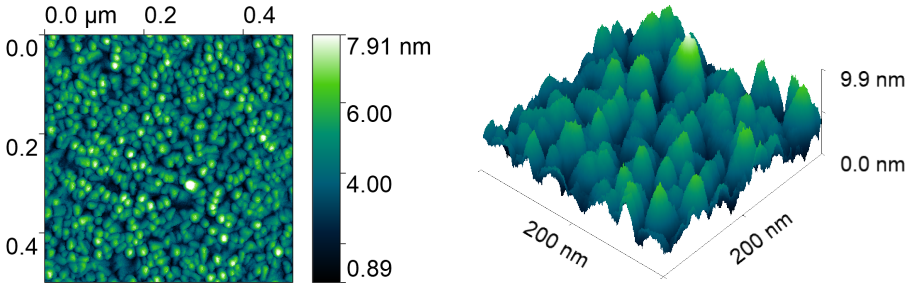

(a) (b)

Figure 3.8: AFM image of a 107 nm Ru layer deposited on glass, shown in (a) 2D and (b) in a pseudo 3D form.

An AFM makes use of a horizontal cantilever with a very sharp tip at the end. The tip diameter is usually on the order of several nanometers. When the tip is brought in close contact with the surface the cantilever will start to bend due to atomic forces, such as Van der Waals forces, between the sample and the tip [81]. The deflection of the cantilever is determined by Hook's law and generally speaking

it is measured using a laser. By scanning the surface of a sample with the AFM while continuously measuring the displacement of the tip, we can generate 3D surface topography maps. In Fig. 3.8(a) we show a 2D AFM image of a 500 x 500 nm area of a 107 nm thick Ru layer deposited on glass. In Fig. 3.8(b) we show a pseudo-3D view of a 200 x 200 nm part of the surface.

3.4.4 Ellipsometry

To accurately model the absorption of a laser pulse onto our samples, it is crucial to have access to the wavelength-dependent dielectric function of the sample. Often, the dielectric function can be extracted from literature. However, for thin layers or composite layers, the wavelength-dependent dielectric function can differ from the known bulk dielectric function. In order to overcome this problem, we use ellipsometry to measure it. In Fig. 3.9 a schematic drawing of an ellipsometer is shown.

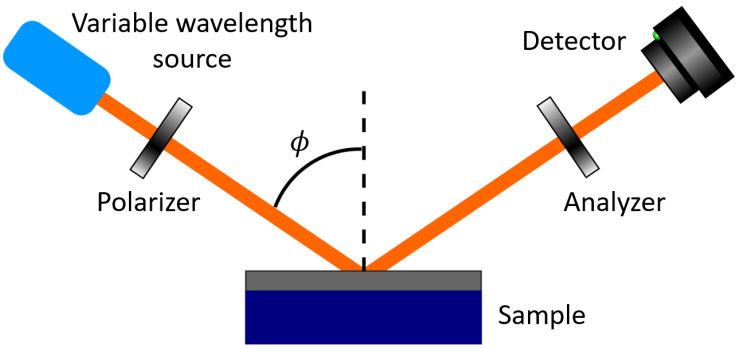

Figure 3.9: Schematic depiction of an ellipsometer. A specific wavelength is selected from a variable wavelength source. This wavelength then passes through a polarizer and reflects off the sample under an angle ϕ. Afterward, it passes through an analyzer and the light is measured using a detector.

The sample is illuminated with a light source of which the wavelength can be selected by spatial filtering of a white light continuum. The ellipsometer then measures the ratio of the normalized reflection coefficients for the s- and p-polarized components, otherwise known as the complex reflection ratio ρ,

$$\rho = \frac{r_p}{r_s} = \tan\Psi \cdot e^{i\Delta}, \tag{3.14}$$

where Ψ is the amplitude ratio of the reflected light and Δ is the phase difference

induced by the reflection. The ellipsometer measures Ψ and Δ for all wavelengths and at a few angles of incidence, ϕ, preferably around the Brewster angle. For a bulk-like sample, with only one single reflection, the dielectric function can be determined using a so-called "pseudo-transform function". Under the assumption that there are no oxide layers and that there is no surface roughness we have,

$$\epsilon_1 + i\epsilon_2 = \sin^2\phi \left[1 + \tan^2\phi \left(\frac{1-\rho}{1+\rho}\right)^2\right]. \tag{3.15}$$

However, when the sample is not bulk-like, but a thin layer, or multiple thin layers instead, and the assumption stated for the pseudo-transform function that only one reflection is present is not met, this method will not work. When this is the case a model needs to be constructed using specialized ellipsometry software which will fit the acquired data using different methods such as the harmonic-oscillator approximation [82] or the Tauc-Lorentz dispersion functions [83].

4 Plasmonic enhancement of photo-acoustic induced reflection changes*

In this chapter, we report on surface-plasmon-resonance enhancement of the time-dependent reflection changes caused by laser-induced acoustic waves. We measure an enhancement of the reflection changes induced by several types of acoustical waves such as longitudinal, quasi-normal, and surface acoustic waves, by a factor of 10 to 20. We show that the reflection changes induced by the longitudinal and quasi-normal modes are enhanced on the slopes of the surface plasmon polariton resonance. The surface acoustic wave-induced reflection changes are enhanced on the peak of this resonance. We attribute the enhanced reflection changes for the longitudinal wave and the quasi-normal mode to a shift in the surface plasmon polariton resonance by acoustically induced electron density changes and changes in the grating geometry.

*This chapter has been published in a slightly modified form as Appl. Opt. **60**(24), 7304-7313 (2021)

4.1 Introduction

Ultrafast optical pulses are capable of launching strain waves inside materials [60]. The fundamental understanding of the generation and propagation of these photo-induced acoustic echoes has grown dramatically in the past decades [59, 84–87]. Furthermore, these photo-acoustic waves have been used to study a variety of material properties and physical phenomena, such as thermal- and electron-diffusion [31–34], electron-hole plasmas in semiconductors [88], hot-electron-induced pressure [35, 36], elastic constants of single layer [37–40] and multi-layer structures [41, 42], the electronic structure of materials [43, 44], surface deformation dynamics [45–48], and the generation of terahertz radiation [89]. Furthermore, laser-induced acoustic echoes have been used for the detection of buried gratings [30,90], showing promise for applications in the semiconductor device manufacturing industry.

Generally speaking, laser-induced acoustic echoes can be detected by measuring changes in optical properties such as reflection from and transmission through a material [85] or by diffracting light from an acoustic-wave-induced grating [46, 90, 91]. Changes in optical reflection caused by acoustic waves are usually small and thus require fairly complicated setups involving high-repetition-rate laser oscillators and signal modulation/demodulation techniques. Therefore, there is a clear need for a method to enhance the signal from acoustic waves and one possible method to achieve this is to employ a plasmonic resonance.

Surface plasmon polaritons (SPPs) were first observed by Wood [92] in 1902 and have since been identified as collective electron oscillations coupled to an electromagnetic wave propagating along a metal-dielectric interface [93–95]. Surface plasmons can be generated in several different ways. The most common methods use the so-called "Kretschmann geometry" [70, 96], and plasmonic gratings [71, 97, 98]. Plasmonic gratings have been used to create terahertz frequency acoustic waves originating from a thin tellurium layer, formed by light-induced segregation in a (Cd,Mg)Te layer [99], and to study acoustic waves inside an acoustic cavity [100]. Surface plasmon polaritons have also been used to detect and quantify strain waves in Au layers [101, 102]. Furthermore, it has been shown that acoustic breathing modes in spherical nanoparticles, with diameters ranging from 15 to 120 nm, can change the localized plasmonic resonance of the particles [103–106]. Also, by using excitation and detection at a fixed wavelength, the angle-dependent plasmonic response to a longitudinal acoustic wave in a flat metallic layer in the Kretschmann geometry has been studied [36, 96, 107]. In general, however, surfaces are not flat. As a result, illumination of such a surface with a short laser pulse may give rise to the generation of additional kinds of acoustic waves, such as surface acoustic

waves (SAW's) and even particle-like normal modes. The effect of these acoustic waves on the grating surface plasmon resonance is currently not well understood.

Here, we show an in-depth study of the effect of multiple types of acoustic waves on a plasmonic grating by measuring the wavelength-dependent reflection changes in the vicinity of the SPP resonance. In our experiments, a 400 nm wavelength pump pulse illuminates the grating and a time-delayed probe-pulse tunable between 600 nm and 700 nm measures the changes in the reflection of the grating at wavelengths around the SPP resonance, located at 650 nm. Heating of the gold layer, including the grating, by the 400 nm pump leads to the generation of high-frequency acoustic waves in the material. Due to these high-frequency acoustic waves, we measure oscillatory changes of the reflection on the order of 1 %. Analysis of these oscillations and their respective frequencies suggest that we observe multiple types of acoustic waves, three of which we identify as longitudinal waves [30, 59, 90], surface waves [59, 61, 66, 108, 109] and grating line quasi-normal mode oscillations [61, 110, 111]. We find that the phase of the longitudinal waves and the grating line normal modes experiences a π phase shift when the wavelength is tuned around the SPP resonance wavelength. Remarkably, we find that the optical response to the SAW is enhanced at the SPP resonance whereas the longitudinal and grating line normal modes are enhanced on the *slopes* of the resonance. The optical response of the gold may be attributed to two main effects: the acoustic-wave-induced material density changes, which in turn change the free-electron density, and the acoustic-wave-induced changes in the amplitude and duty cycle of the grating. Both of these effects give rise to a shift of the SPP resonance wavelength via a change in the plasma frequency and a change in the grating geometry, respectively. Both can explain the results for the longitudinal mode and the quasi-normal mode. The enhancement of the SAW on the peak of the SPP resonance is currently not understood. From the experiment, we estimate that the photo-acoustic detection signals are enhanced 10 to 20 fold by measuring reflection changes on and around the SPP resonance.

4.2 Experimental setup

A schematic drawing of the experimental setup is shown in Fig. 4.1. An amplified Ti:Sapphire laser (Coherent Astrella) with a repetition rate of 1 kHz, a central wavelength of 800 nm, a pulse length of 35 fs, and a maximum pulse energy of 6 mJ is used for the experiments. The output of the laser is split into two beams using an 85/15 beam splitter.

The weaker beam passes through a variable optical delay line after which the beam is frequency-doubled using a β-Barium borate (BBO) crystal to generate 400 nm

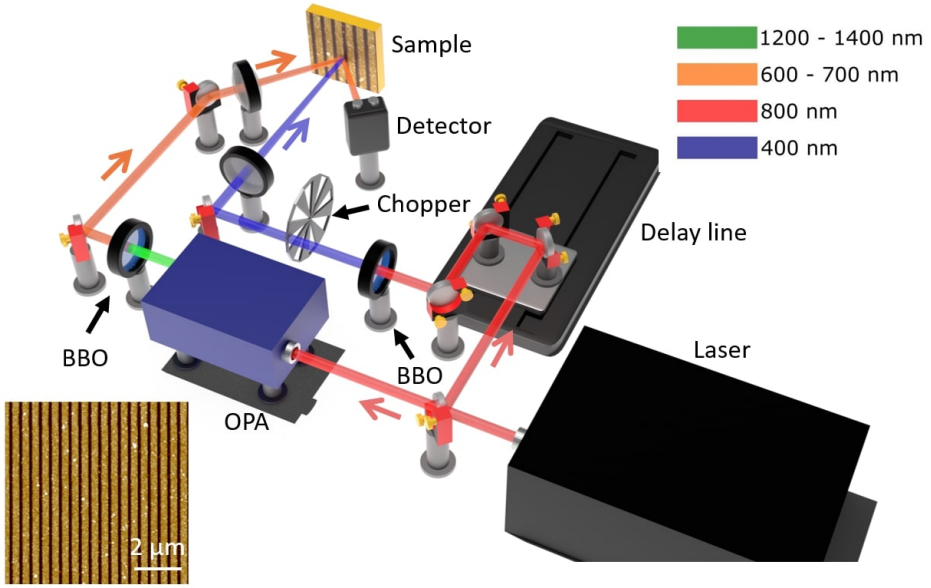

Figure 4.1: Schematic drawing of the setup. The output from a 1 kHz repetition rate Ti:sapphire amplified laser with a central wavelength of 800 nm is split into two parts. One beam (pump) is frequency-doubled to a wavelength of 400 nm by a BBO crystal and modulated by a mechanical chopper at 500 Hz. The other beam (probe) passes through a three-stage OPA changing the wavelength to a tunable range from 1200-1400 nm. This beam is frequency-doubled by a BBO to a tunable wavelength range of 600-700 nm. Both the pump and the probe beam are focused onto the sample at angles of about 5° and 21°, respectively. The probe beam angle is chosen such that the SPP resonance is located at 650 nm. Projected on the sample, we show an AFM image of the gold grating, with a layer thickness of 177 nm, a pitch of 440 nm, and a duty cycle of 71 %.

pulses. The beam passes through a mechanical chopper which is synchronized with the 1 kHz pulse train from the laser. With a 50 % duty cycle, the chopper reduces the repetition rate of the pump to 500 Hz, so that every other pump pulse is blocked. After passing through dichroic mirrors which filter out residual 800 nm light, the beam is focused onto the sample under an angle of incidence of approximately 5 degrees to a spot size of approximately 400 µm. In this geometry, the pump pulses do *not* excite SPPs. In our experiments, these pump pulses have a pulse energy of about 12 µJ.

The stronger 800 nm beam is sent to an optical parametric amplifier (OPA, HE-TOPAS, from Light Conversion). The OPA generates tunable infrared laser pulses

with wavelengths ranging from 1200 to 1400 nm with a maximum pulse energy of about 1 mJ. After the OPA, the probe pulses are frequency-doubled using a BBO crystal, such that the tunable probe wavelength ranges from 600 to 700 nm. The pulse energy of the probe pulses has been kept constant at 270 nJ. Normalized spectra of typical pulses used in the experiments can be seen in Fig. 4.2. Finally, the probe beam is focused onto the sample under an angle of approximately 21 degrees, which is the grating SPP resonance angle at a wavelength of 650 nm. The reflection of the probe pulse is measured using a Si photodiode.

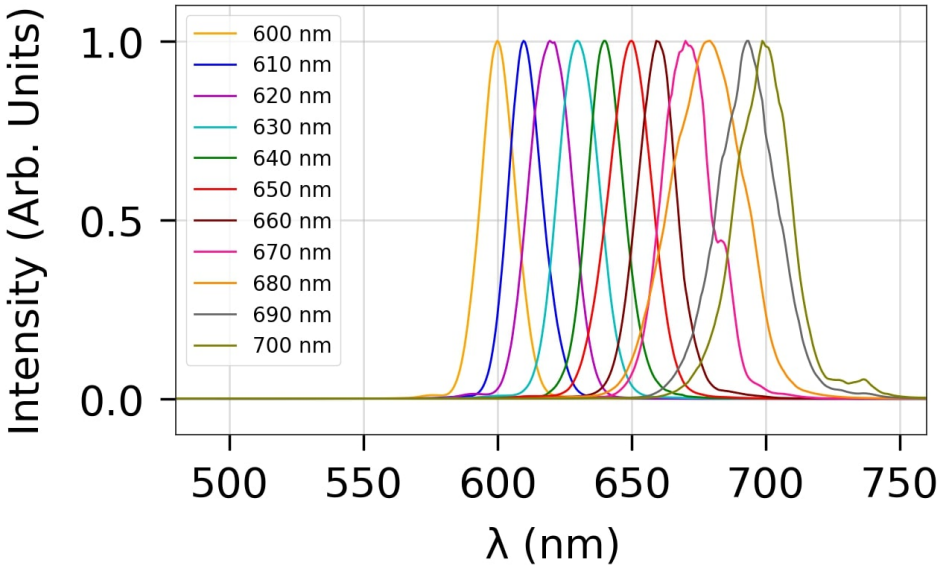

Figure 4.2: Measured laser spectra used in the experiments for different central wavelengths ranging from 600 to 700 nm. All curves have been normalized to their maximum.

Both pump and probe pulses have a duration of about 50 fs. When the pump pulse excites the sample, several types of acoustic waves are launched. These acoustic waves and their reflections change the material properties, giving rise to optical reflection changes that can be measured by the tunable, time-delayed probe pulse.

The samples are made by thermally evaporating gold layers on top of a commercially available SiO_x grating on Si (NanoPHAB B.V.). To create the grating, 200 nm SiO_x is first fabricated on top of a Si substrate. Using electron-beam lithography a grating is defined in a photoresist on the surface of the material. After developing the resist, the grating is etched in the SiO_x using reactive-ion etching. An AFM image of the grating structure after gold deposition is shown in

the bottom left in Fig. 4.1. After the deposition, the duty cycle of the grating is approximately 71 %, the pitch is 440 nm and the grating amplitude is 47 nm. The Au layer thicknesses used in our experiments are 177 nm, 136 nm, and 100 nm thick. In Fig. 4.3 we show the height profiles of the grating lines for all Au thicknesses, measured with an AFM. From this, we conclude that the grating line periodicity, amplitude, and duty cycle are comparable for all samples. We note that small differences in the shape of the grating only lead to small, static changes in the position/amplitude of the plasmonic resonance. In fact, we optimized the angle of incidence slightly for each sample to have the maximum SPP resonance at a wavelength of 650 nm. We found that changes in the angle of incidence were within our measurement accuracy of roughly half a degree.

Approximately 71% of the 400 nm pump light is absorbed by the grating structure and, for wavelengths at the SPP resonance, approximately 50% of the probe light is absorbed. In contrast, for wavelengths off-resonance, approximately 5% of the probe light is absorbed. Since the sample is optically thick, no light is transmitted.

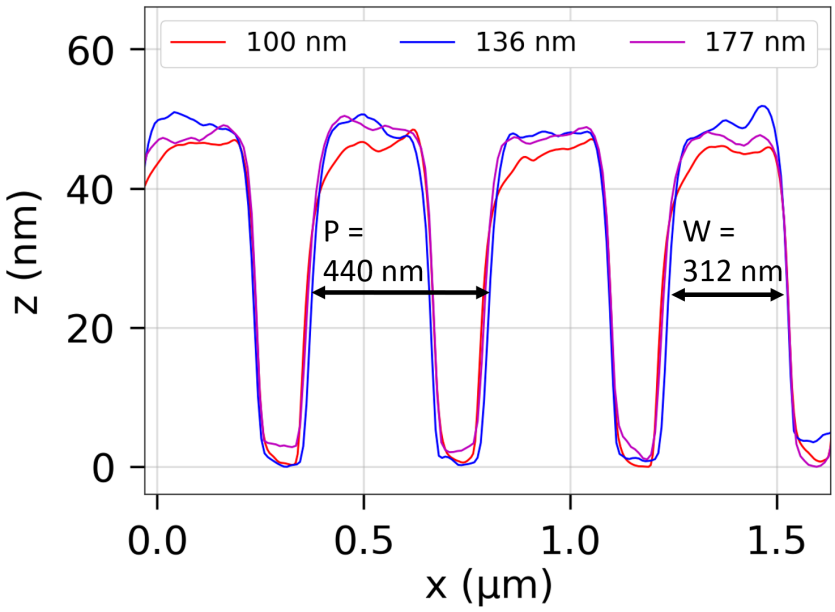

Figure 4.3: AFM Measurements of the grating line height profiles for gold thicknesses of 100 nm, 136 nm and 177 nm. In this figure, P denotes the period of the grating and W denotes the width of the lines. The duty cycle is defined as DC = W/P.

4.3 Results

For all measurements, both pump and probe pulse energies were kept constant at 12 µJ and 270 nJ, respectively. To ensure that the probe beam experiences a homogeneous excitation profile, the focal spot diameter of the probe on the sample is five times smaller than that of the pump.

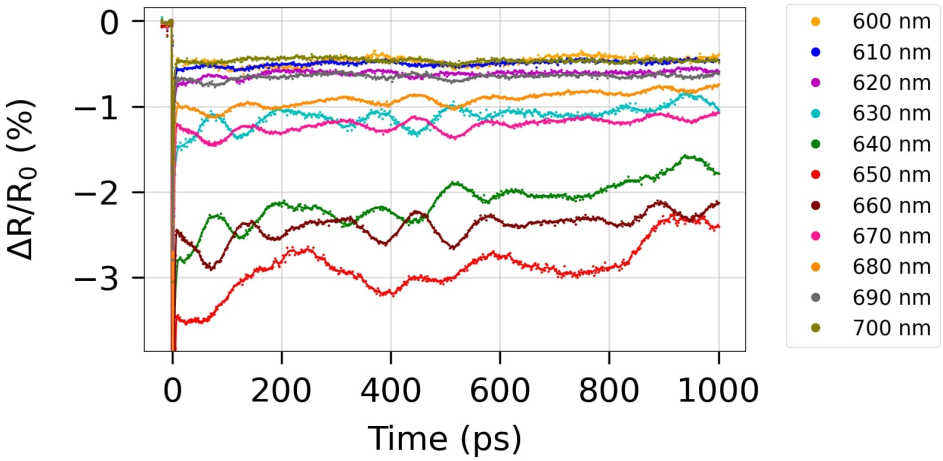

Figure 4.4: Probe pulse reflection changes measured at different wavelengths as a function of time delay between the pump and probe after excitation by a 400 nm pump beam on the 177 nm thick Au layer with a 47 nm amplitude grating on top.

In Fig. 4.4 we plot the time-dependent pump-induced change in reflection $\Delta R/R_0$, where R_0 is the unperturbed reflection, for 11 different probe wavelengths from 600 nm to 700 nm on the 177 nm thick gold sample. For all probe wavelengths, we measure an instantaneous pulse-length-limited reflection decrease, governed by electron dynamics [77]. Afterward, the reflection changes show a more complex oscillatory behavior. We measure relatively low-frequency oscillations with a frequency of 2.8 GHz, most notably at a probe wavelength of 650 nm, with an amplitude of $\Delta R/R_0 \approx 1$ %. However, slightly away from the SPP resonance, in addition to a low-frequency oscillation, we also measure higher frequency oscillations. These high-frequency oscillations are most clearly seen in the first 200 ps and are composed of at least two frequencies, namely 6.9 and 9.1 GHz. As we will discuss later, we attribute the frequencies of 2.8, 6.9, and 9.1 GHz to a surface acoustic wave (SAW), a grating line quasi-normal mode (NM), and a longitudinal wave (LW), respectively. Schematic depictions of these waves are shown in Fig. 4.5. More frequencies appear to be present in the spectrum, which we are not able to identify as of yet.

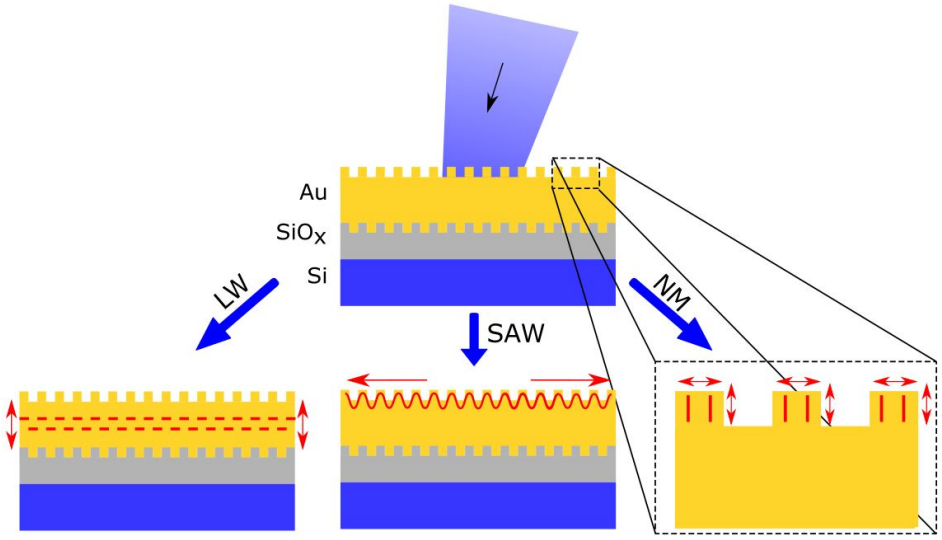

Figure 4.5: Schematic depiction of the different types of acoustic excitations presumably observed in our measurements. An ultrafast laser pulse excites the plasmonic grating. The electrons absorb the light and heat up, after which they transfer their energy to the lattice resulting in high-frequency acoustic waves. From the left to right on the bottom panel we show a schematic depiction of a longitudinal wave (LW), a surface acoustic wave (SAW), and the grating line quasi-normal modes (NM). For the LW and the SAW, the red arrows indicate the direction of propagation of the acoustic waves. For the NM the red arrows represent the direction of expansion and contraction of the grating lines. Note that the LW will partially reflect to the surface once it reaches the Au/SiO_x interface.

A numerical fast Fourier transform (FFT) of the time-dependent measurements, after the removal of the thermal background, is shown in Fig. 4.6(b). The three dashed lines represent the three most prominent frequencies located at 2.8 (SAW), 6.9 (NM), and 9.1 GHz (LW). Below 2.8 GHz we can see the appearance of an even lower frequency. Considering that this frequency corresponds to a period approximately equal to the entire time window of our measurement, we are reluctant to assign a real acoustic mode to it.

The amplitude and phase of the acoustic induced reflection changes, which are extracted from the FFT, are shown versus the optical wavelength in Figs. 4.7(a) and (b), respectively. The colors of the curves correspond to the colors of the dashed lines indicated in Fig. 4.6(b). Fig. 4.7(a) confirms that the optical response to the SAW is strongest when we probe the grating at the SPP resonance. With

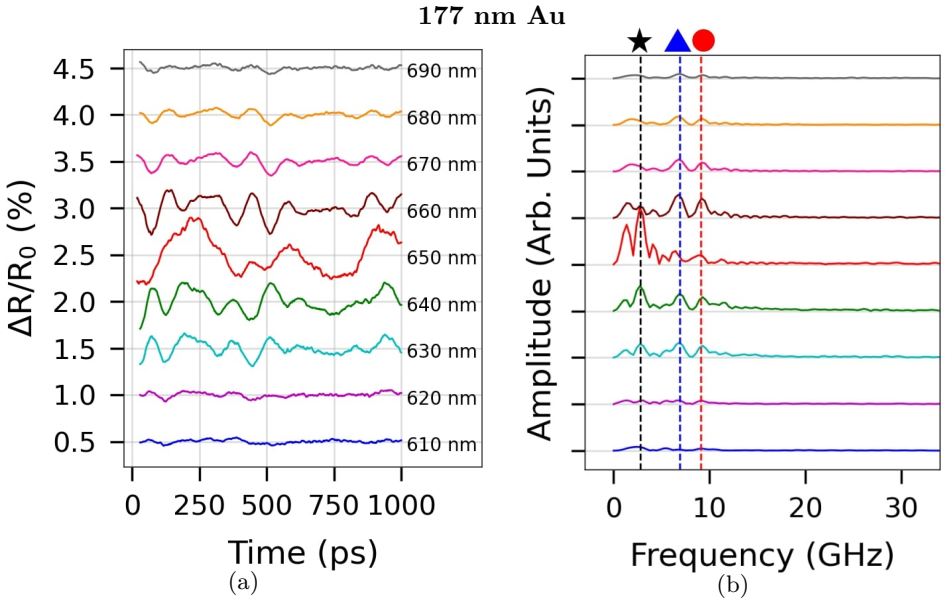

Figure 4.6: (a) Probe pulse reflection changes measured at different wavelengths as a function of time delay between the pump and probe on the 177 nm thick sample, with the thermal background removed. Each curve has been given an offset for clarity. (b) FFT of the time-dependent signals. The three dashed lines, from left to right, correspond to the expected SAW, NM, and LW frequencies.

the probe wavelength on the SPP resonance, we measure an enhancement of the 2.8 GHz signal by a factor of 20 compared to measurements with the probe wavelength on the wings of the resonance. In contrast, the two higher frequencies experience a maximum on the *slope* of the SPP resonance at 640 and 660 nm probe wavelengths. These frequencies are enhanced with a factor of approximately 10 when compared to the measurements using a probe wavelength of 600 nm, but they decrease in magnitude at the SPP resonance.

In Fig. 4.7 (b), we see that both the 6.9 GHz and the 9.1 GHz frequency components experience a phase shift of approximately π when the probe wavelength is tuned from below to above the plasmon resonance, reflecting the sign-flip seen in the time domain data. The signal measured at 2.8 GHz shows a smaller but significant variation of the phase over the entire probe wavelength range from 610-700 nm.

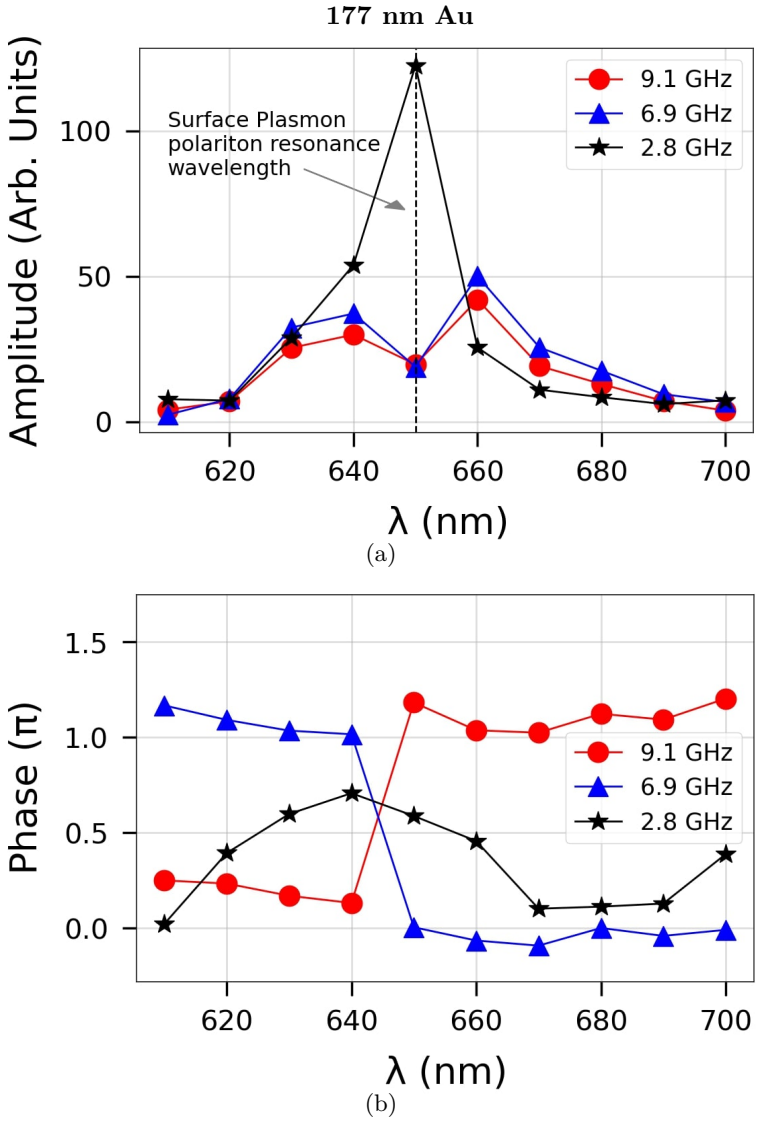

Figure 4.7: (a) The amplitude of the measured reflection changes induced by the acoustic echoes extracted from the FFT of the time-domain data. (b) The phase of the acoustic echoes. The gold layer has a thickness of 177 nm. The color and the symbols of the curves correspond to the frequency indicated by the vertically dashed lines with the same color and symbol as shown in Fig. 4.8. 4.6(b).

In Figs. 4.8(a) and (c) we show the time-dependent reflection changes measured on the same sample, now with a 136 nm and 100 nm gold layer deposited on

the grating, respectively, with the thermal background removed. Again, all wavelengths have been given a vertical offset for clarity. The fast Fourier transforms of the measured signal on the 136 nm and 100 nm samples are shown in Figs. 4.8(b) and (d), respectively.

For the 136 nm thick Au layer we measure transient reflection changes comparable to our 177 nm thick sample, both in shape and in size. The longitudinal wave frequency, which for the sample thickness of 136 nm equals 12.0 GHz, as indicated by the rightmost dashed line in Fig. 4.8(b), has shifted to a higher frequency due to the decreasing thickness. The presence of another frequency around 10 GHz is also observed, but it has not been identified yet.

In contrast to the results for the 177 nm and 136 nm thick Au layer, for the 100 nm thick sample we measure predominantly a slowly oscillating reflection change attributed to a SAW. However, in the first 100 ps, weak higher frequency oscillations are also observed, most clearly visible in the measurement with a probe wavelength of 630, 640, and 660 nm. These fast oscillations are attributed to the high-frequency longitudinal wave. They are difficult to identify in the FFT due to their relatively low signal strength and fast decay.

In Fig. 4.9, we show the amplitudes and phases of the frequencies shown by the dashed lines from Figs. 4.8(b) and (c) versus the probe wavelength. The color of the curves corresponds to the color of the dashed lines. The upper two panels and the bottom two panels represent the 136 nm and 100 nm thick sample, respectively. For both thicknesses, we measure an enhancement of the amplitude by a factor of approximately 10 for the 2.8 GHz component when approaching the SPP from the lowest wavelength of 600 nm, and from the highest wavelength of 700 nm. For the 136 nm thick gold layer we see that the 6.9 GHz and the 12.0 GHz components have a weak local minimum when resonant with the SPP and similarly, a weak maximum in the amplitude of these frequencies on the *slopes* of the resonance.

Again, for both the 136 nm and 100 nm thick samples, we measure a variation in the phase for the 2.8 GHz component, around the SPP resonance. For the 6.9 (NM) and 12.0 (LW) GHz frequency components, as observed for the 136 nm sample, we measure an approximately π phase shift around the plasmon resonance, which is similar to what we see for the 177 nm thick sample. Due to the low signal strength of the LW and the NM for the 100 nm thick layer, the amplitude and phase could not be determined for these modes.

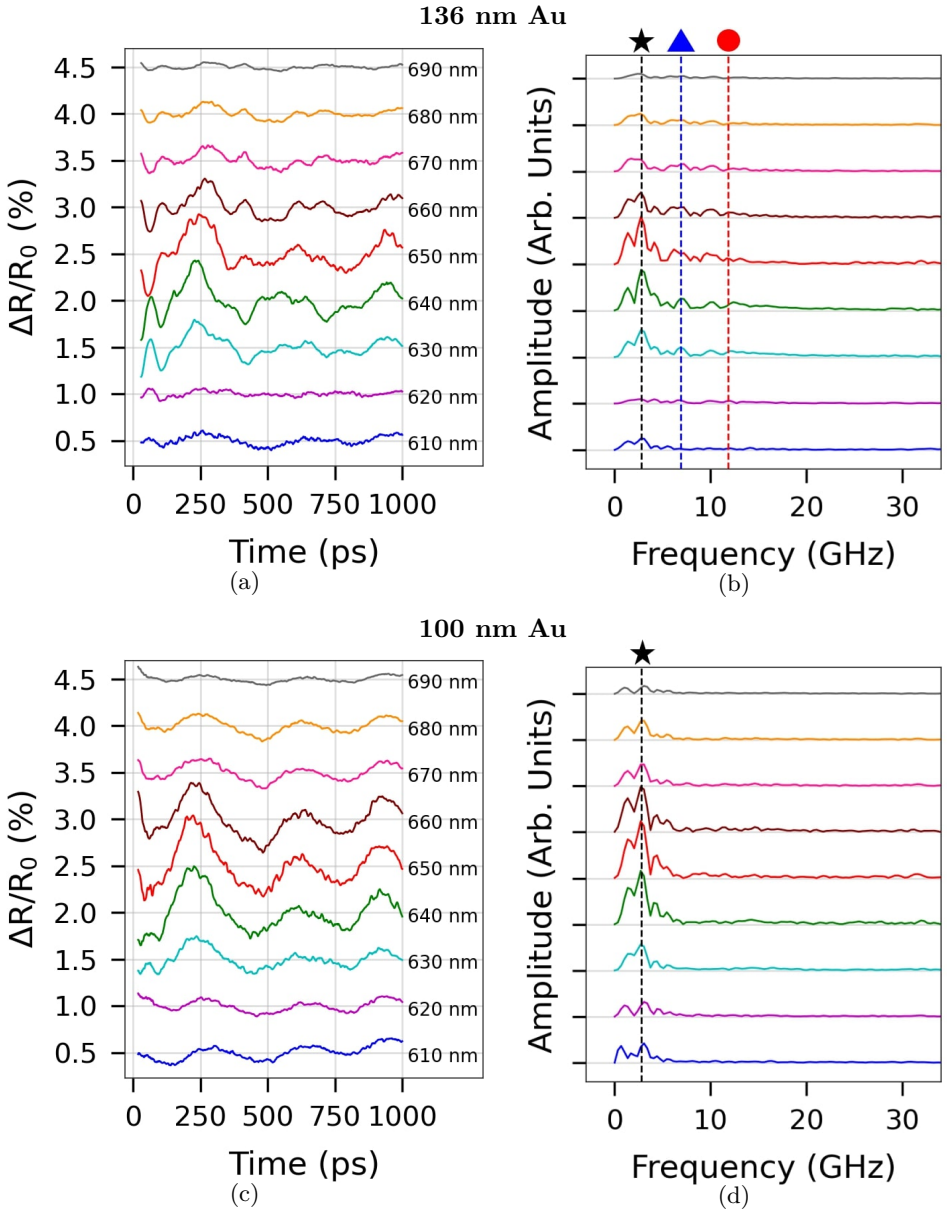

Figure 4.8: (a) Reflected probe signal with the thermal background removed for the 136 nm thick gold layer and (c) for the 100 nm thick gold layer. (b) Fourier transform of the time dependent signal for the 136 nm thick sample and (d) for the 100 nm thick sample.

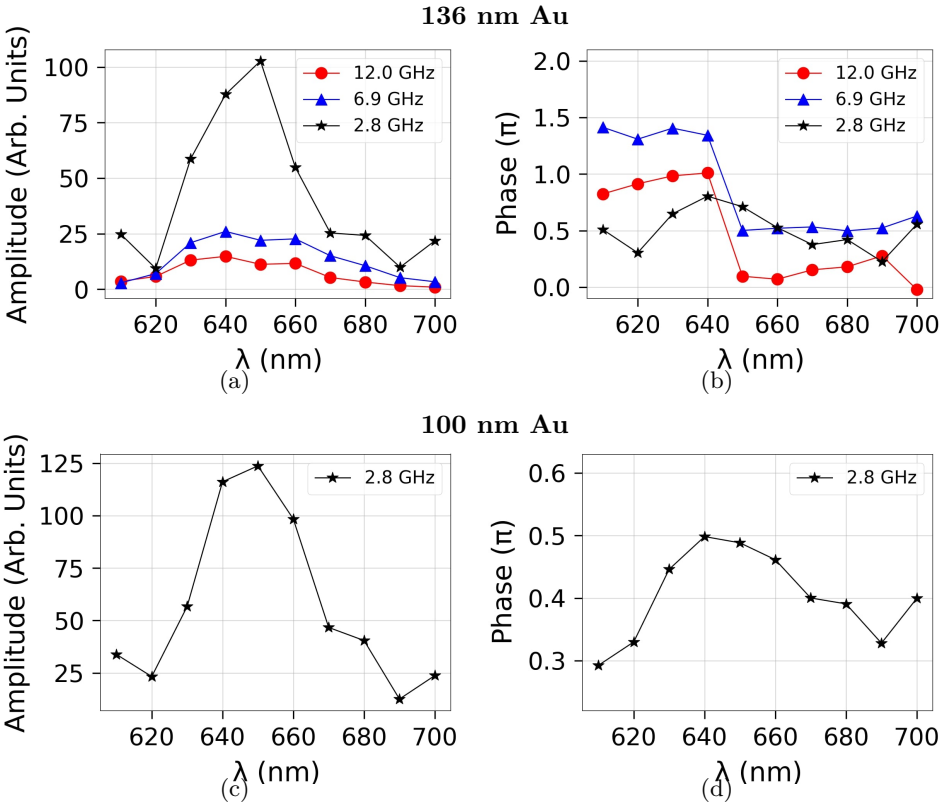

Figure 4.9: (a) Amplitude of the reflection changes induced by the acoustic echoes as a function of wavelength, measured for the 136 nm thick sample and (c) for the 100 nm thick sample. (b) Phase of the acoustic echoes for the 136 nm thick sample and (d) for the 100 nm thick sample. The color and the symbols of the curves correspond to the frequency indicated by the vertically dashed lines with the same color and symbol as shown in Fig. 4.8.

4.4 Discussion

From our results, as discussed in the previous section, we can see that the phase and amplitude of the measured photo-acoustic signals vary around the SPP resonance. Furthermore, the actual response of the amplitude and phase as a function of wavelength is different for high-frequency and low-frequency oscillations. In this section, we will first briefly attempt to identify the different types of acoustic echoes that we measure. Afterward, we will argue that these observations may be partially explained by two effects: 1) acoustic-wave-induced changes in the free

electron density and 2) acoustic-wave-induced grating deformations.

4.4.1 Acoustic echoes

As mentioned before, in our experiments we measure the presence of multiple acoustic frequencies. For a Au thickness of 177 nm we measure strong peaks around 9.1 GHz, 2.8 GHz, and 6.9 GHz, see Fig. 4.6(b). We attribute these to longitudinal waves (LW), surface acoustic waves (SAW), and grating line quasi-normal modes (NM), respectively, and we discuss them briefly below.

Longitudinal Wave
A longitudinal acoustic wave is generated due to rapid heating of the lattice via energy transfer from the heated electron gas, causing rapid expansion of the lattice. This expansion of the lattice launches an acoustic wave that bounces back and forth between the Au/SiO_x interface and the air/Au interface, losing energy each time it reflects off the Au/SiO_x interface via partial transmission into the substrate. Near-field calculations show that most of the optical energy is deposited in the lines of the grating, but light also reaches the top of the spaces, in between the lines. This makes it plausible that LW waves are generated there too. As the grating has the same thickness everywhere, we expect the LW's to have the same frequency in the lines and spaces. It's possible, and even likely, that acoustic diffraction will occur near the line edges, but this is currently not taken into account.

The spatial extent of the acoustic wave is determined by the electron energy diffusion depth [90], which is about 150 nm for Au [77]. This causes the generation of two counter-propagating waves with a wavelength of approximately twice the layer thickness that form a standing wave with a node in the middle of the layer. This leads to a periodic expansion and contraction of the whole layer. The oscillation frequency of such a wave can be found using the longitudinal speed of sound, $V_l = 3.2 \times 10^3$ m/s, and the thickness of the gold layer, d. Based on this we calculate that the longitudinal echo should have a frequency of $V_l/2\mathrm{d} = 9.04$ GHz, 11.76 GHz, and 16.0 GHz for the 177 nm, 136 nm, and 100 nm thick sample, respectively. Considering the close proximity of the frequencies for the 177 nm and 136 nm sample with our measured frequencies of 9.1 GHz and 12.0 GHz, we attribute these frequencies to a longitudinal standing wave. For the 100 nm sample thick sample, the longitudinal wave frequency equals $f_{lw} = 16.0$ GHz. However, due to the low amplitude of this oscillation in comparison to the SAW and due to the apparent higher damping rate, this frequency is not clearly visible in the FFT shown in Fig. 4.8(d).
In the 177 nm and the 136 nm thick sample, we measure a dip in the amplitude of the reflection change induced by the longitudinal echo when the probe is tuned to

the SPP resonance, as can be seen in Fig. 4.7(a) and 4.9(a). We also measure an increase in the reflection change from the longitudinal echo for both thicknesses on the slopes of the resonance at a wavelength corresponding to 640 and 660 nm.

Surface Acoustic Wave

A surface acoustic wave is an acoustic wave that travels along the surface of the material. A surface acoustic wave can be excited if there is a spatial inhomogeneity in either the excitation profile [59, 112–114] or in the surface topography [109]. However, such a wave is not necessarily confined to the surface. The type of SAW potentially present in our experiment are a Rayleigh wave, a Lamb wave, or a shear wave.

A Rayleigh wave has a finite penetration depth into the metal [61, 110]. For a bulk Au layer, we can calculate that relative vertical displacement of such a wave reaches a value of $1/e$ at a depth of 275 nm [62], which exceeds all layer thicknesses reported in this paper. This indicates that it is unlikely that our measured SAW is a pure Rayleigh wave.

A Lamb wave is, generally speaking, a wave which is confined by two free surfaces and can be viewed as a guided mode [63]. Since our Au layer is not confined by two free surfaces but rather a Au/SiO_x and Au/Air interface the presence of a Lamb wave seems unlikely. A shear wave is a wave that travels through the entire bulk with a k-vector parallel to the surface, similar to a Rayleigh and Lamb wave [62]. A shear wave displaces the lattice orthogonal to its k-vector. By definition, it is a property of a shear wave that it does not alter the density of the material [62]. This would seem to be in agreement with the fact that the SAW signal does not peak at the slopes of the SPP resonance, which would be the case if it were sensitive to density changes, as we will explain below. The velocity of a shear wave equals the transverse sound velocity [62], which for gold equals approximately 1200 m/s [115]. When a periodic structure is present on a surface, the periodicity of the surface structure determines the wavelength of the dominant surface wave [45, 66], which in our experiments equals 440 nm. Taking the velocity and the periodicity into account, the predicted frequency of the SAW equals $f_{SAW} = 2.7$ GHz. Considering the close proximity of the calculated frequency to the 2.8 GHz signal observed for all our measured thicknesses, the excited and measured SAW is most likely a shear wave.

Grating Line Quasi-Normal Mode

A grating line normal mode is the expansion and contraction of individual isolated metallic bars. Here, considering that the lines are attached to a gold layer, we think it is more appropriate to speak of quasi-normal modes. Under similar experimental conditions, the grating line quasi-normal mode for 1-dimensional Au rectangular bars with a 50 % duty cycle, a thickness of 40 nm, and a pitch of 400

nm on a quartz substrate has been measured at 7.78 GHz [110] by Lin et. al. If we extrapolate from their data to a grating amplitude of 50 nm, we find a normal mode frequency of 7.1 GHz, which is close to our measured frequency of 6.9 GHz. Discrepancies between our measured frequency and the calculated frequency from Lin et. al. are probably caused by the fact that we have a Au substrate for our Au bars, instead of quartz. Furthermore, our periodicity and duty cycle are slightly different from those of Lin et. al. The effect of this is difficult to predict precisely. Nevertheless, it seems plausible to attribute the 6.9 GHz frequency to the grating line quasi-normal mode.

4.4.2 Acoustically induced SPP resonance frequency variations

In this section, we will describe two possible ways by which the SPP resonance frequency can shift due to the presence of acoustic waves. They are acoustically induced electron density changes, and acoustic-wave-induced grating deformation. A strongly exaggerated schematic depiction of this process of shifting the SPP resonance is shown in Fig. 4.10. The acoustic echoes can both decrease and increase the SPP resonance frequency, as we will explain below. Therefore, the SPP resonance will periodically oscillate around the unperturbed resonance wavelength. Note that the presence of an acoustic wave might also possibly influence the interband transitions of our sample [43, 44], altering the dielectric function across the entire spectrum. We are currently unable to calculate the effect of the density changes on the frequency and strength of the interband transitions.

Acoustical-wave-induced electron-density changes
In our setup, the acoustic wave-induced electron density changes cannot directly be measured. However, to test the hypothesis that the change of the free electron density can give rise to the optical response that we observe, we can calculate the shift of the plasmonic resonance wavelength as a function of the electron density. The main principle behind this hypothesis is that many types of acoustic waves consist out of propagating regions of higher and lower material density. The electron density will semi-instantaneously follow the acoustic induced lattice density changes to maintain charge neutrality [55]. Changes in the free electron density will in turn change the plasma-frequency $\omega_p = \sqrt{N_e e^2/\epsilon_0 m}$, where N_e is the free electron density, e the electronic charge, ϵ_0 the vacuum permittivity of space and m the effective electron mass. Changes in the plasma frequency cause changes in the dielectric constant and, thus, the position of the SPP resonance.

To successfully excite a surface plasmon, the sum of the scalar value of the x-component of the probe wave vector and the grating wavenumber must be equal to the plasmonic wavenumber [116]. The SPP excitation condition then is,

$$\left|\frac{\lambda_0}{2\pi}\sin\theta \pm N\frac{2\pi}{\Lambda}\right| = k_{SPP} = \frac{\lambda_0}{2\pi}\sqrt{\frac{\epsilon_m\epsilon_d}{\epsilon_m+\epsilon_d}}, \tag{4.1}$$

where λ_0 is the vacuum wavelength of the light, θ the angle of incidence with respect to the surface normal, N the plasmonic order which, under our experimental conditions, is 1, Λ the grating pitch, k_{SPP} the SPP wavenumber, and ϵ_m and ϵ_d the frequency-dependent dielectric functions of the metal (gold) and the dielectric (air) respectively. For convenience, we will assume that the imaginary parts of the dielectric functions are small compared to their real parts and can, therefore, be neglected. The dielectric constant of air, ϵ_d, is taken as 1. For a given Λ and θ, Eq. (4.1) allows us to determine the SPP resonance wavelength. Furthermore, from Eq. (4.1) it is clear that the SPP resonance wavelength is dependent on the dielectric function of the material. If the dielectric function of the metal would change due to an external perturbation, such as an acoustic wave, the plasmon resonance wavelength will shift [96, 101, 102, 107, 117].

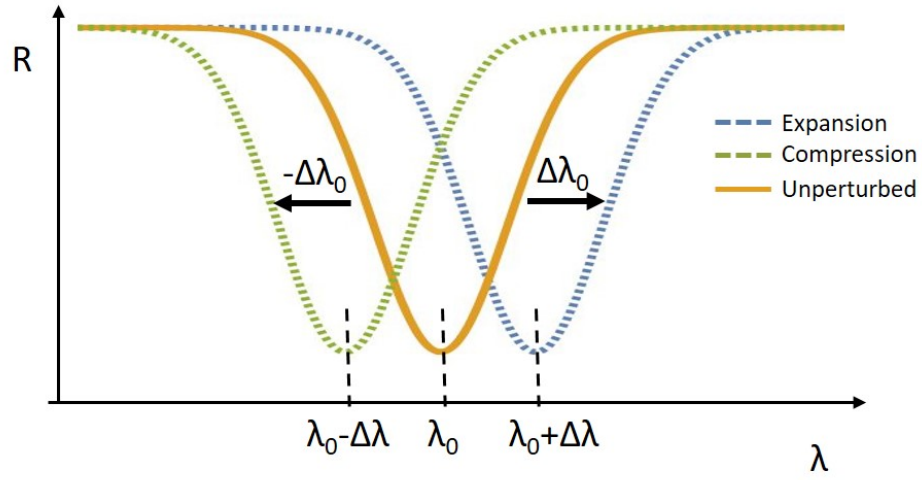

Figure 4.10: Schematic representation of the acoustically induced change in the SPP resonance. Compression due to the acoustic echo causes the SPP resonance wavelength to decrease whilst expansion causes the SPP resonance wavelength to increase.

Looking at Fig. 4.6(b), as discussed before, we measure multiple acoustic frequencies. The frequencies of 2.8, 6.9, and 9.1 GHz have been tentatively identified as a surface wave, a grating line quasi-normal mode, and a longitudinal wave, respectively. When the SPP resonance oscillates due to the presence of an electron

density perturbation, this should result in a π-phase shift of the reflection change when the reflection is measured above compared to below the SPP resonance, as can be seen in Fig. 4.10. When we look at the phase of the reflection changes, as shown in Fig. 4.7(b), we see that such a phase shift is only present for the 6.9 and 9.1 GHz frequencies and *not* for the 2.8 GHz frequency. This could indicate that the LW and NM mode both induce electron density changes, resulting in oscillations of the SPP, whereas the SAW does not induce electron density changes. This is consistent with the assumption that the 2.8 GHz wave is indeed a shear wave since a shear wave does not induce density changes.

In the presence of the longitudinal and quasi-normal acoustic modes, the lattice density will change depending on the displacement of the atoms. Using an advanced 2D numerical model [59] which incorporates the generation and propagation of acoustic waves in single *flat* Au layers, we are able to calculate that the expansion and contraction under our experimental conditions equal approximately $\pm$ 150 pm. It is not unreasonable to assume that similar expansion and contraction amplitudes are present in our grating structure. This expansion and contraction results in electron density oscillations with maximum values between $0.999 \times N_{e,0}$ and $1.001 \times N_{e,0}$, where $N_{e,0}$ is the unperturbed electron density. These oscillations in electron density result in a change of the dielectric function through the plasma frequency, which would be probed in a volume determined by the penetration depth of the probe light in our experiment. If we use this acoustically altered dielectric function in Eq. (4.1) we find that the maximum plasmon resonance wavelength shift, $\Delta\lambda_{0,max}$, equals 0.05 nm. Although such a shift seems small, we calculate that it results in a reflection change of approximately $\pm$ 0.2 % at a wavelength of 640 nm. If we look at Fig. 4.4 we see that this is close to the amplitude of our measured oscillatory reflection changes. A similar argument holds for reflection changes measured for different probe wavelengths.

Acoustic wave induced grating deformations
In addition to electron density variations, acoustic waves also alter the grating structure. Displacement of the atoms by the acoustic waves results in a change of the grating amplitude and the duty cycle, both of which are known to influence the SPP resonance and, thus, the wavelength-dependent reflection [118]. Numerical simulations were performed to see the effect of grating amplitude changes and duty cycle changes on the SPP resonance. The numerical calculations were performed using "Cyclops", an in-house developed program that solves Maxwell's equations [119]. It is based on the finite element method described by Lalanne et al. [120] and was tested and benchmarked against other methods such as the finite-difference time-domain method.

To calculate the shift of the SPP resonance as a function of grating depth and

duty cycle, 2D simulations were performed for optical wavelengths ranging from 300 to 800 nm for different grating amplitudes. In Fig. 4.11 we plot the SPP resonance wavelength as a function of grating amplitude. We note that around our grating amplitude of 47 nm, the dependence of the SPP resonance on the grating amplitude is almost linear. From these calculations, we extract that the $\Delta\lambda_{SPP}/\Delta A = 2.25$, where ΔA is the change in grating amplitude. For the duty cycle, we can look at how much the SPP resonance shifts as a function of the valley width. A similar analysis as with the grating amplitude shows that $\Delta\lambda_{SPP}/\Delta d_v = 0.25$, where d_v is the width of the valley of the grating.

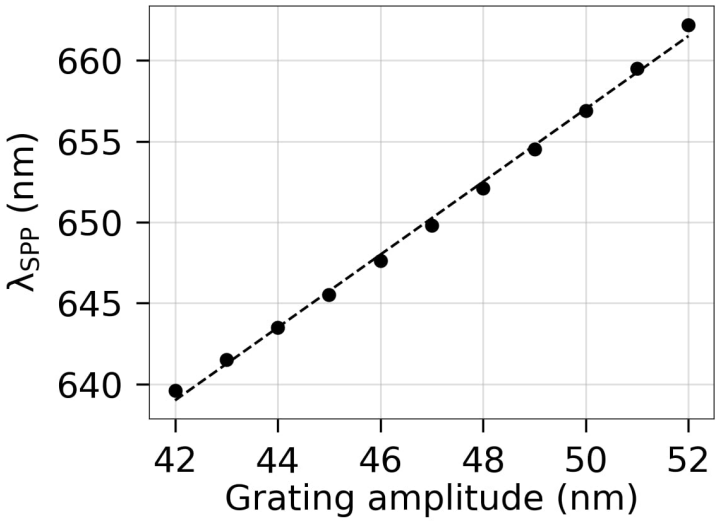

Figure 4.11: SPP resonance wavelength λ_{SPP} as a function of the grating amplitude for a gold thickness of 177 nm, computed via simulation. The dashed curve represents a linear fit to the data.

From this, we conclude that relative grating amplitude variations shift the SPP resonance more than relative duty cycle variations. The amplitude of the grating can only change when there is a difference in acoustic-wave induced vertical expansion/contraction in the valleys and the ridges of the grating. We cannot assume a priori that the ridges and valleys expand and contract with the same phase and amplitude. Such differences in the grating amplitude can, in fact, arise due to differences in absorption of the pump light in the ridges and valleys of the grating. The calculated spatial distribution of the light absorption, as shown in Fig. 4.12, demonstrates that there is indeed a difference in the amount of absorbed light in the valleys and ridges of the grating. In gold, electron energy diffusion

is rapid but does not *fully* homogenize the temperatures in our grating structure. Therefore, we expect that different lattice temperature changes in the ridges and the valleys of the grating are likely. We can thus expect acoustically induced vertical expansion differences between the ridges and the valleys of the grating. We calculate that in order to induce reflection changes with a similar magnitude as seen in our measurements, the grating amplitude would have to change with a maximum amplitude of only ± 35 pm, which is plausible.

Both the electron density variation and changes in the grating amplitude are suitable candidates to explain our measured results. We cannot currently exclude either model as an explanation for the effects we observe when probing around the SPP resonance.

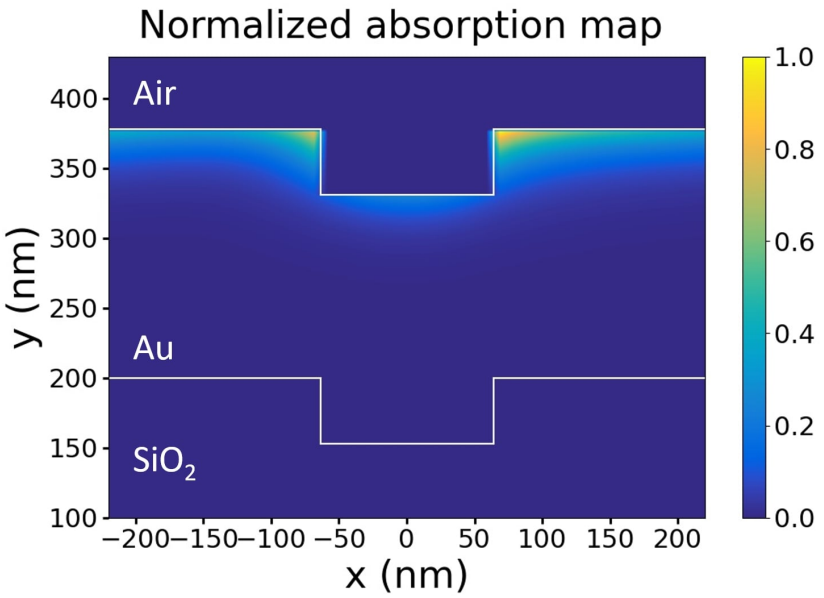

Figure 4.12: Simulated normalized absorption of the 400 nm pump beam. We find that the absorption is mostly localized on the ridges of the grating. For clarity the absorption in air is not shown.

4.5 Summary

We have studied the generation and detection of acoustic waves on a plasmonic grating. We have shown time-dependent reflection changes caused by acoustic echoes of which the detection was enhanced at probe wavelengths around the SPP resonance. We demonstrate the simultaneous presence of multiple acoustic

waves, of which the most prominent are the longitudinal, quasi-normal, and surface acoustic wave modes. Our measurements show an enhancement of the longitudinal and the quasi-normal mode induced reflection changes by a factor of 10 on the slopes of the resonance and an enhancement of the surface acoustic wave mode on the peak of the resonance by a factor of 20, compared to the measurements with a probe wavelength on the wings of the resonance.

Using a simple model that calculates the shift of the SPP resonance as a function of electron density we are able to reproduce the magnitude and the phase of the reflection changes for the longitudinal and normal modes. Besides the presence of electron density variations, we also argue that acoustic-wave-induced grating deformations may play a significant role in the measured reflection changes. Both proposed mechanisms are capable of explaining our measured results. There is no a priori reason to assume that these two effects do not both influence the measured reflection change simultaneously, although our results do currently not allow us to determine which one dominates.

5 Plasmonic enhancement of photoacoustic strain-waves on gold gratings*

In this chapter, we report on the time-dependent strain-wave-induced changes in the reflection and diffraction off a gold plasmonic grating. We demonstrate efficient excitation of strain waves using enhanced absorption at and around the surface plasmon polariton resonance. In addition, we observe that the strain-wave-induced changes in the reflection and diffraction of the grating show an approximately quadratic dependence on pump fluence. We tentatively attribute this non-linear behavior to strain-induced nonlinear changes of the interband transition energy. Using a model which calculates the permittivity of the gold taking into account the d to s/p interband transition, we deduce that the interband transition energy would have to change by about 0.013 eV to account for the measured changes in reflection.

*This chapter has been submitted as a research article to AIP Advances

5.1 Introduction

The ability of ultrafast lasers to generate strain waves in thin metal layers has been investigated extensively in the past [36, 59, 85]. Compared to light, the advantage of laser-induced strain waves is that they can travel through optically opaque materials, giving access to a multitude of material properties and physical phenomena [31–34, 37–48, 89, 121, 122]. Laser-induced strain waves find applications in many fields, such as the detection of buried structures [28–30, 90, 123] and photo-acoustic imaging [124, 125]. They also show promise for applications in the semiconductor manufacturing industry for wafer alignment. The presence of strain waves can be detected by measuring changes in the optical properties of the material or by measuring the physical displacement of surfaces and interfaces caused by these waves. Changes in the optical properties can be extracted by either measuring reflection and transmission changes [85], or by measuring diffraction [46, 91]. Generally speaking, strain-wave-induced optical changes are small. Therefore, there is a clear need to enhance the optical response to laser-induced strain waves.

In the previous chapter, we showed that the detection of laser-induced strain waves can be enhanced by probing the effect that they have on a surface plasmon polariton (SPP) resonance [126]. In this way, we were able to show optical signal enhancements of up to a factor of twenty in response to a strain wave. Improving the optical signal strength is important for applications, as this decreases the time needed to obtain a good signal-to-noise ratio. It is interesting to realize that, in principle, an SPP resonance can also be used to increase the amplitude of the strain wave itself in the generation process. This is possible because SPP excitation is accompanied by significantly stronger optical absorption. This would allow the generation of stronger strain waves, also at wavelengths where flat metals normally do not absorb much light, i.e., in the near-infrared and infrared region of the spectrum. It would also provide more flexibility in the choice of the wavelength of the light source used for the strain wave generation and/or lower the power requirements for the light source.

Here, we show how grating-coupled SPPs can be used to efficiently *excite* strain waves on gold gratings. In our experiments we excite SPPs on a gold grating with a period of 440 nm and an amplitude of 47 nm, using ultrashort laser pulses with central wavelengths around the SPP resonance at 650 nm. The pump pulses generate several types of strain waves which are detected by measuring the strain-wave induced reflection and diffraction changes of a synchronized probe pulse with a central wavelength of 400 nm. We find that the pump-induced reflection and diffraction changes reach fairly large values of nearly half a percent, significantly

more than what can be achieved on a flat metal surface using transient-grating excitation [127]. Surprisingly, we find that the strain-wave-induced optical changes scale roughly quadratically with the incident pump fluence, where a linear relation is expected. We tentatively attribute this to non-linear changes of the interband transition energy via strain-induced changes to the band structure of the gold. Our results show that SPPs can be used to more efficiently excite strain waves on structured metal surfaces.

5.2 Experimental setup

A schematic drawing of the experimental geometry is given in Fig. 5.1. A more detailed explanation and drawing of the entire setup can be found in Ref. [126]. The output of an amplified Ti:Sapphire laser (Astrella, Coherent) with a repetition rate of 1 kHz, a central wavelength of 800 nm, a pulse length of 35 fs, and an average power of 6 W is split into two using an 85/15 beamsplitter. The stronger beam (pump beam) travels through a three-stage optical parametric amplifier (OPA, HE-TOPAS, from LightConversion). The OPA generates tunable infrared laser pulses with central wavelengths ranging from 1200 to 1400 nm with a maximum pulse energy of about 1 mJ. Afterward, the beam is frequency-doubled using a β-Barium Borate (BBO) crystal generating pulses with a central wavelength tunable from 600 nm to 700 nm. The beam passes through a mechanical chopper which is synchronized with the 1 kHz pulse train from the laser. With a 50 % duty-cycle, the chopper reduces the repetition rate of the pump to 500 Hz, so that every other pump pulse is blocked. Finally, the beam is focused onto the sample to a spot with a diameter of 600 µm. The pump beam illuminates the sample under an angle of approximately 21 degrees such that the SPP resonance is located at 650 nm.

The weaker beam (probe beam) passes through a variable optical delay line after which it is frequency-doubled, using another BBO crystal, to a central wavelength of 400 nm. The beam is then focused onto the grating under a five-degree angle of incidence to a spot with a diameter of about 300 µm. The polarization of the electric field of the probe beam is perpendicular to the grating lines. The reflection and diffraction of the probe beam are measured using silicon photodiodes. In an unperturbed state, the grating reflects and diffracts 18 % and 11 % of the probe beam, respectively.

The samples are made by thermally evaporating gold layers on top of a commercially available SiO_x grating on Si (NanoPHAB B.V.). To create the grating, 200 nm SiO_x is deposited on top of a Si substrate. Afterward, the grating pattern is formed by electron beam lithography and is etched into the SiO_x using reactive-ion etching. An atomic force microscopy (AFM) image of the grating structure after

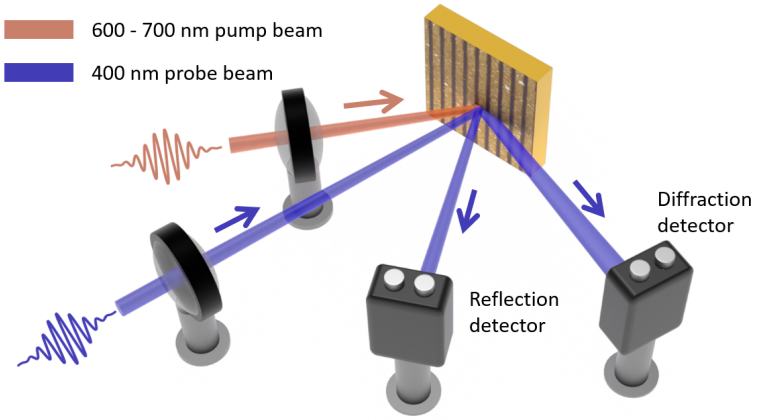

Figure 5.1: Schematic drawing of the experimental geometry. The 500 Hz repetition rate, tunable 600 - 700 nm central wavelength pump pulses illuminate the sample under an angle of 21 degrees, such that they excite the SPP resonance at 650 nm. The 1 kHz repetition rate, 400 nm central wavelength time-delayed probe pulses illuminate the sample under an angle of incidence of five degrees. Both the reflection and diffraction changes of the probe pulse are measured as a function of the time delay between the pump and probe pulses. Projected onto the sample, we show an AFM image of the gold grating, with a layer thickness of 139 nm, a pitch of 440 nm, and a duty cycle of 71 %.

gold deposition is shown in Fig. 5.1. After deposition, the Au layer thickness is 139 nm. The duty cycle, pitch, and amplitude of the grating have been measured to be 71 %, 440 nm, and 47 nm, respectively, using AFM measurements.

5.3 Results & Discussion

For all pump-probe measurements discussed below, the beam diameters at the surface of the sample of both pump and probe were kept constant with a full width at half maximum (FWHM) beam diameter of 600 µm and 300 µm, respectively. The probe pulse fluence was kept constant at a relatively low fluence of $2.8 \times 10^{-4}\,\mathrm{J/cm^2}$.

Pump-induced probe reflection changes

In Fig. 5.2 we show the pump fluence dependence of the measured reflection changes from the probe beam with polarization orthogonal to the grating lines. We

illuminate the sample using three different pump wavelengths of 640, 650, and 660 nm, which are below, on, and above the SPP resonance wavelength, respectively. At t = 0, we measure a pulse-length-limited decrease in reflection directly after excitation, governed by electron dynamics [52, 77]. Afterward, the electrons will cool to the lattice via the emission of phonons. This results in rapid heating of the layer, which causes a thermal stress to form. The growth of the thermal stress then launches a strain wave. Due to the geometry of the sample, multiple types of acoustic waves are launched, each having its own frequency. These different types of acoustic waves are described in more detail elsewhere [126]. Briefly, we identified a longitudinal wave (LW), a surface acoustic wave (SAW), and a grating-line-normal mode (NM). These different types of strain waves result in both relatively low and high-frequency time-dependent reflection changes.

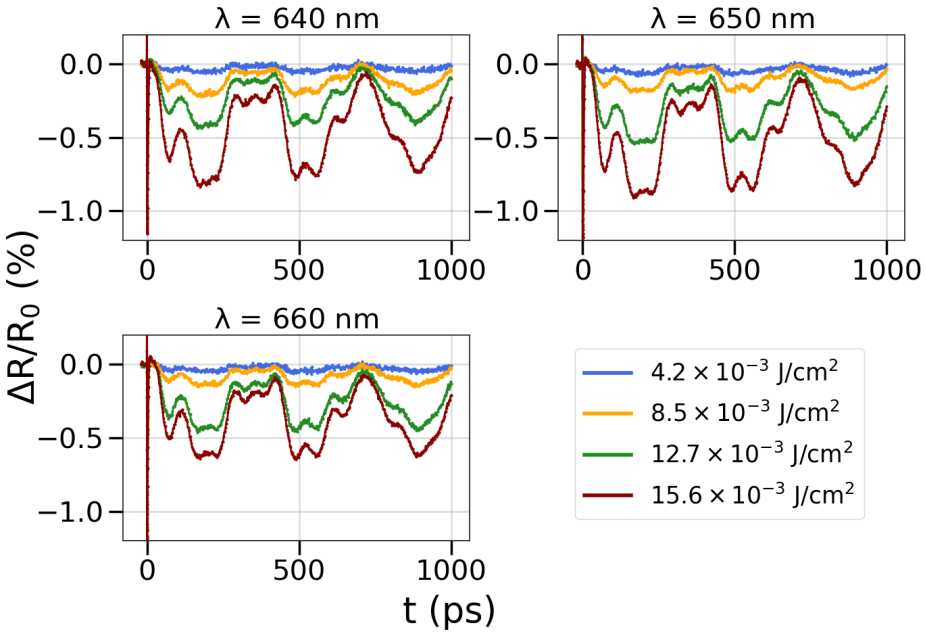

Figure 5.2: Pump-induced reflection changes from a gold grating measured with a 400 nm central wavelength probe beam for different excitation fluences, and for pump wavelengths below (640 nm), at (650 nm) and above (660 nm) the SPP resonance.

We measure remarkably strong strain-wave-induced reflection changes, with a magnitude of approximately 0.7 % for the highest pump fluences used in our experiments. The signal is strongest when the pump beam is exactly tuned to the SPP resonance and becomes smaller when the pump is tuned to wavelengths

above or below the resonance. This is consistent with the fact that when the wavelength is tuned to the resonance, the absorption is strongest, leading to a stronger strain wave. As mentioned before, we launch multiple types of acoustic waves, each with its own frequency. We can determine the strain-induced signal strength for each frequency from the fast Fourier transform (FFT) of the time-dependent data. From the FFT we extract four prominent frequencies, located at 2.8 GHz (SAW), 7.0 GHz (NM), 10.0 GHz (unknown), and 12.0 GHz (LW). In Fig. 5.3 we show the magnitude of these four most prominent frequencies as a function of pump fluence for all pump wavelengths. Surprisingly, we notice an approximately quadratic increase of the strain-induced reflection changes for all measured frequencies.

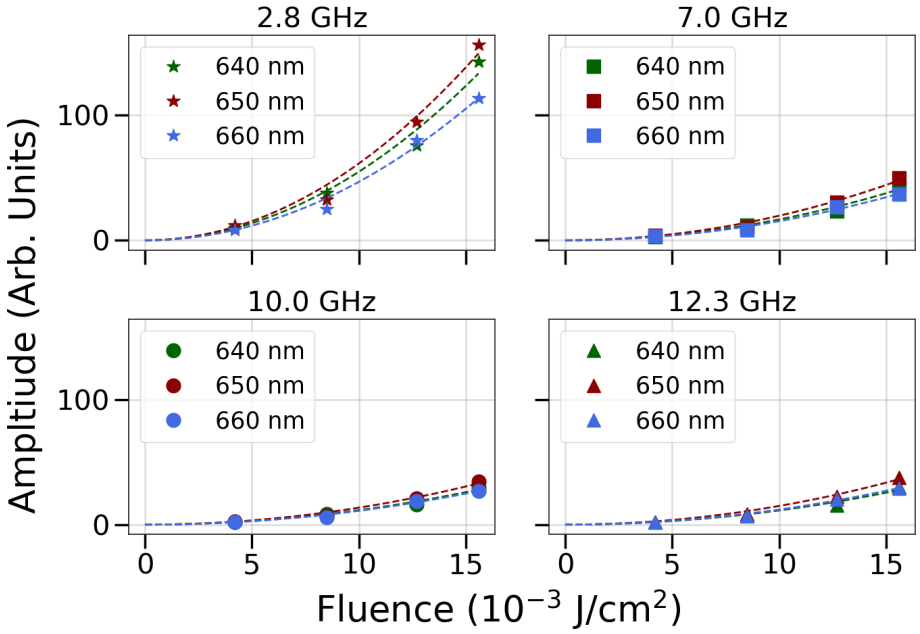

Figure 5.3: FFT amplitudes of the four most prominent frequencies as a function of incident pump fluence for three different pump wavelengths. The dashed lines going through the data points, represent quadratic fits to the data. The agreement between the data and the fit indicates that the amplitude of the strain-induced reflection changes scales non-linearly with the incident pump fluence, for all measured frequencies.

To better understand the observed non-linear behavior of the signal strength versus pump power, we first have to determine whether the non-linearity occurs in the generation process or in the detection process. A non-linear response in the

generation of the strain wave could be the result of the non-linear absorption of the pump beam by, for example, two-photon absorption [128]. However, by measuring the absorption of the gold grating as a function of incident power, we find that, within our measurement accuracy of approximately 1 %, the absorbed pump energy scales linearly with the incident pump energy for all pump fluences up to the highest pump fluence used in the experiments of 1.6×10^{-2} J/cm^2. Independent of the incident pump fluence, approximately 65 % of the pump energy is absorbed. Note that this is much more than what is typically absorbed by a flat gold surface at a wavelength of 650 nm, and shows the enhanced absorption caused by the SPP resonance.

Another potential non-linear effect in the generation process is that the magnitude of the generated strain might scale non-linearly with the incident pump power. Using a one-dimensional model developed by Thomsen et al. [60, 127], we can calculate the time-evolution of laser-induced strain waves as a function of absorbed pump power. From these calculations, we find that, within the range of our experimental pump fluences, the generated strain scales linearly with the absorbed laser power (not shown here). Since the strain scales linearly with the amount of absorbed energy, the non-linearity of the measured reflection changes versus pump power most likely arises from the way the strain waves are *detected*.

It has been shown that strain can directly change the band-structure of materials [129–133], even in such a manner that strain can induce semiconductor-to-metal transitions [134–137]. Furthermore, it has been demonstrated that strain can increase or decrease the bandgap and interband transition energy of materials [138–143], also in a non-linear manner [144]. For gold in particular, the interband transition from the d-band to the hybridized s/p-band is very sensitive to strain [145,146]. In our experiments, the probe wavelength is 400 nm and thus we excite electrons from the d-band to the hybridized s/p-band [52]. We speculate that the strong non-linear reflectivity changes versus pump power are due to strain-induced changes in the interband transition energy.

We can estimate how much the interband transition energy in gold has to change to reproduce the magnitude of our measured reflection changes, using a dielectric function that takes into account interband transitions from the d-band to the hybridized s/p-band. This function is given by, [147–150]

$$\epsilon(\omega) = \underbrace{\epsilon_\infty - \frac{\omega_p^2}{\omega\left(\omega + \frac{i}{\tau_c}\right)}}_{\epsilon_{intra}} \underbrace{-\frac{4\pi e^2}{m^2\omega^2} \sum_{\mathbf{k}\mathbf{k}'bb'} \frac{\left(\hbar\omega + \frac{i}{\tau_{bb'}}\right) \left\langle b\mathbf{k}|p_i|b'\mathbf{k}'\right\rangle \left\langle b'\mathbf{k}'|p_i|b\mathbf{k}\right\rangle}{(E_{b'k'} - E_{bk})\left(E_{b'k'} - E_{bk} - \hbar\omega - \frac{i}{\tau_{bb'}}\right)} (f_0(E_{b'k'}) - f_0(E_bk))}_{\epsilon_{inter}} \tag{5.1}$$

where ϵ is the frequency-dependent permittivity, consisting of two terms ϵ_{intra} and ϵ_{inter}, which describe the contributions by intraband and interband transitions to the permittivity, respectively. ϵ_∞ is a constant contribution to the dielectric function due to all other bound transitions, ω_p is the plasma frequency, e is the electronic charge, m the effective electron mass, $\hbar$ the reduced Planck's constant, $\mathbf{k}$ the momentum of an electron in band b, τ_c is the inverse intraband damping rate, τ_{bb} is the interband equivalent of τ_c, $\left\langle b\mathbf{k}|p_i|b'\mathbf{k}'\right\rangle \left\langle b'\mathbf{k}'|p_i|b\mathbf{k}\right\rangle$ is the transition matrix element, E_{bk} is the energy of an electron in band b with momentum $\mathbf{k}$ and f_0 is the Fermi distribution.

For gold, we can approximately describe the d-band as a completely filled flat band and the s/p-band as a half-filled parabolic band. The momentum-dependent energy of the bands is approximated by [148],

$$E_{d,k} = 0, \tag{5.2}$$

$$E_{s/p,k} = \frac{\hbar^2 k^2}{2m} + \Delta, \tag{5.3}$$

where Δ is the interband transition energy. If we plug Eqs. (5.2) and (5.3) into Eq. (5.1), we end up with a dielectric function that depends on the interband transition energy. We then calculate the reflection from the dielectric function.

In Fig. 5.4(a) we show the calculated $\Delta R/R$ as a function of Δ. In the regime of the reflection changes measured in our experiments, we find that the reflection changes scale linearly with Δ. In Fig. 5.4(b) we show the maximum interband transition energy Δ_{max} required to account for the measured maximum reflection changes, versus the pump fluence. We find that the maximum strain-induced change of the interband transition energy needed to obtain the highest measured

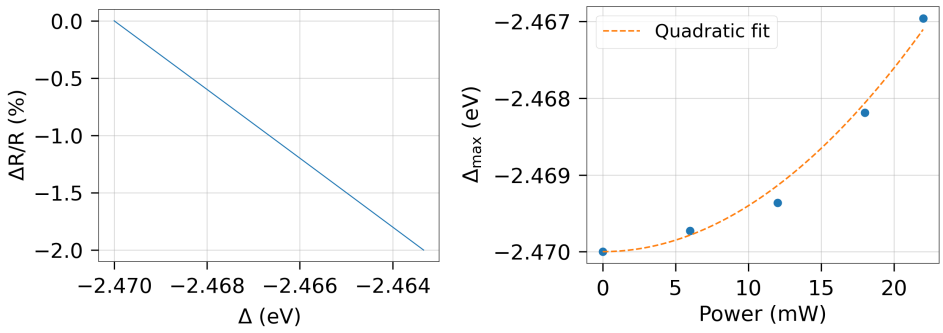

(a) (b)

Figure 5.4: (a) Calculated change in reflectivity as a function of interband transition energy. (b) Calculated required maximum change of the interband transition energy, Δ_{max}, induced by the longitudinal strain needed to retrieve the magnitude of our measured reflection changes. We see that Δ_{max} has to change by only 0.013 eV to account for the measured reflection changes. The dashed line is a quadratic fit to the data and serves as a guide to the eye.

reflection change, is approximately 0.013 eV. Since the strain scales linearly with the incident power and the reflection changes scale linearly with Δ, we conclude that Δ would have to scale approximately quadratically with the strain to explain our data. We caution that the model we used here assumes that the strain only affects Δ. In reality, it seems likely that the strain also influences the shape of the band structure itself. Nevertheless, the calculation gives an order-of-magnitude estimate of the required maximum change in Δ and implies that this would require a roughly quadratic relation between the strain and Δ, which is not unreasonable to assume [144, 145].

Diffraction

In Fig. 5.5(a) we show a measurement of the time-dependent diffraction change and the time-dependent reflection change in the same plot. The pump wavelength equals 650 nm and the pump fluence equals $15.6 \times 10^{-3}\,\mathrm{J/cm^2}$. Note that here, in contrast to transient-grating measurements [59, 127], we measure a 0.7 % modulation of the diffraction efficiency on top of a static background diffraction from the fixed, physical grating. Even though the excitation is identical for both the reflection and diffraction measurements, the shape of the time-dependent response is different. For both reflection and diffraction, we measure a pulse-length-limited signal decrease caused by electron dynamics, with a rapid recovery within ap-

proximately 5 ps. Afterward, both the diffraction and reflection start to slowly decrease. After approximately 50 ps the diffraction change starts to increase, while the reflection starts to decrease further. From here on, reflection and diffraction behave differently.

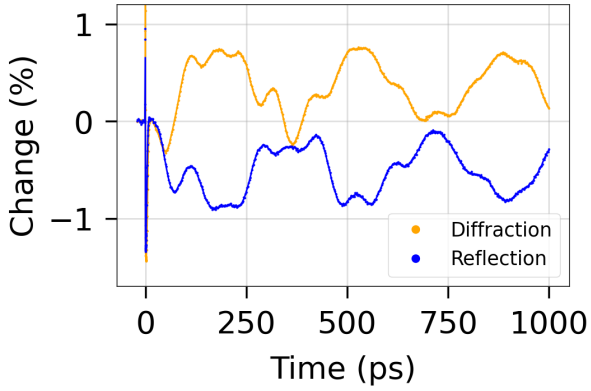

(a)

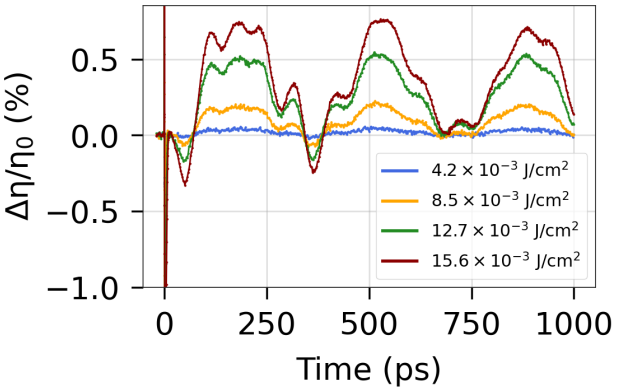

(b)

Figure 5.5: (a) Measured pump induced diffraction and reflection change of the 400 nm probe pulse from the gold grating. (b) Pump-power-dependent measurement of the strain-wave-induced diffraction changes.

For both diffraction and reflection, we measure a slow oscillation with a frequency of 2.8 GHz. However, this frequency induces diffraction and reflection changes which are opposite in sign. Compared to the reflection measurements, the higher frequency oscillations in the diffraction measurement seem to have shifted slightly from 10.0 GHz to 9.5 GHz and from 12.0 GHz to 12.7 GHz. Furthermore, the 7.0 GHz frequency which is present in the reflection spectrum, is no longer present

in the diffraction measurement. The cause of these small changes in the apparent position of the peaks as measured in diffraction is currently not well understood. Other, more subtle, discrepancies in the temporal response of the diffraction and reflection to the *same* strain wave are attributed to the fact that reflection is *only* sensitive to the strain-optic effect, while diffraction is sensitive to *both* the strain-optic effect *and* strain-induced deformation and displacement of the grating lines.

In Fig. 5.5(b) we show the pump power dependence of the strain-wave-induced diffraction changes. Similar to the pump power-dependent reflection measurements as shown in Fig. 5.2, we measure a roughly quadratic dependence of the strain wave-induced diffraction efficiency as a function of pump power. Intuitively, one would expect that the diffraction efficiency would scale quadratically with the incident power because the diffraction efficiency of a square grating scales quadratically with the grating amplitude [118]. However, this is only true in a background-free measurement, i.e. when no static background diffraction is present. This is *not* the case in our measurements since we have a static background diffraction of 11 %. It has been shown that, when a strong background field is present, such a quadratic dependence reduces to a linear dependence when the background field is much stronger than the strain-induced diffracted field, which is the case here [30]. In spite of this, we still measure a quadratic dependence of the diffraction efficiency on the pump power and attribute this to the same nonlinear change in the interband transition energy as for the reflection measurements.

5.4 Summary

In summary, we have shown efficient excitation of ultrasonic strain waves on a gold grating by using surface plasmon polaritons to enhance the coupling of the light to the grating. We measure strong time-dependent strain-wave-induced reflection and diffraction changes on the order of 0.7 %. Furthermore, we have shown that the amplitude of the measured reflection changes scales non-linearly with the fluence of the pump beam. We argue that this non-linear behavior is possibly linked with non-linear changes of the interband transition energy as a function of strain. In order to account for the amplitude of the measured reflection changes, the interband transition energy would need to decrease by 0.013 eV.

6 Ultrafast laser-induced strain waves in ultra-thin ruthenium layers ⋆

We report on the time-dependent optical diffraction from ultra-high frequency laser-induced acoustic waves in thin layers of ruthenium deposited on glass substrates. We show that the thermo-optic and strain-optic effects dominate the optical response of Ru layers to a traveling longitudinal strain wave. In addition, we show the generation and detection of acoustic waves with a central frequency ranging from 130 GHz to 750 GHz, on ultra-thin layers with thicknesses in the range of 1.2 - 20 nm. For these ultra-thin layers we measure a strong dependency of the speed of sound on the layer thickness and, thus, the frequency. This frequency dependent speed of sound results in a frequency-dependent acoustic impedance mismatch between the ruthenium and the glass substrate, leading to a faster decay of the measured signals for increasing frequency. Furthermore, for these extremely high-frequency oscillations, we find that the frequency and phase remain constant for times longer than about 2 ps after optical excitation. Back extrapolation of the acquired acoustic signals to $t = 0$ gives a starting phase of $-\pi/2$. As this seems unlikely, we interpret this as an indication of possible dynamic changes in the phase/frequency of the acoustic wave in the first 2 ps after excitation.

⋆This chapter has been published in a slightly modified form as Opt. Express **29**(20), 32051-32067 (2021)

6.1 Introduction

The study of thin films with ultra-fast laser-induced acoustic waves has seen a lot of development in the past decades. Major advancements in the fundamental understanding of photo-acoustics have been made with regards to the generation, propagation, and detection of high-frequency acoustic waves [36, 59, 85]. The ability of acoustic waves to travel through optically opaque materials has many applications, such as detection of buried structures [28–30, 123] and photo-acoustic imaging [124, 125]. Furthermore, laser-induced acoustic waves have been used to access and investigate a multitude of material properties and physical phenomena [31–34, 37–48, 89, 122].

A less well-known candidate for photo-acoustic studies is ruthenium (Ru). Ru has a relatively high electron-phonon coupling constant of 1.85×10^{18} $\mathrm{Wm^{-3}K^{-1}}$, a relatively small optical penetration depth of about 6 nm at a wavelength of 400 nm, and a relatively modest electronic thermal conductivity of 117 $\mathrm{Wm^{-1}K^{-1}}$ compared to other metals commonly used in photo-acoustic studies, such as gold and silver [54, 58]. In addition, Ru has a high melting point of 2607 K. When an ultra-short laser pulse is used to illuminate a Ru layer, these parameters suggest that significant amounts of energy can be deposited in a thin layer near the surface, leading to the generation of extremely high-frequency longitudinal strain waves. Furthermore, thin layers of ruthenium are of industrial relevance in extreme ultraviolet (EUV) lithography machines, where they are used as a capping layer on top of EUV multilayer mirrors to prevent oxidation [151–156]. Moreover, thin layers of Ru are also used to enhance the near-IR emissivity of thin membranes, or pellicles, used in EUV lithography machines to protect photomasks. Pellicles can become hot and cool typically via emission of thermal radiation [157]. There is thus a significant interest in using photoacoustics to study the material properties of Ru.

In this chapter, we show the generation of extremely high-frequency acoustic waves in ruthenium layers deposited on glass. We demonstrate that the optical response of the Ru layers to acoustic waves is mostly governed by the thermo-optic and strain-optic effects. Furthermore, we measure strain waves with frequencies as high as 750 GHz and we show that, for ultra-thin layers, the speed of sound is a strong function of layer thickness. Moreover, we observe that the decay time of the strain-wave-induced oscillations of the diffraction efficiency decreases strongly with decreasing layer thickness and, thus, with increasing strain wave frequency. We attribute this to a layer thickness (and thus a frequency) dependent acoustic impedance mismatch with the glass substrate which allows for higher transmission of the strain wave into the substrate with a corresponding faster decay of the mea-

sured signals. Finally, we demonstrate that for ultra-thin Ru layers, the frequency of the excited strain wave is stable after approximately t = 1.8-2.0 ps. However, if we extrapolate the measured strain-wave-induced diffraction, starting from 1.8-2.0 ps, back to t = 0, when both pump and probe overlap in time on the sample, we find that the extrapolated starting phase equals $-\pi/2$. This seems rather unlikely and therefore suggests that in the first 1.8-2.0 ps, dynamical changes occur in the frequency and/or the phase of the generated strain wave.

6.2 Experimental setup

In Fig. 6.1 we show a schematic depiction of the pump-probe setup. The laser system is a 1 kHz repetition rate Ti:Sapphire regenerative amplifier (Astrella, Coherent) which generates laser pulses with a central wavelength of 800 nm, a pulse energy of 6 mJ, and a pulse length of 35 fs. The laser output is split into two by a beam splitter.

The 800 nm beam reflected by the beam splitter acts as the pump beam and first passes through a variable optical delay line. The beam is frequency-doubled to a central wavelength of 400 nm using a 100 µm thick BBO crystal and passes through a mechanical chopper, reducing the repetition rate to 500 Hz. After the chopper, the pump beam passes through a 50/50 beamsplitter, creating two pump beams with equal intensity. Both beams are focused onto the sample to a spot with a diameter of approximately 500 µm. Care is taken to ensure that the two 400 nm pump pulses overlap in both space and time, creating an interference pattern on the sample. In doing so, the Ru layer is excited only in the bright fringes of the interference pattern and remains unperturbed in the dark fringes. As optical excitation modifies the optical properties of the material, this leads to a transient-grating that is capable of diffracting light. The period of the grating is determined by the 400 nm wavelength and the angle between the two beams and has a value of approximately 6 µm [78].

The 800 nm beam transmitted by the beam splitter, which acts as the probe beam, enters an optical parametric amplifier (OPA, HE-TOPAS, LightConversion). This converts the 800 nm pulses into pulses with a wavelength of 1300 nm. After the OPA, the beam is frequency-doubled to generate pulses with a central wavelength of 650 nm. This beam is then focused onto the sample to a spot with a diameter of approximately 250 µm.

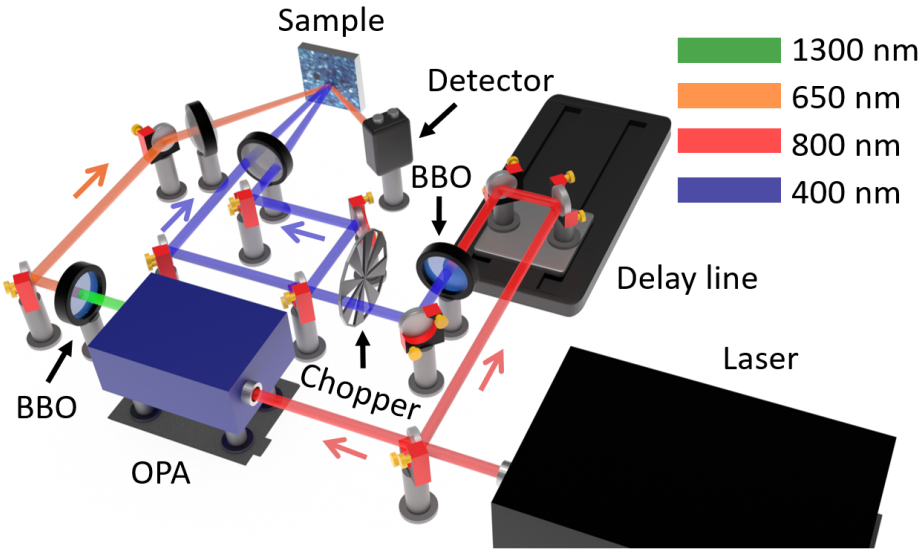

Figure 6.1: Schematic drawing of the setup used in our experiments. The output of a 1 kHz repetition rate regenerative amplified Ti:Sapphire laser is split into a pump beam and a probe beam. The pump first travels through an optical delay line after which the optical frequency is doubled using a BBO crystal. Afterward, the pump is optically chopped to reduce the repetition rate by 50%. The pump is split into two beams. These two pump beams overlap in time and, noncollinearly, in space to form an intensity grating on the Ru surface. The probe is sent to an optical parametric amplifier (OPA) set to generate a signal beam with a wavelength of 1300 nm. This beam is subsequently frequency-doubled to create a beam with a central wavelength of 650 nm. Afterward, the probe beam is focused onto the sample in the same spot as the pump pair.

The Ru layers are made by plasma-assisted sputter deposition on a chemically cleaned glass substrate. In Fig. 6.2, we show Atomic Force Microscopy (AFM) images of a 20 nm, 5.0 nm, and 2.3 nm thick Ru layer, deposited on glass. From these images, we find that the root mean square (RMS) surface roughness values are 520 pm, 580 pm, and 460 pm for the 20 nm, 5.0 nm, and 2.3 nm thick layer samples, respectively. We also took an AFM image of the glass substrate (not shown here) and obtained an RMS roughness value of 430 pm. Ellipsometry measurements on a thick 107 nm Ru layer have shown that the Ru layers have a complex refractive index of $\tilde{n} = 3.0 + 5.7i$ and $\tilde{n} = 5.9 + 6.0i$ at 400 nm and 650 nm, respectively. Furthermore, for all Ru layer thicknesses we have measured an absolute absorption between 27% and 34% at a wavelength of 400 nm.

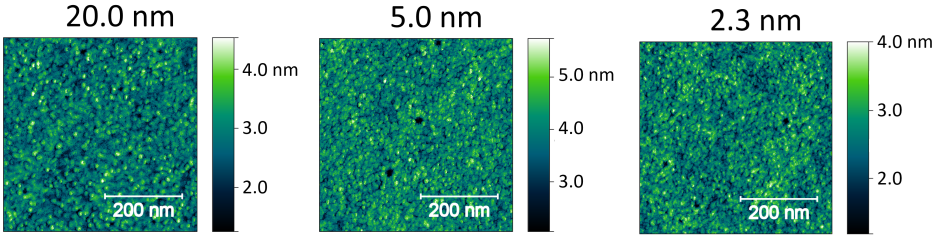

(a) (b) (c)

Figure 6.2: AFM images of three Ru layers on glass with thicknesses of 20 nm (a), 5.0 nm (b), and 2.3 nm (c). The RMS surface roughness for these thicknesses is 520 pm, 580 pm, and 460 pm, respectively.

6.3 Results & Discussion

In the transient-grating measurements discussed below, the surface area on the sample illuminated by the pump and probe beam was kept constant, for each sample. The pump power was adjusted to values below the damage threshold of each sample. It was found that thinner samples were damaged at lower fluences than thicker samples. Nevertheless, we found that the maximum laser fluences deposited on these layers before damage occurs were surprisingly high. For example, on a Ru layer of 5 nm thick, damage only occurred when each of the pump pulses incident with a 500 µm diameter spot had a fluence of 2 $\times 10^{-3}$ J/cm^2. This is most probably related to the high melting point of Ru and the fact that Ru seems to adhere to the surface of the glass very well, in contrast to a material such as gold. The probe beam power was chosen to maximize signal-to-noise, but low enough to ensure that no self-induced probe reflection changes were measured. Although we are primarily interested in thin layers with a thickness of less than 20 nm, we also performed experiments on a relatively thick layer of 107 nm Ru for comparison.

6.3.1 107 nm thick Ru

In Fig. 6.3, we plot the time-dependent normalized diffraction efficiency of a 107 nm Ru layer as a function of time delay between the pump and probe pulses. The solid line going through the data points is a running average over three data points. At t = 0 ps we measure a pulse-length-limited increase in the probe diffraction efficiency. This response is attributed to the quasi-instantaneous heating of the electron gas, creating a grating in the electron temperature [77]. Afterward, the electron gas energy thermally diffuses into the material, while simultaneously

cooling by transferring energy to the lattice via electron-phonon coupling [33,158]. This causes the lattice to heat up in the same spatially periodic manner as the incident intensity profile. Consequently, a grating in the lattice temperature is generated, which manifests itself as a background diffraction signal. The lattice energy will thermally diffuse deeper into the material, lowering the temperature near the surface where the probe pulse samples the grating to a depth roughly equal to the probe optical penetration depth of 8.5 nm. This causes the background diffraction to decay within 100-150 ps.

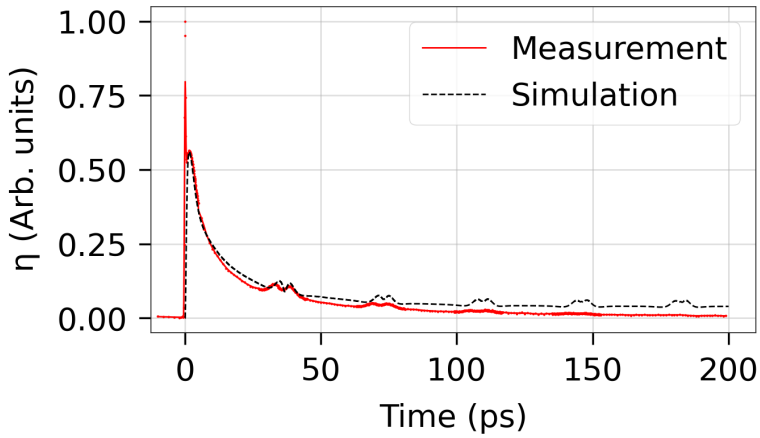

Figure 6.3: Transient-grating pump-induced diffraction efficiency of the 650 nm central wavelength probe beam on a 107 nm Ru layer deposited on glass, as a function of time. The black dashed line is a calculation of the diffraction efficiency induced by a combination of the strain- and thermo-optic effect. This calculation does not include damping of the acoustic wave or partial transmission of the wave into the glass substrate.

Superimposed on the background diffraction we measure periodic perturbations in the diffraction efficiency. These perturbations are caused by a strain wave that is launched near the surface due to rapid lattice heating which creates a thermal stress [59, 84]. The strain wave travels through the Ru layer, partially reflects off the substrate, and travels back to the Ru/air interface, where it is detected by measuring the probe diffraction. The acoustic echo can induce changes in the diffraction efficiency via both the strain-optic effect and by physical displacement of the surface [28,30,123]. From the periodicity of the acoustically induced diffraction changes, we can determine that the speed of sound for our 107 nm thick ruthenium layer is approximately 6030 m/s, which is close to the literature value for the speed

of sound in bulk Ru of 5970 m/s [159].

To simulate the strain wave-induced-diffraction, we start with the transient temperature distribution of the Ru layer after excitation with an ultrafast laser pulse. We use the two-temperature model, as described in section 2.1. In the TTM, energy exchange between the lattice and the electron gas is governed by a set of two coupled differential equations [49], given by Eqs. (2.2) and (2.3). From this set of differential equations, we see that the electron gas will absorb the energy from the laser, after which the electron gas energy will diffuse deeper into the metal, transferring energy to the lattice, thereby heating the lattice. Rapid heating of the lattice will set up a thermal stress σ_z^{th}, given by Eq. (2.20) [59,60]. In order to calculate the thermal-stress-induced-strain wave inside our Ru layers, we use Eq. (2.21), as derived by Thomsen et al. [60]. We numerically solve these differential equations given by employing a central difference method.

The periodicity of the transient-grating of 6 µm is approximately three orders of magnitude larger than the sample thickness. This could, in principle, lead to the generation of shear waves which, for the grating period in our experiment, would have a temporal period much longer than the time scale of our experiment, and can thus be ignored [126]. We numerically solve the differential equations given in Eq. (2.21) by employing a central difference method. The lattice temperature increase will also influence the diffraction via a thermally-induced spatial grating in the dielectric function, referred to as the thermo-optic effect. We can calculate how the strain-optic, thermo-optic, and surface displacement effects influence the diffraction efficiency with [60, 91],

$$\eta_{disp} = \left|irk_z h_0(t)\right|^2 \propto \left| k_z \int_0^L s_z(z,t)\ \mathrm{d}z \right|^2 , \tag{6.1}$$

$$\eta_{str} = \left|\delta r_{str}\right|^2 \propto \left| k_{str} \int_0^L \exp\left(2ik_z nz - \frac{2z}{d_p}\right) s(z,t)\ \mathrm{d}z \right|^2 , \tag{6.2}$$

$$\eta_{th} = \left|\delta r_{th}\right|^2 \propto \left| k_{th} \int_0^L \exp\left(2ik_z nz - \frac{2z}{d_p}\right) \Delta T(z,t)\ \mathrm{d}z \right|^2 , \tag{6.3}$$

$$\eta_{tot} \propto \left|irk_z h_0(t) + \delta r_{str} + \delta r_{th}\right|^2 , \tag{6.4}$$

where η_{disp}, η_{str} and η_{th} are the diffraction efficiencies induced by *only* the dis-

placement, strain and thermal effects, respectively. η_{tot} is the total diffraction efficiency from a combination of the effects caused by displacement, strain and a thermal background, r the complex optical reflection coefficient, k_z the z-component of the k-vector of the probe beam, h_0 the strain-induced displacement at the surface, L the layer thickness, δr_{str} and δr_{th} the changes to the complex reflection coefficient caused by the strain and the thermal background, respectively, k_{str} the strain-optic coefficient, n the real part of the refractive index, d_p the penetration depth of the incident probe light, and k_{th} the thermo-optic coefficient. For ruthenium, the strain-optic and thermo-optic coefficients are, to the best of our knowledge, not known and are thus used as fitting parameters in our calculations. In Fig. 6.4 we show calculations of the displacement-, strain-, and thermally- induced normalized diffraction efficiencies separately, for the 107 nm Ru layer. Note that, according to Eq. (6.4), we cannot simply add the different components of the diffraction efficiencies themselves to get the total diffraction efficiency.

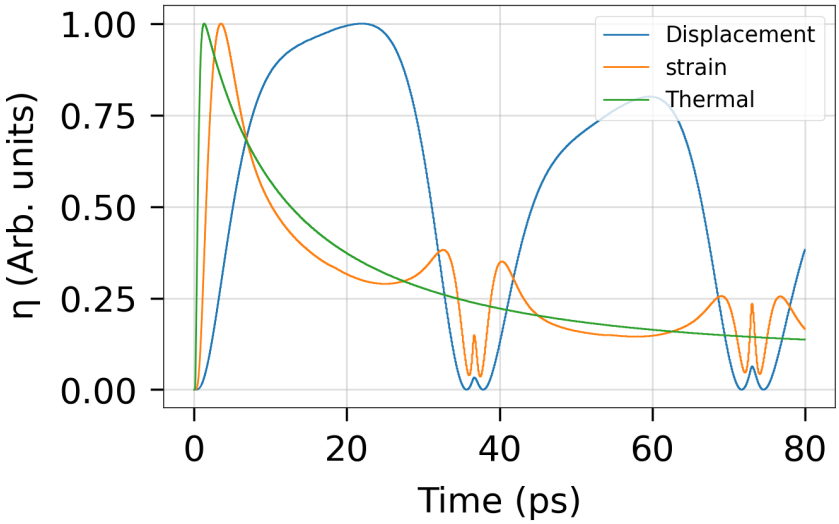

Figure 6.4: Calculated diffraction efficiency of *only* the strain-optic, *only* the thermo-optic and *only* the displacement effects. All contributions have been normalized to their respective maximum.

If we compare the shapes of the calculated diffraction curves with the measurement, we see that we find the best resemblance if we take into account only the strain-optic and thermo-optic effects. The dashed curve in Fig. 6.3 is the calculated diffraction efficiency taking only the strain-optic and thermo-optic effect into account, using the bulk literature values for the Lamé parameters. If we

take diffraction induced by surface displacement into account, agreement between the measurement and the simulation is not possible. From our simulations, we find the best agreement between the measurement and the calculations when $k_{str}/k_{th} = 4.5 \times 10^4 \times e^{1.5\pi i}$. The phase factor in this fraction represents the difference between the strain-optic and thermo-optic induced optical phase.

6.3.2 Ultrathin layers

As discussed in the previous section, in the 107 nm thick Ru layer, temporally separated acoustic echoes are measured. When the Ru layer thickness is decreased, it is no longer possible to separate the acoustic echoes in time. This is demonstrated in Fig. 6.5(a), where we plot the time-dependent diffraction efficiency of two Ru layers with thicknesses of 20 and 5 nm. The total incident pump pulse energy equals 12 µJ and 34 µJ for the 5 nm and 20 nm thick Ru layers, respectively. For both layer thicknesses, we measure a pulse-length-limited increase in diffraction efficiency at t = 0 ps, similar to the measurement performed on the 107 nm Ru sample. However, for the samples shown here, we measure periodic sinusoidal oscillations with a decreasing amplitude on top of a decreasing background. The diffraction efficiency induced by the acoustic waves is on the order of 10^{-9}.

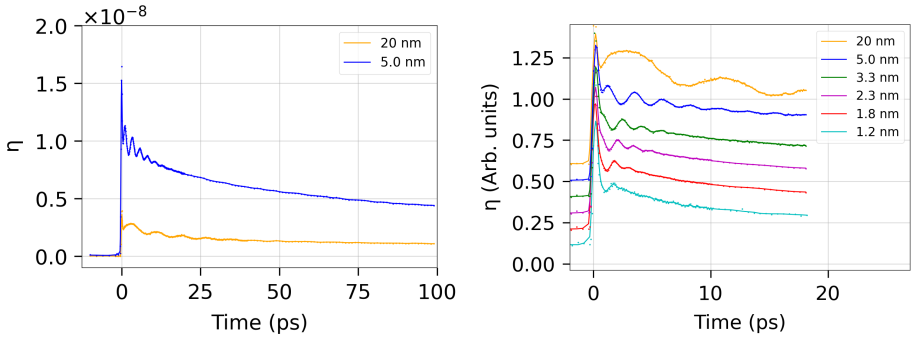

Figure 6.5: Transient-grating pump-induced changes to the diffraction efficiency. (a) The measured diffraction efficiency for 20 nm and 5 nm thick Ru layers on a long timescale. (b) The measured diffraction for multiple layer thicknesses, here the curves have been normalized to their respective electronic peaks and have been given an offset for clarity.

When the Ru layer thickness is on the same order as the electron energy diffusion depth the entire layer will heat up homogeneously. Using the two-temperature model, given by Eqs. (2.2) and (2.3), we can calculate that for Ru layers thinner than about 25 nm, the entire layer is homogeneously heated within 4 ps or less.

Thus, isotropic stress is formed in the layer, generating a standing acoustic wave, formed by the addition of two counter-propagating acoustic waves. Since the penetration depth of the probe light is approximately 8.5 nm, the probe will also diffract off the acoustic-wave-induced grating at the Ru/glass interface for the ultrathin layers discussed here. The light diffracted off the Ru/glass interface will accumulate an additional optical phase that is determined by the layer thickness and by the phase shift that occurs upon reflection/diffraction off the interface. The difference in optical phase between the beams diffracted off the Ru/glass interface and off the grating at the surface can cause interference between the two diffracted beams and should be considered in future attempts to simulate the measurements.

For the ultra-thin layers, as compared to the 107 nm Ru layer, we would initially expect a constant, thermally induced, background diffraction, since the lattice temperature is equal throughout the entire layer. However, a gradually decreasing background is present. This is attributed to the slow energy diffusion into the underlying glass substrate. We note that this is different for the 107 nm thick Ru layer where the relatively slow decay was determined by diffusion of thermal energy deeper into the Ru itself.

The optically generated standing wave results in periodic oscillations in diffraction efficiency after approximately 1 ps. The frequency of such a standing wave is determined by the layer thickness d and the speed of sound of the material v_c and is given by $f = v_c/2d$. If we use the known layer thicknesses and the speed of sound derived from the 107 nm Ru sample, we find that the expected oscillation frequencies are 603 GHz and 150 GHz for the 5 nm and 20 nm thick Ru layer, respectively. However, the measured frequencies of the acoustic oscillations are approximately 420 GHz and 130 GHz for the 5 nm and 20 nm thick layers, respectively.

To investigate the discrepancy between the expected and measured sound frequencies, we performed pump-probe measurements on multiple Ru layer thicknesses, from 1.2 to 20 nm, as shown in Fig. 6.5(b). Note the shorter timescale when compared to Fig. 6.5(a). All curves have been normalized to their respective electron diffraction peak at t $\approx$ 0 ps and have been given a vertical offset for clarity. The figure shows that we measure a general increase in the apparent frequency of the acoustic waves when the layer thickness decreases, as expected. The layer thicknesses have been determined by accurately calibrating the deposition rate of the sputter-coater using a profilometer to measure the thickness of a relatively thick layer of Ru. In addition, after deposition, the layer thicknesses have been experimentally confirmed for the 5.0 and 20 nm thick Ru layer samples using ellipsometry.

To better show only the *acoustic-wave* induced diffraction efficiency, we removed

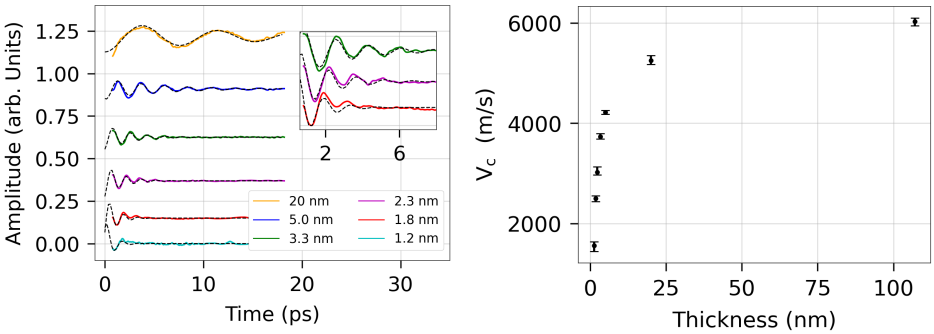

(a) (b)

Figure 6.6: (a) Measured diffraction efficiency of multiple layer thicknesses, also shown in Fig. 6.5(b) but with the thermal background removed. The dashed lines correspond to a fit of a single-frequency, damped sine to the data. (b) The speed of sound extracted from the fit as a function of layer thickness.

the thermal background by subtracting an exponentially decaying function with a single time constant from the data, see appendix A for more detail. The results are shown in Fig. 6.6(a). The black dashed line going through each data set represents a fit to the data with a single frequency, exponentially damped sine. In the inset of this figure, we show a zoomed-in version of the 1.8, 2.3, and 3.3 nm measurements. Close inspection of the data shows that the fit slightly deviates from the measured data. The frequency, or the phase, of the measured oscillating acoustic diffraction efficiency changes as a function of time. This was confirmed by repeating the experiment several times.

If we initially ignore this, as the effect seems to be fairly small, and assume a single-frequency acoustic signal, we can extract the frequency from the fit and, combined with the Ru layer thicknesses, we can calculate the effective speed of sound for all Ru layers. This is shown in Fig. 6.6(b). We find that the effective speed of sound strongly depends on the layer thickness, ranging from 1555 ± 80 m/s for a layer thickness of 1.2 nm to 6030 ± 70 m/s for a layer thickness of 107 nm. It has been shown that the sound velocity in thin metal films can decrease as a function of layer thickness due to the thin-film softening effect, which has been reported for thin films of Au [160, 161] and Ni [162]. It has also been shown that Young's modulus can decrease with decreasing layer thickness due to changes in crystal structure and grain size [163], which directly influences the speed of sound. Furthermore, although difficult to see in the AFM and SEM measurements, we suspect that the thinnest Ru layers, ≤ 1.8 nm, may not be continuous. This most

likely influences the effective speed of sound as well. We caution, however, that Ru can oxidize and form an oxide layer at the surface of ≈ 1 nm thickness. The consequences of these effects on the observed sound velocity and, thus, the sound frequency are difficult to predict.

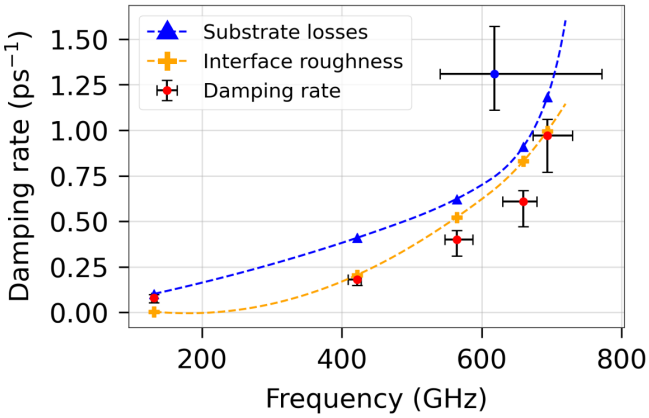

Figure 6.7: The red dots show the damping rate versus the frequency of the acoustic wave. The blue dot corresponds to the damping rate acquired for the 1.2 nm thick Ru layer. The yellow crosses represent the calculated damping rate caused by interface roughness and the dashed line going through the data points acts as a guide to the eye. The blue triangles represent the calculated damping rate caused by transmission of acoustic energy into the substrate, and again, the dashed line going through the data points acts as a guide to the eye. The blue data point has been excluded from all the above mentioned analysis due to its high uncertainty.

Another interesting observation is that we measure an increase of the acoustic damping rate for decreasing layer thicknesses, as can be seen in Fig. 6.7. The red dots show the measured damping rate versus the frequency of the acoustic waves. The blue dot represents the measured damping rate for the frequency corresponding to the 1.2 nm thick Ru layer. Accurate determination of the frequency of the acoustic wave is not possible for the 1.2 nm thick layer because there is only half a period of the oscillation present, as can be seen in Fig. 6.6(a). However, we do find the strongest damping rate for the frequency corresponding to the 1.2 nm thick layer. The error bars have been determined as the range of frequencies and damping rates for which a reasonable fit to the data, as shown in Fig. 6.6(a), could be obtained. For the analysis that follows, the blue data point has been excluded due to the relatively high uncertainty in the estimated frequency of the acoustic wave in the 1.2 nm thick layer.

An important mechanism for the observed signal decay in our setup is most likely that sound waves are partially transmitted every time they reach the Ru/glass interface. The transmission and reflection values are determined by the acoustic impedance mismatch between the Ru and the glass. If this mismatch were independent of the frequency, the decay rate would still increase for higher frequencies because at higher frequencies, there would be more reflections of the acoustic wave from the Ru/glass interface per unit of time. Another way of phrasing this is to say that the decay time expressed in units of the number of periods of the acoustic wave, would be constant. However, from our measurements we see that the decay is faster for higher frequencies, which may be an indication that the acoustic impedance of the Ru changes as well. This can be understood from the fact that the acoustic impedance of a material is given by $Z = \rho v_c$. Thus, from the measured (see Fig. 6.6(b)) frequency-dependent speed of sound, we can calculate the frequency-dependent acoustic impedance of the ruthenium. Combined with the acoustic impedance of the glass substrate, $Z_{sub} = 12.5 \times 10^6\,\mathrm{Ns/m^3}$ [28], we can calculate the acoustic reflection coefficient for the Ru/glass interface, using

$$R(f) = \left(\frac{Z_{Ru}(f) - Z_{sub}}{Z_{Ru}(f) + Z_{sub}} \right)^2, \tag{6.5}$$

where $Z_{Ru}(f)$ is the frequency-dependent acoustic impedance of ruthenium. The calculated acoustic impedance at the different measured frequencies can be found in Table 6.1.

Frequency (GHz)	131	421	564	659	693
$\mathbf{Z_{Ru}}$ **(10^6Ns/m^3)**	64.4	52.5	46.4	37.7	31.1

Table 6.1: Calculated acoustic impedance of Ru at the different measured acoustic frequencies.

From the acoustic reflection coefficient, we can derive the frequency-dependent decay rate of our measured diffraction signal caused by the loss of acoustic energy into the substrate, which is shown by the blue triangles and the blue dashed line in Fig. 6.7. We find that the shape of the damping rate caused by substrate losses matches the measured shape of the damping rate reasonably well, despite a quantitative difference in strength. However, we note that the acoustic impedance depends not only on the speed of sound but also on the density. So far, we have used the bulk value for the density of ruthenium in these calculations but, perhaps, the density is different for these thin layers. A more precise calculations would therefore require knowledge of the layer thickness-dependent density of the ruthenium, which we do not have access to. For the present calculation, a fixed

ruthenium density has been assumed of 12.45 g/cm^3 [159]. Qualitatively speaking, the agreement of the calculated frequency-dependent damping rate with the measured damping rate would improve if we could assume a higher ruthenium density than the bulk value.

Another mechanism which could contribute to damping of the signal is the surface roughness of the Ru layers. The surface roughness leads to a distribution of the effective thickness across the entire layer. Such a variation in the effective thickness could lead to the generation of a broader spectrum of generated sound frequencies that would give rise to a more strongly damped signal. Note that if the RMS values of the surface roughness are not strongly dependent on layer thickness, the ratio of the RMS roughness value and the layer thickness will determine the relative spread of generated frequencies. Thin layers would thus give rise to a more strongly decaying signal. By taking the height distribution of the ruthenium directly from AFM measurements for each layer thickness, we can calculate the width of frequency distribution of the acoustic wave. From this, we extract the damping rate as a function of the layer thickness, and thus the frequency. The result of this calculation is shown as the orange crosses and the orange dashed line in Fig. 6.7. We see that the calculated damping due to Ru/Air interface roughness is close to the measured damping rate. However, AFM images show that the glass substrate has a similar surface roughness as the Ru, meaning that the effective thickness could be homogeneous throughout the entire layer if the Ru follows the glass topography. Nevertheless, at this moment we cannot determine whether the topography of the Ru exactly copies that of the glass. This means that we cannot state with certainty that the surface roughness could explain the measured rapid damping of the acoustic wave for the thinnest layers.

We note that other decay mechanisms exist as well, such as viscous damping [59, 63] which can give a decay which quadratically depends on the frequency. However, our experimental results currently do not allow us to conclude whether interface roughness and/or viscous damping contribute to the measured frequency-dependent damping rate which appears to be dominated by partial transmission of the acoustic wave into the substrate.

6.3.3 Pump power dependence

In Fig. 6.8(a) and (b) we show time-resolved pump-probe diffraction measurements on the 5 nm Ru layer and on the 2.3 nm layer, respectively, as a function of the sum of the energies of the two pump pulses. Again, the thermal background has been removed by subtracting a decaying exponential function. The dashed line represents a fit to the data with a single frequency, damped sine. However, rather than fitting to the whole waveform as we have shown in Fig. 6.6(a), here we start

the fit at 2 ps and 1.8 ps for the 5 nm and 2.3 nm layers respectively, indicated by the vertical dashed red lines. The fitted function is then extrapolated back to t = 0 ps. From the fit, we extract acoustic frequencies of 420 ± 10 GHz and 750 ± 15 GHz for the 5.0 nm and 2.3 nm thick layers, respectively. We observe a mismatch between the measured data and the extrapolated sinusoidal fit in approximately the first 2 ps after excitation. This could be due to several reasons. One reason might be that the method used for the subtraction of the thermal background is not perfect. Subtraction of an exponential fit to correct for the slowly decaying lattice temperature during the time that the electron gas cools and still heats the lattice could lead to unreliable results in the first two ps.

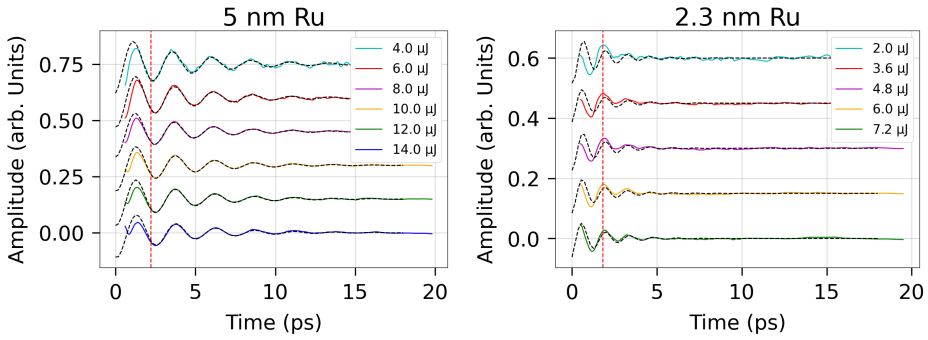

(a) (b)

Figure 6.8: Measured pump-power dependence of the diffraction for a 5 nm (a) Ru layer and a 2.3 nm (b) Ru layer. The black dashed lines are single frequency dampened sinusoidal fits to the data, starting from the dashed vertical red line and extrapolated backwards to t = 0.

Another reason might be that the frequency of the acoustic wave changes as a function of the lattice temperature. The latter hypothesis is supported somewhat by the fact that TTM calculations show that, under our experimental conditions, the lattice temperature rapidly increases and reaches high values, but stabilizes and remains constant after approximately 2 ps, see Appendix B for more details. However, as we will show later, the frequencies measured after 2 ps when the lattice temperature has stabilized, do *not* depend on the pulse energy and therefore the lattice temperature. This rules out a temperature dependent frequency. After 2 ps the fit matches the data almost perfectly, showing no changes in the frequency of the acoustic wave.

Note that, using the TTM, our calculations show that the lattice temperature in our samples somewhat exceeds the melting point of Ru for the highest pump powers, even when using temperature-dependent thermodynamic properties such as

the electron-phonon coupling constant and the lattice heat capacity [164]. However, our TTM calculations do not take into account the latent heat of melting, which has been shown to play a key role in high power optical experiments on Ru layers [165]. It has been shown that taking the latent heat of melting into account will keep the (lattice) temperature of the Ru at the melting temperature for a little longer, for pulse energies that are somewhat higher than needed to reach the melting point temperature [165].

In Fig. 6.9, we show the frequency and phase extracted from the fits, indicating that the frequency and phase, after 2 ps, remain nearly constant. What is surprising here is that for both thicknesses and all pump-powers, the measured starting phase obtained by extrapolating the fit back to t=0 approximately equals $-\pi/2$. This would seem to suggest that at t = 0 there is a non-zero acoustically induced diffraction efficiency. It has been shown that hot electron pressure can also contribute to the generation of stress [35]. Since the stress generated by the hot electron pressure occurs on a somewhat faster timescale than the stress generated by the lattice, the phase of the strain generated by the electron pressure induced stress will be different from the phase of the lattice-heating-induced strain, which changes the phase of the total strain [166].

$$\sigma_e = \gamma_e \Delta E_e, \tag{6.6}$$

where γ_e is the electronic Grüneisen parameter and ΔE_e is the change in electron gas energy. A similar relationship holds for the lattice temperature-induced stress, which scales linearly with the lattice Grüneisen parameter γ_l. The presence of a significant addition to the strain wave generation by electron pressure has been shown for ultrathin Ni layers [162], where $\gamma_e > \gamma_l$. For ruthenium, however, we have $\gamma_e \approx 0.8$ and $\gamma_l = 2.3$ [167], which means that $\gamma_e < \gamma_l$. Attempts to describe the non-zero starting phase by simulating the layer expansion using a driven harmonic oscillator model [166] where we include electron pressure (not shown here) indicates that its contribution is indeed small and, therefore does not change the phase of the acoustic wave significantly. As electron pressure appears to be an unlikely candidate to explain why the back extrapolated fit has a non-zero value at t = 0, we speculate that during the first 1.8-2.0 ps the phase/frequency of the acoustic wave changes.

6.4 Summary

In this paper, we have shown the ability to generate high-frequency laser-induced acoustic waves in thin Ru layers deposited on glass. We find that for a relatively

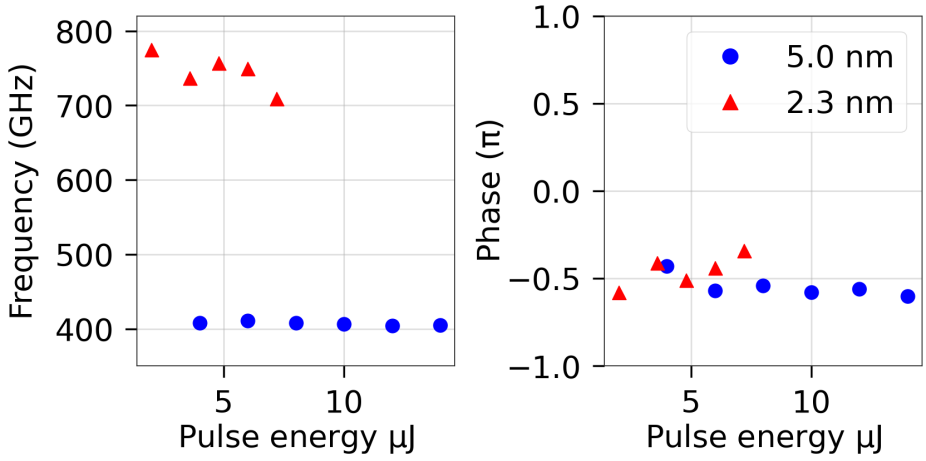

Figure 6.9: The starting phase and the frequency of the generated acoustic wave, extracted from the fits shown in Fig. 6.8(a) and (b). Note that for both thicknesses the frequency and phase remain almost constant as a function of pump pulse energy and that the phase equals -$\pi/2$ for all pump powers.

thick layer of 107 nm Ru, a traveling strain wave is created that perturbs the optical properties periodically and propagates with approximately the bulk speed of sound. Based on our simulations, we find that the acoustically induced optical response of the Ru layer is governed mostly by the thermo- and strain-optic effects. For ultra-thin Ru layers with thicknesses ranging from 1.2 to 20 nm deposited on glass, we demonstrate that we are able to generate extremely high-frequency acoustic waves with frequencies up to 750 GHz. We find that that the speed of sound for these thin layers strongly depends on the layer thickness and thus the frequency of the strain wave. We attribute the layer thickness-dependent speed of sound to possible thin-film softening effects and changes in grain size. Furthermore, this effective frequency-dependent speed of sound results in a frequency-dependent acoustic impedance mismatch between the Ru and the glass substrate, leading to a faster decay of the measured signals with increasing frequency. Moreover, the frequency of the acoustic waves appears to be constant after approximately 2 ps. By back-extrapolation of the signal, we observe an apparent initial phase of $-\pi/2$ for the acoustic-induced optical response. This would suggest that there is a non-zero acoustically induced diffraction efficiency at t = 0. Electron pressure could in principle explain this measured behavior. However, we have calculated that the strain wave generated by the electron pressure in Ru layers is not strong

enough to significantly change the phase of the acoustic wave. Therefore, as a non-zero starting phase seems unlikely, we speculate that the phase/frequency of the acoustic wave changes during the first 2 ps after optical excitation.

Appendix A: Thermal background removal

For the analysis of the measured acoustic signals from the ultrathin Ru layers, it is important that we separate the acoustic behavior from the slowly decaying thermal background signal. As mentioned in the main body, we attribute the slow thermal decay to lattice heat diffusion into the substrate.

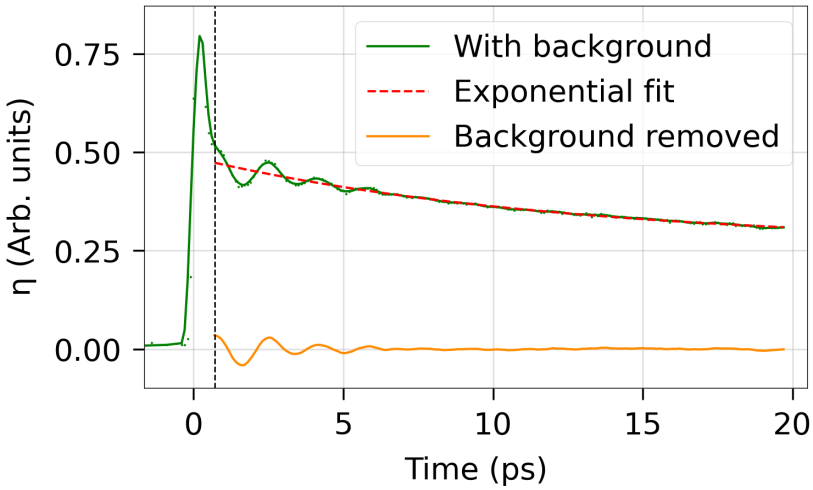

Figure 6.10: The different steps undertaken to remove the slowly decaying thermal background from the measured signal on the 3.3 nm thick Ru layer. In green, we show the nearest neighbor average of the normalized acoustic-wave-induced diffracted probe signal as a function of pump-probe delay. The red curve shows the exponential fit to the data truncated at the time t = 0.7 ps, indicated by the vertical dashed line. After subtraction of the exponential fit, we end up with the acoustic signal shown in yellow.

The different steps in the background removal procedure are shown in Fig. 6.10, where we show the background removal for the 3.3 nm thick Ru layer. First, we take the nearest neighbor average of the data with two neighbors. Visual inspection of the data reveals that there are two decay time scales. First, we observe a rapid decay in the first picosecond, caused by cooling of the electron gas. Afterward, we observe a slow exponential decay up until the end of our signal, attributed to heat diffusion into the substrate. We truncate the measured signal at t =

0.7 ps, indicated by the vertical black dashed line. Truncation of the measured signal is required to largely eliminate the part of the signal caused by the electron dynamics. We have experimented with several truncation times and found that the shortest truncation time where still good agreement between the fit to a single exponentially decaying function and the data is realized, equals t = 0.7 ps. Good agreement between the fit and the data is determined by looking at the overlap between the fit and the data at timescales where the acoustic oscillations have mostly decayed. The function used to fit the background is given by,

$$f(t) = ae^{b(t-c)} + d, \tag{6.7}$$

where a, b, c, and d are fitting parameters. The exponential fit is shown as the red-dashed line in Fig. 6.10. After this, the exponential background is subtracted from the data and we are left with the yellow curve, also shown in Fig. 6.10.

Appendix B: Two-Temperature calculations

We numerically solve the TTM, according to Eqs. (2.2) and (2.3), to obtain the time-dependent electron and lattice temperature distributions for the Ru layers. The material parameters used in the TTM are shown in Table 6.2 and the experimental conditions are the same as those described for the experimental results shown in Fig. 6.8.

Parameter	**Value**
A_e ($\mathrm{Jm^{-3}K^{-2}}$)	385
k_0 ($\mathrm{Wm^{-1}K^{-1}}$)	117
g ($10^{16}\mathrm{Wm^{-3}K^{-1}}$)	185
C_l ($10^{6}\mathrm{Jm^{-3}K^{-1}}$)	2.95

Table 6.2: ruthenium material parameters used in the TTM calculations, taken from Ref. [58].

In Fig. 6.11(a) and (b) we show the calculated electron and lattice temperature, respectively, as a function of time in the middle of the Ru layer. Due to the small layer thickness and the high thermal conductivity of the Ru, the layer is heated homogeneously. The source term used to simulate heat absorption by the laser in Eq. (2.2) is calculated using a so-called three-layer model. This model calculates the electric and magnetic field at all locations inside the sample as a function of time, and takes into account all optical interface reflections and their interference. Using the electric and magnetic field we can calculate the absorbed energy per

unit volume and per unit time using Poynting's Theorem [56]. Since we excite the sample using a transient-grating geometry, we only deposit energy into the sample in the bright fringes of the grating, whereas no energy is deposited into the dark fringes of the grating. To take this effect into account, the incident total laser energy is multiplied by a factor of two to get the deposited energy inside a bright fringe of the transient grating.

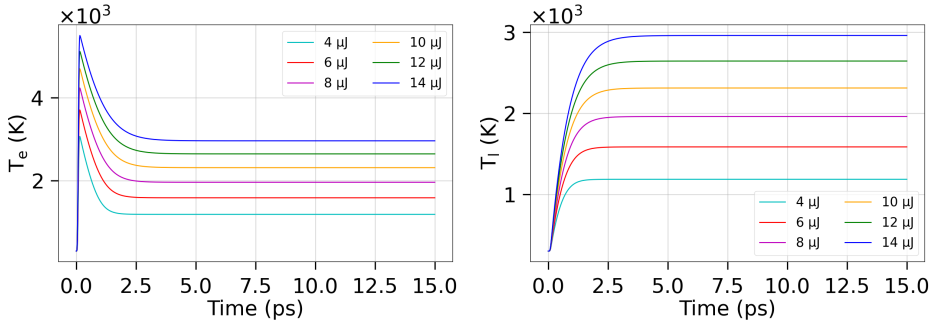

(a) (b)

Figure 6.11: Electron (a) and lattice (b) temperature as a function of time in the center of a 5 nm thick Ru layer in a bright fringe of the transient grating. The legend shows the total energy of the two incident pump beams which form the transient grating.

From the TTM calculations we see that immediately after excitation, the electron temperature starts to rise quickly, after which the electron temperature cools down to a constant value within 2 ps via energy transfer to the lattice. Due to the energy transfer from the electrons to the lattice, the lattice temperature starts to gradually increase. After 2 ps, the lattice temperature has also reached a constant value. It should be noted that for the two highest pump powers, the calculated lattice temperature exceeds the melting temperature of ruthenium, which equals 2583 K [159]. However, our samples did not show any sign of material damage, even after prolonged exposure to the laser pulses. Therefore, we tentatively conclude that the temperature of our Ru layer in the experiments did not exceeded the melting temperature. One explanation for this could be that our TTM calculations do not take the latent heat of melting into account. This will keep the Ru temperature fixed at the melting point temperature for a limited range of increasing pump energies [165]. In addition, there is some uncertainty in the measured excitation and material parameters and, thus, in the final temperatures reached. The TTM calculations for the 2.3 nm thick Ru layer show the same dynamics as those for the 5.0 nm thick Ru layer.

7 Femtosecond time-resolved pump-probe measurements on percolating gold in the ablation regime*

In this chapter we report on femtosecond laser ablation experiments on percolating gold layers deposited on a glass substrate. In order to launch acoustic waves with a higher amplitude, one could simply increase the excitation energy. However, at a certain fluence threshold, the sample will get damaged by the incident radiation. To attempt to circumvent this issue, it is important to understand the damage mechanism. In the experiments shown in this chapter, we measure changes in optical transmission and reflection induced by single, high-intensity infrared laser pulses as a function of the time delay between the pump and the probe. For the highest pump intensities, we find that on a time scale of about 150 ps after excitation, the transmission and reflection approach values that are close to the substrate transmission and reflection values. We attribute this to the vaporization of the entire layer when the injected energy exceeds the cohesive energy of the material. This vaporization results in the rapid transformation of the gold layer into a sufficiently dilute mist of atoms and nano-particles which renders the material almost optically transparent to the probe pulse. SEM images of the surfaces show how the morphology of the films changes at relatively low excitation intensities and show the complete removal of the gold at high intensities. We find that the ablation threshold for percolating Au on glass is 2.3 $\times$ 10^{11} W/cm^2, which is two orders of magnitude lower than the damage threshold for continuous gold layers reported in the literature.

*This chapter has been published in a slightly modified form as Opt. Express **28**(8), 12093-1210 (2020)

7.1 Introduction

Discontinuous, nanostructured metallic surfaces exhibit different linear and nonlinear optical properties compared to continuous metallic layers [168–170]. Examples of enhanced nonlinear optical effects range from the generation of terahertz pulses [116, 171, 172] to strongly enhanced second-harmonic generation [173, 174]. An example of a nanostructured surface that has been widely studied is percolating gold. Gold is a non-oxidizing metal and its physical and linear optical properties are generally well-understood [175, 176]. When physical vapor deposition is used to make gold layers on glass, a nanostructured surface forms, consisting of isolated islands that coalesce into larger networks with increasing average layer thickness. When deposition continues, an average layer thickness is reached where connected networks of gold provide an uninterrupted conducting path for electrons from one end of the sample to the other. The threshold where this occurs is called the percolation threshold and depends on the type of substrate [177, 178], but typically occurs around an average layer thickness of about 6 nm for gold on glass.

The linear and nonlinear optical properties of gold around the percolation threshold are reasonably well understood. However, little is known about the effects of percolation in the extreme nonlinear optical regime where laser pulse powers are high enough that damage and even ablation takes place. It is known, for example, that optical field strengths can be strongly enhanced in the gaps between the metal structures of a nanostructured metal surface such as percolating gold [179]. What is not known, is what the time-dependent response of such a surface is when the intensity reaches and exceeds the damage threshold.

Here, we show measurements of the transient optical response of a percolating gold surface after optical excitation with a strong 56 fs duration pump pulse, powerful enough to ablate material. In our experiments, a pump pulse excites the percolating gold and a time-delayed attenuated probe pulse measures the change in optical reflection and transmission induced by the excitation. Our results show that the measured pump-induced optical reflection change for a percolating gold surface initially shows a rapid, strong increase, followed by a slower decrease to negative values, with a rate that is fluence-dependent. For the highest pump fluences, the induced optical changes seem to saturate and are quasi-constant during the first two picoseconds. Transmission measurements show similar dynamics, with an initial sharp decrease in transmission, a quasi-constant plateau during the first two picoseconds, followed by a slower increase to positive values on longer time scales. For the highest intensities, the transmission and reflection of the samples approach the substrate values on a time scale of about 150 ps. We argue that this means that the percolating gold layer has become nearly optically transparent and suggests

that it has changed into a relatively dilute "mist" of atoms and/or nanoparticles on this time scale. We attribute this to the percolating nature of the film which gives rise to significantly more absorption compared to a continuous gold layer, and to the small average thickness of the layer which makes vaporization of the entire layer on this time scale plausible. We find that the ablation threshold for percolating Au is 2.3×10^{11} W/cm^2, which is two orders of magnitude lower than the damage threshold for continuous gold layers reported in the literature.

7.2 Experimental setup

A schematic drawing of the experimental setup is shown in Fig. 7.1. An amplified Ti:Sapphire laser (Coherent Astrella) with a repetition rate of 1 kHz, a central wavelength of 800 nm, a pulse length of 35 fs, and a maximum pulse energy of 6 mJ is used. The laser pulses are sent into an optical parametric amplifier (OPA, HE-TOPAS from Light Conversion). The OPA generates infrared laser pulses and is tuned to a wavelength of 1300 nm with a pulse energy of about 1 mJ. A wavelength of 1300 nm is used because at this wavelength the OPA has a high output power and because we want to reduce the probability of directly exciting interband transitions, which are known to occur at wavelengths shorter than about 502 nm in Au [52]. A non-collinear autocorrelator is used to measure the pulse length. Assuming a Gaussian temporal profile, a pulse duration of 56 ± 5 fs for both the pump and the probe pulses is measured. Both pump and probe pulses are s-polarized.

The output of the OPA is split into a stronger pump beam and a weaker probe beam using a 90/10 beam splitter. The pump beam passes through a mechanical chopper which is synchronized with the 1 kHz pulse train from the laser. With a 50% duty-cycle, the chopper reduces the repetition rate of the pump to 500 Hz, so that every other pump pulse is blocked. Afterward, the beam reflects off a rapidly rotating galvo mirror which, when in the "on" position, directs the pump pulse through the setup and when in the "off" position, directs the pump into a beam dump. The galvo mirror is phase-locked to the chopper allowing us to select individual pulses to enter the setup. Selected pump pulses are sent through two wire-grid polarizers to attenuate the pulse energy. Finally, using a 10 cm focal length lens, the pump pulse is focused onto the sample to a spot size with a diameter of approximately 100 µm. The sample is mounted on a computer-controlled xy-translation stage to translate the sample in the plane parallel to the sample surface. Each pump pulse either removes or damages the Au layer locally. To ensure that every pump pulse illuminates an undamaged part of the sample, the sample stage moves the sample 400 µm to a new position after each pump shot.

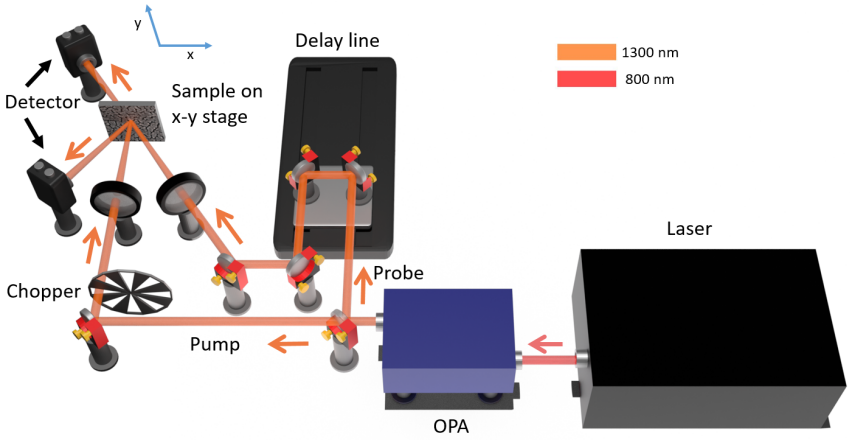

Figure 7.1: Schematic drawing of the setup. The laser beam coming out of the HE-TOPAS, with a central wavelength of 1300 nm, is split into pump and probe. After this, the repetition rate of the pump is halved using a mechanical chopper. Using a phase-locked rapidly rotating galvo mirror we select single pump pulses. The power of these pulses can be attenuated using two wire grid polarizers. After a pump pulse is incident on the sample a time-delayed probe pulse is measured in both reflection and transmission using two InGaAs detectors. Using an automated xy-translation stage we move the sample to a new position after every pump pulse.

A weak, 180 nJ probe pulse, time-delayed by first sending it to a variable optical delay line, is focused onto the same spot on the sample under a 15-degree angle with respect to the pump beam. The diameter of the probe focal spot is approximately 50 µm, twice as small as the pump beam diameter. The transmission and reflection of the probe pulse are then measured simultaneously using two InGaAs detectors. A third InGaAs detector is used to measure a reference beam that is split off from the probe. This reference is used to monitor fluctuations in the OPA output power. Since the repetition rate of the pump is half that of the probe, we measure the reflection/transmission of a probe pulse when the pump is blocked, and when the pump is transmitted, allowing us to measure the pump-induced transmission and reflection changes. After the reflection and transmission change are measured, the sample stage moves the sample to a new position. For each delay between pump and probe, this process is repeated 25 times to improve the signal-to-noise ratio of the measured probe transmission and reflection. Both the reflection and transmission changes are plotted normalized to the initial unperturbed reflection

R_0 and transmission T_0 when the pump is blocked, so $\Delta R/R_0$ and $\Delta T/T_0$. In what follows we will refer to $\Delta R/R_0$ as the reflection change and to $\Delta T/T_0$ as the transmission change.

The samples used in the experiments are prepared using physical vapor deposition at a pressure below 10^{-6} mbar. The substrates are chemically cleaned glass plates with a thickness of 2 mm. During the evaporation process, the deposited film thickness was monitored using a quartz crystal oscillator. Scanning Electron Microscope (SEM) images of all samples were made before and after the experiments were performed. An example image of an undamaged sample with an effective film thickness of 6 nm is shown in the inset of Fig. 7.1. All samples show a similarly nanostructured Au layer, typical for Au deposited on glass with an effective thickness at, or close to, the percolation threshold. We find the effective fraction of the surface covered in Au to be 0.85, which is somewhat above the reported percolation threshold of 0.68 [177]. All gold layers have an average thickness of 6 nm and SEM images show that all gold layers have a similar percolating morphology.

To determine whether laser-substrate interaction plays a role in our experiments, pump-probe measurements were also performed on the bare substrate for all pump energies. No transient effect was measured on a timescale of our experiments on a timescale of 0 to 1 ns, except for a small, pulse duration limited instantaneous effect at t=0. This we attribute to the coherent coupling between the pump and probe beam in the substrate. This coherent coupling gives rise to apparent changes in probe reflectivity and transmission, which were measured to be less than 1% for our highest used pump energy. Furthermore, optical microscopy images of the substrate after the experiment show no permanent alteration of the substrate.

7.3 Results

In this section, we will describe the measured results, both the time-dependent transmission and reflection changes, and the aftermath. In section 4 the results will be discussed in further detail and an interpretation of the results will be given.

7.3.1 Power dependence

In Fig. 7.2(a) and (b) we plot the time-dependent pump-induced reflection and transmission change during the first 15 ps after excitation of a percolating gold layer, for ten different values of the pulse energy, ranging from 1 µJ to100 µJ. These pulse energies correspond to a fluence range of 0.0127 J/cm^2 to 1.27 J/cm^2 and an intensity range of 2.3×10^{11} W/cm^2 to 2.3×10^{13} W/cm^2. We define the intensity here as the pulse energy divided by the pulse duration divided by beam surface area determined by the FWHM diameter of the beam on the sample.

For all pump energies, when pump and probe overlap in time at t=0, we observe a pulse length limited increase in the reflection change $\Delta R/R_0$ and a pulse length limited decrease in the transmission change $\Delta T/T_0$. Both become larger with increasing pump fluence. For pump energies of 35 µJ and less, we measure a small quasi-exponential decrease in reflection change in the first two picoseconds. For pulse energies of 1, 2, 5, and 10 µJ this is followed by a slow increase on a 15 ps time scale, whereas for the pulse energies of 20 and 35 µJ this is followed by a signal decrease. For pump pulse energies of 50 µJ and higher, the reflection changes reach values of approximately 50% and vary little during the first two picoseconds. After two picoseconds, the signals begin to decay and become negative. Very similar effects are seen for measurements of the transmission change, which are opposite in sign compared to the reflection change.

In Figs. 7.2(c) and 7.2(d) we plot the time-dependent pump-induced reflection and transmission changes of the percolating Au samples for time delays up to one nanosecond. We show that for pump energies of 10 µJ and lower the slow increase of the reflection change, seen in Fig. 7.2(a) after two picoseconds, continues for a few tens of picoseconds (inset of 7.2(c)). Afterward, a decrease to negative values occurs on a time scale of hundreds of picoseconds. Again, similar effects can be seen for the transmission measurements, but with opposite sign. For pulse energies of 20 µJ and higher, after staying relatively constant during the first two picoseconds, the reflection change drops, becomes negative, and reaches a value that corresponds to an absolute reflection of about 9% ($\Delta R/R = -75\%$), indicated by the black dashed line. This value of 9% corresponds to the absolute reflectivity measured on a bare substrate under the same experimental conditions. The rate of the decrease in the reflection change for these high fluences grows with increasing pulse energy.

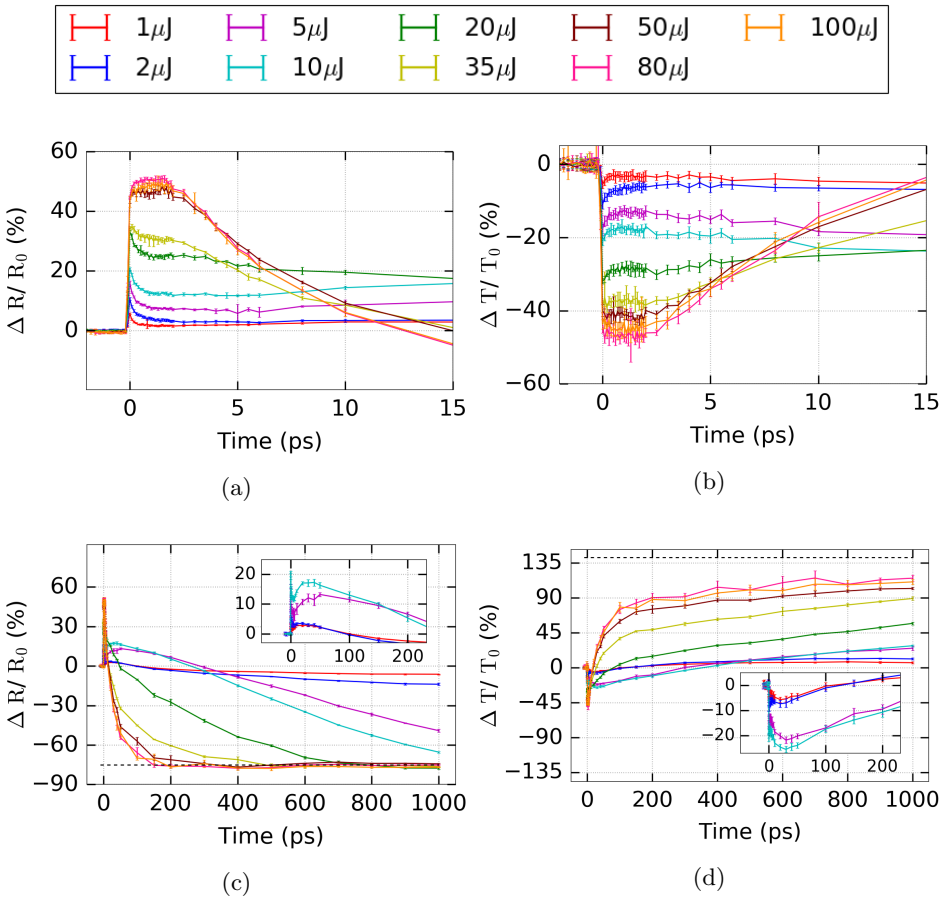

Figure 7.2: (a), (c) Pump-induced reflection change and, (b), (d) transmission change as a function of delay between the pump and probe pulses for pump pulse energies ranging from 1 to 100 µJ and on two different time scales. At t=0 ps the pump and probe overlap in time. Both the pump and the probe have a wavelength of 1.3 µm.

7.3.2 SEM analysis

So far, we have described the ultrafast pump-induced changes in the reflection and transmission of the percolating gold layers on a time scale of up to 1 ns. In this section, we will show SEM images taken of the samples before and after illumination for different pulse energies.

In Figs. 7.3(a) and (b) we show the SEM images for two different magnifications of the sample surface after illumination with a pump pulse with an energy of 1 µJ on two different length scales. In Fig. 7.3(c) we show the location of the SEM images on an optical microscopy image of the entire crater. Note that on the microscopy image the crater looks black, indicating no material present. However, closer inspection using the SEM shows that this is not the case. We notice that, in contrast with images made for higher pump energies, the gold in the center has not been fully removed but now shows larger holes whilst in between these holes the percolating Au structure is still in pristine condition. The structure of the center of the illuminated regime closely resembles that of the edge of the craters for higher pump energies, as becomes clear when comparing Fig. 7.3(b) with Fig. 7.4(b), where we show the crater edge for a pulse energy of 35 µJ. We note that in the case of illumination with a 1 µJ pulse, ablation only occurs locally. Therefore, we can determine the ablation threshold by calculating the intensity for a 1 µJ pump pulse. Thus, we find that the intensity at which removal of the gold starts taking place equals 2.3×10^{11} W/cm^2. The ablation threshold we measured is on the same order of magnitude as the ablation threshold measured for trapped single spherical gold nanoparticles [180].

In Figs. 7.4(a) and (b), we show typical SEM images of the sample surface both before and after illumination, respectively, with a pump pulse energy of 35 µJ. The image of the aftermath is taken at the left edge of the pump-induced crater, as indicated by the arrow in Fig. 7.4(c). For all pulse energies above 5 µJ used in the experiment similar images were obtained but not shown. In the experiment, the transverse beam profile of the pump resembles a Gaussian, with a beam diameter of approximately 100 µm. Due to the Gaussian-like shape of the pulse, a transverse pump intensity gradient is present on the Au surface. As a result, in Fig. 7.4(b) we observe a transition from little damage on the left side of the image to significant damage on the right side, which is closer to the center of the beam. In Fig. 7.4(b) the crater begins when moving further to the right. Furthermore, we note that the gold layer is curling up at the edges of the crater.

In Figs. 7.5(a) and (b) we show more detailed SEM images of the edge of the crater at two different magnifications for a sample illuminated with a pump energy of 100 µJ. Here it can be clearly seen that the gold at the edge has become detached

from the substrate and is curling up, indicating violent removal of material. Furthermore, next to the crater edge there is a small band where no gold is present, which is the location where the curled-over gold used to be. Due to the rapid heating of the lattice and vaporization, pressure will develop at the substrate-film interface and at the free surface. The curling over of the gold indicates that the pressure developed at the substrate film interface exceeds that of the pressure developed on the free surface, causing the gold to violently detach.

Further towards the center of the crater is a region where isolated nano-islands of gold are present with a diameter of approximately 50 nm. This region extends 20 µm towards the center of the crater. Optical microscopy and SEM analysis show that there is no more gold left in the crater center itself. Due to charging effects of the substrate during SEM, clear imaging of the center of the crater was not possible.

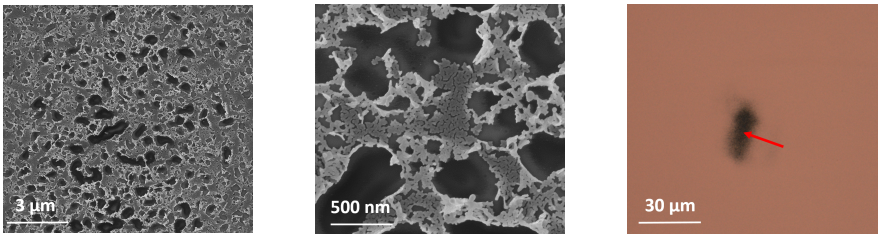

(a) (b) (c)

Figure 7.3: (a) SEM image of the sample illuminated with a 1 µJ pump pulse. (b) Zoomed-in image of the sample. At these pump intensities, the gold layer is damaged but has not been fully removed in the center. Note that large holes have appeared in the layer and that the edges of the holes curl over. In between the large holes the original percolating structure of the Au is still present, indicating that the intensity used here is close to the ablation threshold. (c) Optical microscopy image of the crater. The red arrow gives an indication of the location where the SEM images were taken.

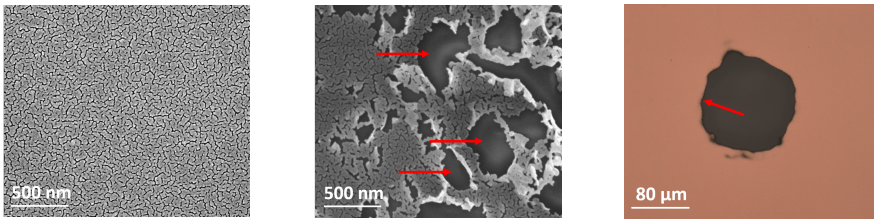

(a) (b) (c)

Figure 7.4: SEM images of the percolating Au surface, before (a) and after (b) illumination with a 35 µJ single laser pulse. In (b) we show the left edge of the pump-induced crater. We observe local removal of gold from the surface. The red arrows indicate regions where the gold has been removed and the substrate is visible. Furthermore, at the edge of the holes the gold is curling over indicating violent removal of the gold. (c) Optical microscopy image of the crater. The red arrow gives an indication of the location where the SEM image of (b) was taken.

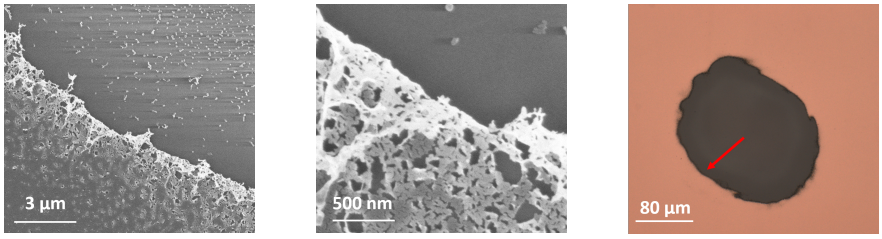

(a) (b) (c)

Figure 7.5: (a) SEM image of the crater edge. The sample was illuminated with a pulse energy of 100 µJ. The transition of the non-damaged percolating Au (bottom left) to a damaged region closer to the crater center (top right) can be seen. In the top right half of the figure many nano-islands of gold are visible. These isolated nano-islands of gold are present for the first 20 µm, starting from the crater edge towards the crater center, except in the region where the curled-over gold used to be. In between the nano-islands the bare substrate (darker grey) can clearly be seen. (b) Zoomed-in SEM image of the crater edge, Note the different length scales indicated in the figures. (c) Shows an optical microscopy image of the crater. The red arrow gives an indication of the location where the SEM images were taken.

7.4 Discussion

The interaction between ultrafast laser pulses and various materials has been investigated extensively in the past [52,148,150,181–184]. When a femtosecond laser pulse irradiates a metal, the energy is partly absorbed by the electrons, creating a non-thermal electron distribution [53, 185]. The electron gas then thermalizes into a Fermi-Dirac distribution on a timescale of several hundreds of femtoseconds [158, 186]. This so-called thermalization time has been shown to decrease with increasing laser power [186]. During and after thermalization, energy is exchanged with the lattice via electron-phonon coupling [50,75,187]. The timescale of electron energy transfer to the lattice is governed by the electron-phonon coupling constant g, which is unique for every metal [188].

This process of energy exchange between the electrons and the lattice can be described by the two-temperature model (TTM), as first proposed by Anisimov et. al. [49]. This model consists of two coupled differential equations describing the temporal and spatial evolution of both the electron temperature T_e and the lattice temperature T_l. Both the electron gas and the lattice have their own heat capacities, C_e and C_l, respectively. The heat capacities themselves can also exhibit a temperature dependency at high temperatures. In general, the electron heat capacity is much smaller than the lattice heat capacity, allowing the electrons to heat up to relatively high temperatures, even for low fluences.

It has been shown that the process of energy transfer to the lattice occurs on a timescale of 1-10 ps for Au [51, 189, 190]. An estimate of the theoretical lattice temperature attained in our experiment can be made by taking the pump pulse energy absorbed in a disk of percolating gold with an effective thickness of 6 nm and a diameter equal to the diameter of the pump beam. It has been shown that for thin gold layers with a thickness of ≈ 50 nm the heat capacity is not different with respect to the bulk lattice heat capacity [191]. However, the heat capacity for a 6 nm thick percolating layer might be different, but the exact value is not known to us. Therefore, as a *rough* approximation, in our calculations we use the lattice heat capacity of a 50 nm thick gold layer at room temperature, having a value of 2.44×10^6 $\mathrm{Jm^{-3}K^{-1}}$. Furthermore, assuming an incident pulse energy of 100 µJ, a *measured* absorptivity of 0.32 and a beam diameter of about 100 µm, we calculate a lattice temperature of 2.78×10^5 K. This temperature of course well exceeds the melting and boiling temperature for Au (1338 K and 3243 K respectively) and is therefore not the real temperature reached. It does indicate, however, that extreme conditions are reached in our experiments. One of the reasons for this is the structure of the percolating surface. The percolating Au absorptance (A_p) is higher for 1300 nm light than the absorptance of a flat continuous Au layer

(A_c). We found in our experiments that $A_p \approx 16A_c$. It is known that percolating gold absorbs considerably more light than continuous layers of gold and therefore heats up more. The increased absorption is typically attributed to the excitation of localized plasmons in the nano-structured material [192, 193]. In turn, this can lead to local field enhancements which can lower the average damage threshold for percolating gold compared to that for continuous layers of gold.

In what follows we will provide a qualitative explanation for the reflection and transmission changes observed on different timescales.

7.4.1 Electron excitation

For both the reflection and transmission change, as seen in Fig. 7.2(a) and (b) respectively, we measure a pulse length limited increase in reflection and a decrease in transmission around t=0 ps, corresponding to an increase in absorption. Due to the strong excitation by the pump pulse the electron distribution, as described by a Fermi-Dirac distribution, starts to smear out. This smearing of the electron distributions results in a reduction of the electronic occupancy below the Fermi energy as sketched by the dashed area in Fig. 7.6. In this figure we show the electronic density of states (DOS) of the d-band together with the electron distribution of the hybridized s/p-band as a mere schematic representation of the new pump-induced allowed interband transitions with energy $E(\omega)$. It has been shown that such a reduction of electronic occupancy below the Fermi energy can lead to an increase in absorption [148], as lower energy photons can now induce optical transitions from the shallow d-band to the hybridized s/p-band [194, 195]. Thus it may become feasible for our probe photons with a relatively low energy $E(\omega)$ (Fig. 7.6) to excite previously forbidden *interband* transitions, consequently increasing the absorption. In general, we also induce *intraband* transitions, which have been shown to increase the reflectivity in Au as well [196].

In Fig. 7.7(a) and (b) we plot the reflection and transmission change at t=0 ps versus pump pulse energy. We see that the magnitude of the reflection and transmission change saturates for higher pump energies. For the reflection and transmission change, saturation occurs for pulse energies on the order of 50 µJ at a value of ∼50% for the reflection change and at a value ∼-45% for the transmission change.

We note that the reflection and transmission change start to saturate for high pump energies. We speculate that this is because the *changes* in electronic occupancy start to saturate due to the saturation of the broadening of the Fermi distribution which begins to flatten out at high pump energies. For high electron temperatures, the change in the smeared-out electron distribution becomes

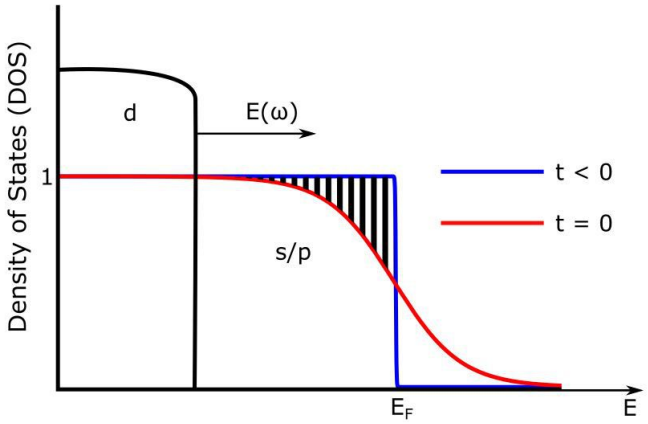

Figure 7.6: Schematic depiction of the broadening of the electronic occupation distribution and the consequently induced availability of intraband transitions from the d-band. Here we show the DOS of the d-band together with the Fermi distribution of the electrons of the hybridized s/p-band as a schematic representation of the possibility to excite electrons from the d- to the s/p-band. See [194] for a more accurate depiction of the actual DOS of the d-band of Au. In blue we show the unperturbed electron distribution, in red we show the electron distribution as changed by the pump pulse. The probe photon energy $E(\omega)$ is represented by the black arrow. Due to the broadening of the electron distribution, optical interband transitions for probe photons with an energy of $E(\omega)$ become possible.

less significant for further temperature increases and thus, changes in the optical response saturate as well. Saturation of the reflectivity change as a function of incident pump energy has been shown before for continuous gold [150] but, to our knowledge, not for percolating gold and never simultaneously in transmission and reflection and not for the intensities used in our experiments, which are at least two orders of magnitude above the damage threshold. Note, however, that the physics is likely to be complicated by the high probability that at these intensities, energetic electrons are capable of promoting electrons from the d-band to the s/p-band, thus increasing the number of carriers in the s/p-band.

7.4.2 Lattice relaxation

For pump pulse energies below 50 µJ, we observe a quasi-exponential decrease in the reflection change and an increase in the transmission change in the first 2 ps

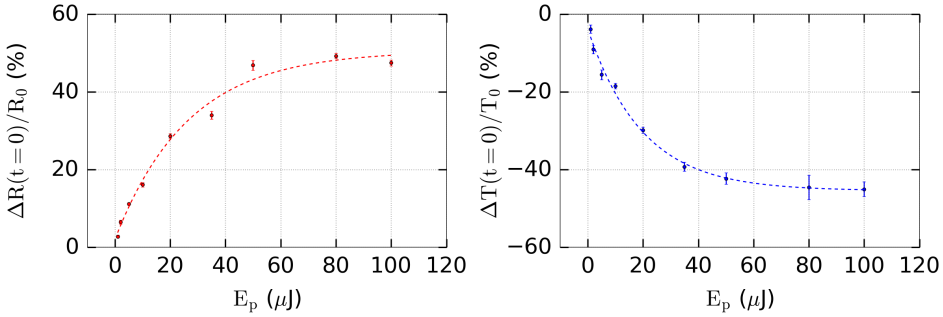

Figure 7.7: Pump-induced reflection change (a) and transmission change (b) at t=0 ps as a function of the pump pulse energy. The dashed line is an exponential fit and should be considered a guide to the eye.

after excitation.

When the metal layer is thin, the electron gas inside the layer homogeneously heats up. Under these circumstances, electron energy diffusion can be neglected and it was shown that this causes the electron gas temperature to decay linearly with time [52, 185]. However, the observed exponential decay seems to indicate that this does not play a role here. It has also been suggested that for noble metals a non-thermalized electron gas experiences a stronger electron-phonon coupling than a thermalized electron gas [185]. This implies that when the electron gas thermalizes and the coupling with the lattice decreases, the energy transfer rate to the lattice slows down. However, as mentioned at the beginning of section 4, we expect the thermalization time to increase with laser power and to be significantly shorter than 2 ps [197].

Instead, we think that the temperature-dependent electron-phonon coupling strength is responsible for the observed quasi-exponential decay. At lower power, it has been shown that in Au the electron gas will cool by heating the lattice on a timescale of 10-15ps [77]. However, for high electron temperatures, the electron-phonon coupling constant exhibits a temperature dependence [198]. At electron temperatures of about 2000 K and higher the electron-phonon coupling constant g increases and becomes proportional to T_e and T_l, i.e. $g \propto T_e + T_l$. It was shown that g can increase by as much as a factor of 6 when reaching electron temperatures on the order of 2×10^4K [194, 199], which is very likely in our experiments.

Assuming a linear relationship between the electron heat capacity and the electron temperature, i.e. $C_e(T_e) \propto T_e$ [200], which is normally only valid for electron

temperatures below 2000 K, we can calculate as a rough estimate that the electron temperature reached under our experimental conditions for the highest used pump energy of 100 µJ equals $\approx 1.5 \times 10^5$ K. This is, of course, a gross overestimate of the actual electron temperature due to the non-linear behavior of the electronic heat capacity at high temperatures. However, it gives an upper limit on the electron temperature and shows that under our experimental conditions, we can no longer assume that the electron-phonon coupling constant g is independent of the electron temperature. An increase of g will in turn increase the initial rate at which energy is transferred from the electron gas to the lattice, explaining the observation of an initial fast signal decay in our experiment.

We speculate that after 2 ps the electrons have cooled off substantially, lowering the electron-phonon coupling constant and decreasing the energy exchange rate, slowing down the cooling of the electron gas. Simultaneously, the lattice is heating up, increasing the reflection and decreasing the transmission at a timescale of approximately 30 ps, as can be seen in the insets of Figs. 7.2(c) and (d). These two competing effects of the electron-cooling and lattice-heating can explain the shape of the curves of the optical response on a timescale of 0.5 - 30 ps.

For pump pulse energies of 50 µJ and higher, we measure a constant plateau in both the reflection- and transmission change in the first 2 ps. When the electron gas transfers its energy to the lattice the electron distribution will relax to its original shape. However, since the change of the electron distribution is "saturated" it takes time for this relaxation to affect the optical parameters, thus creating a plateau. Simultaneously the lattice will heat up to extreme temperatures resulting in the rapid heating, melting, and, possibly, vaporization of the lattice. We speculate that at pulse energies above 10 µJ the morphological changes to the lattice occur before non-destructive changes in the lattice temperature have had the time to affect the reflection and the transmission. Therefore, the "bulge" in reflection and transmission as seen for pulse energies below 10 µJ in the insets of Figs. 7.2(c) and (d) is absent for pulse energies above 10 µJ. This rapid heating, melting and, possibly, vaporization of the Au results in a steep decrease in reflection and an increase in transmission.

7.4.3 Vaporization

On longer timescales, we see that the transmission values start to increase dramatically whilst the reflection values start to decrease and are even approaching the substrate values. This combined behavior of both reflection and transmission is strong evidence that the Au layer is becoming optically transparent on a remarkably short timescale of about 150 ps. This suggests that the excited layer has in fact vaporized into a mist of atoms and small particles, distributed over a

larger volume in a direction predominantly perpendicular to the surface. It has been shown that this process of vaporization is possible via dissociation of the entire layer when the injected energy exceeds the cohesive energy of the material [201, 202]. Using the pump pulse energy and beam size we can calculate the absorbed energy per gold atom. For 100 µJ pulse energy we calculate that the absorbed energy equals 59 eV/atom, whilst the cohesive energy of gold equals 3.81 eV/atom [200]. For all pulse energies above 5 µJ the absorbed energy per atom exceeds the cohesive energy of gold. For lower pulse energies the average absorbed energy per atom is lower than the cohesive energy. However, near-field optical hotspots due to the percolating nature of our film can lead to enhanced absorbed energy which locally exceeds the cohesive energy. Therefore, locally the threshold for removal of material is reached whereas it is not reached at other locations, explaining the morphology seen for the lowest fluences, see Fig. 7.3(b). It is important to realize that this process of vaporization is not the traditional vaporization process characterized by the Hertz-Knudsen equation which only describes vaporization from the outer surface. Hertz-Knudsen surface vaporization happens on timescales larger than 1 ns and is thus too slow to explain our experimental data [203].

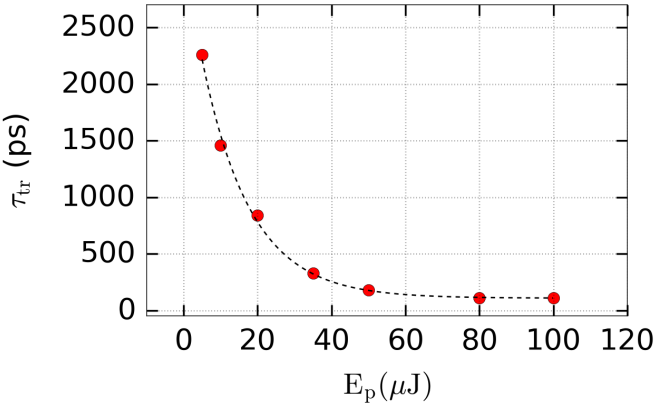

Figure 7.8: Time τ_{tr} before sample becomes transparent as a function of pump pulse energy. The dashed line is a decaying exponential and should be considered a guide to the eye.

The maximum reflection change possible in our system is when the absolute reflection equals the substrate reflection, which corresponds to a reflection change of ≈ -75%. When the reflection change reaches this value, the density of the mist of atoms/particles has decreased in such a manner that it has become nearly fully optically transparent for our probe pulse. We use only the reflection here because, although the transmission dramatically increases for the highest intensi-

ties, it has not yet fully reached the value of the bare substrate level. We suspect that this is caused by thermal lensing effects present in the substrate, which could diffract/refract some light away from the detector. However, more research is needed to confirm this hypothesis.

From our reflection measurements, we can derive the time τ_{tr} it takes for the Au gold to become optically transparent. The experimental data starting from Fig. 7.2(c) was fitted to an exponential function starting at 50 ps decaying to an asymptote of -75%, which corresponds to an absolute reflection close to that of the substrate. The time τ_{tr} is somewhat arbitrarily chosen as the time it takes for the reflection change to drop below -70%. For the pulse energies below 20 µJ extrapolation of the fit was necessary to retrieve τ_{tr}. For pulse energies below 10 µJ, the τ_{tr} was not extracted as the uncertainty in the extrapolated values for was too large for these slowly changing curves.

In Fig. 7.8 we show τ_{tr} as a function of the pulse energy. The dashed line is an exponential fit to the data which acts as a guide to the eye. We can see that for pulse energies larger than about 50 µJ, the sample reaches the substrate reflection levels, indicating that the percolating gold layer has transformed into a mist of atoms and/or small particles and has become optically transparent within approximately 150 ps.

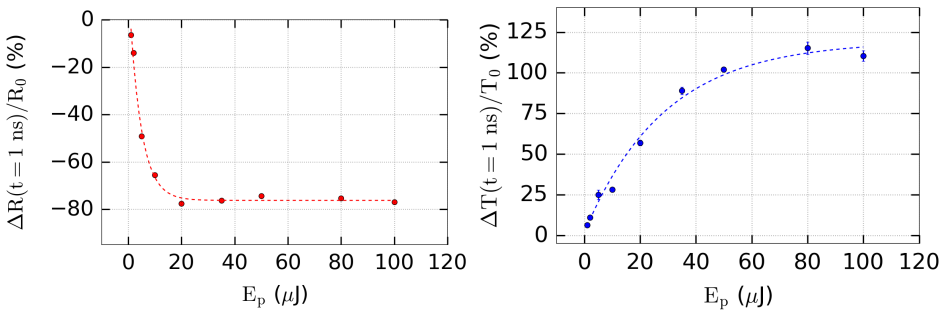

Figure 7.9: Pump-induced reflection change (a) and transmission change (b) at t=1 ns as a function of the pump pulse energy. The dashed line is an exponential fit and should be considered a guide to the eye.

In Fig. 7.9(a) and (b) we show the reflection and transmission change respectively as a function of pulse energy at t = 1 ns. Note how the reflection has reached the substrate value at this point for all pulse energies of 20 µJ and higher. We see that for the pulses with 10 and 20 µJ the substrate level has not yet been reached, indicating that the mist of atoms/particles is still partially opaque. The

transmission change shows similar saturation-like dynamics, but possibly due to the thermal lensing effect discussed previously, it has not completely saturated.

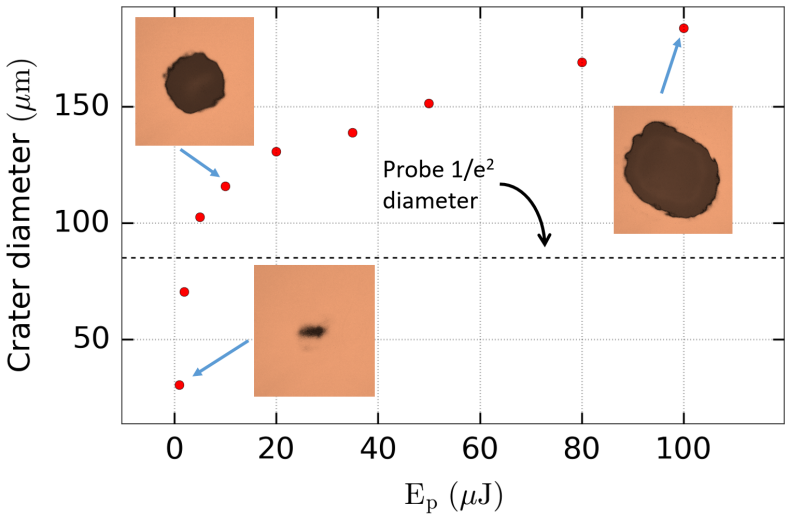

Figure 7.10: Crater diameter versus the pump pulse energy. The black dashed line represents the $1/e^2$ diameter of the probe. The three insets are optical microscopy images of the final crater.

In Fig. 7.10 we show the final diameter of the crater versus the incident pulse energy. The crater diameter was determined by measuring the surface area of the ablated crater and calculating an effective diameter corresponding to a circle with the same surface area. Note that for the pulse energies of 1 and 2 µJ, the resulting crater diameter is smaller than the $1/e^2$ size of the probe. This explains why we do not see the reflection and transmission values approach the substrate value, as can be seen in Fig. 7.9(a) and (b). For these pulse energies, a part of the probe beam still illuminates gold which has not been ablated. Due to this, the observed response in the measurements is not solely caused by ablation dynamics. Rather, it is a combination of measurements of the ablation effects in the part of the probe beam overlapping with, what will later become the crater and of non-destructive excitation in the part of the probe beam that does not overlap with the crater area.

7.5 Summary

We have shown transient pump-probe reflection and transmission measurements on percolating gold layers on glass substrates in the ablation regime. Our measure-

ments show a strong increase in reflection and a decrease in transmission directly after optical excitation. This is attributed to the increasing electron temperature and the subsequent Fermi-smearing of the electron distribution, resulting in a reduction of the electronic occupancy. Fermi smearing of the electron distribution enables excitations from the d-band to the hybridized s/p-band, increasing the absorption.

On longer times scales and for the highest intensities, both the reflection and transmission approach the values of the substrate on a timescale of about 150 ps, indicating that the Au layer becomes optically transparent. We argue that the vaporization of the entire layer into a mist of atoms and small particles is the most plausible explanation for this behavior. This process of vaporization is possible because the absorbed energy exceeds the cohesive energy of the gold atoms. We find that the ablation threshold of percolating gold layers is some two orders of magnitude lower than the values found for continuous layers of gold in the literature.

Bibliography

[1] "Apple unleashes M1," *https://www.apple.com/au/newsroom/2020/11/apple-unleashes-m1/*.

[2] "ASML," *https://www.asml.com/en*.

[3] G. E. Moore, "Cramming More Components onto Integrated Circuits," *IEEE Solid-State Circuits Soc. Newsl.*, vol. 11, pp. 33–35, 2006.

[4] G. E. Moore, "Electronics, Progress in digital integrated," *IEEE Solid-State Circuits Soc. Newsl.*, vol. 11, pp. 36–37, 2006.

[5] H. J. Levinson, *Principles of lithography: Third edition*. 2011.

[6] A. J. Den Boef, "Optical wafer metrology sensors for process-robust CD and overlay control in semiconductor device manufacturing," *Surf. Topogr. Metrol. Prop.*, vol. 4, no. 2, p. 23001, 2016.

[7] "Moore's Law: Transistors per microprocessor," *https://ourworldindata.org/grapher/transistors-per-microprocessor*.

[8] C. Mack, *Fundamental Principles of Optical Lithography: The Science of Microfabrication*. No. Ic, 2007.

[9] P. Van Zant, "Microchip Fabrication," *McGraw Hill Prof.*, vol. 155, no. 1, p. 611, 2004.

[10] M. Dusa, B. Arnold, J. Finders, H. Meiling, K. van Ingen Schenau, and A. C. Chen, "The lithography technology for the 32 nm HP and beyond," *Photomask Next-Generation Lithogr. Mask Technol. XV*, vol. 7028, 2008.

[11] E. Hecht, *Optics*. Pearson Education, 2017.

[12] C. Wagner and N. Harned, "EUV lithography: Lithography gets extreme," *Nat. Photonics*, vol. 4, no. 1, pp. 24–26, 2010.

[13] B. W. Smith, H. Kang, A. Bourov, F. Cropanese, and Y. Fan, "Water immersion optical lithography for 45-nm node," *Opt. Microlithogr. XVI*, vol. 5040, no. June, p. 679, 2003.

[14] K. Ronse, "Optical lithography-a historical perspective," *Comptes Rendus Phys.*, vol. 7, no. 8, pp. 844–857, 2006.

[15] H. Tanaka, A. Matsumoto, K. Akinaga, A. Takahashi, and T. Okada, "Comparative study on emission characteristics of extreme ultraviolet radiation from CO 2 and Nd:YAG laser-produced tin plasmas," *Appl. Phys. Lett.*, vol. 87, no. 4, pp. 1–4, 2005.

[16] P. Hayden, A. Cummings, N. Murphy, G. O'Sullivan, P. Sheridan, J. White, and P. Dunne, "13.5 Nm Extreme Ultraviolet Emission From Tin Based Laser Produced Plasma Sources," *J. Appl. Phys.*, vol. 99, no. 9, 2006.

[17] J. White, P. Dunne, P. Hayden, F. O'Reilly, and G. O'Sullivan, "Optimizing 13.5 nm laser-produced tin plasma emission as a function of laser wavelength," *Appl. Phys. Lett.*, vol. 90, no. 18, pp. 2005–2008, 2007.

[18] F. Torretti, R. Schupp, D. Kurilovich, A. Bayerle, J. Scheers, W. Ubachs, R. Hoekstra, and O. O. Versolato, "Short-wavelength out-of-band EUV emission from Sn laser-produced plasma," *J. Phys. B At. Mol. Opt. Phys.*, vol. 51, no. 4, 2018.

[19] V. Y. Banine, K. N. Koshelev, and G. H. Swinkels, "Physical processes in EUV sources for microlithography," *J. Phys. D. Appl. Phys.*, vol. 44, no. 25, 2011.

[20] J. Mulkens, M. Hanna, H. Wei, V. Vaenkatesan, H. Megens, and D. Slotboom, "Overlay and edge placement control strategies for the 7nm node using EUV and ArF lithography," *Extrem. Ultrav. Lithogr. VI*, vol. 9422, p. 94221Q, 2015.

[21] H. Wakabayashi, T. Ezaki, T. Yamamoto, M. Hane, and T. Mogami, "SUB-10-NM planar-bulk CMOS device characteristics using lateral junction control," *IEEE Int. Electron Devices Meet.*, 2003.

[22] M. M. Waldrop, "More than moore," *Nat. News*, vol. 530, no. 7589, pp. 144–147, 2016.

[23] G. Bouwhuis and S. Wittekoek, "Automatic alignment system for optical projection printing," *IEEE Trans. Electron Devices*, vol. 26, no. 4, pp. 723–728, 1979.

[24] J. W. Goodman, *Introduction to Fourier Optics.* McGraw-Hill, 2 ed., 1996.

[25] S. Keij, I. Setija, G. van der Zouw, and E. Ebert, "Advances in phase-grating-based wafer alignment systems," *Metrol. Insp. Process Control Microlithogr. XIX*, vol. 5752, p. 948, 2005.

[26] S. Edward, *Detection of hidden gratings using light and sound.* PhD thesis, University of Amsterdam, 2019.

[27] V. Verrina, *Laser-Induced Ultrasound for the Detection of Buried Micro- and Nano-Structures.* PhD thesis, University of Amsterdam, 2021.

[28] S. Edward, H. Zhang, I. Setija, V. Verrina, A. Antoncecchi, S. Witte, and P. C. M. Planken, "Detection of Hidden Gratings through Multilayer Nanostructures Using Light and Sound," *Phys. Rev. Appl.*, vol. 14, no. 1, p. 014015, 2020.

[29] S. Edward, H. Zhang, S. Witte, and P. C. M. Planken, "Laser-induced ultrasonics for detection of low-amplitude grating through metal layers with finite roughness," *Opt. Express*, vol. 28, no. 16, p. 23374, 2020.

[30] V. Verrina, S. Edward, H. Zhang, S. Witte, and P. C. M. Planken, "Photoacoustic detection of low duty cycle gratings through optically opaque layers," *Appl. Phys. Lett.*, vol. 117, no. 5, 2020.

[31] T. Saito, O. Matsuda, and O. B. Wright, "Picosecond acoustic phonon pulse generation in nickel and chromium," *Phys. Rev. B*, vol. 67, no. 20, pp. 1–7, 2003.

[32] J. L. Arlein, S. E. Palaich, B. C. Daly, P. Subramonium, and G. A. Antonelli, "Optical pump-probe measurements of sound velocity and thermal conductivity of hydrogenated amorphous carbon films," *J. Appl. Phys.*, vol. 104, no. 3, pp. 1–7, 2008.

[33] G. Tas and H. J. Maris, "Electron diffusion in metals studied by picosecond ultrasonics," *Phys. Rev. B*, vol. 49, no. 21, pp. 15046–15054, 1994.

[34] V. E. Gusev and O. B. Wright, "Ultrafast nonequilibrium dynamics of electrons in metals," *Phys. Rev. B*, vol. 57, no. 5, pp. 2878–2888, 1998.

[35] V. E. Gusev, "On the duration of acoustic pulses excited by subpicosecond laser action on metals," *Opt. Commun.*, vol. 94, pp. 76–78, 1992.

[36] J. Wang and C. Guo, "Effect of electron heating on femtosecond laser-induced coherent acoustic phonons in noble metals," *Phys. Rev. B*, vol. 75, no. 18, pp. 2–6, 2007.

[37] O. B. Wright and K. Kawashima, "Coherent phonon detection from ultrafast

surface vibrations," *Phys. Rev. Lett.*, vol. 69, no. 11, pp. 1668–1671, 1992.

[38] A. Devos and C. Lerouge, "Evidence of laser-wavelength effect in picosecond ultrasonics: Possible connection with interband transitions," *Phys. Rev. Lett.*, vol. 86, no. 12, pp. 2669–2672, 2001.

[39] A. Devos, R. Cote, G. Caruyer, and A. Lefvre, "A different way of performing picosecond ultrasonic measurements in thin transparent films based on laser-wavelength effects," *Appl. Phys. Lett.*, vol. 86, no. 21, pp. 1–3, 2005.

[40] D. Schneider, T. Witke, T. Schwarz, B. Schoneich, and B. Schultrich, "Testing ultra-thin films by laser-acoustics," *Surf. Coatings Technol.*, vol. 126, pp. 136–141, 2000.

[41] H. T. Grahn, H. J. Maris, and J. Tauc, "Time-resolved study of vibrations of a-Ge:H/a-Si:H multilayers," *Phys. Rev. B*, vol. 38, no. 9, 1988.

[42] B. Perrin, B. Bonello, J. C. Jeannet, and E. Romatet, "Picosecond ultrasonics study of metallic multilayers," *Phys. B Condens. Matter*, vol. 219-220, no. 1-4, pp. 681–683, 1996.

[43] A. Devos and A. Le Louarn, "Strong effect of interband transitions in the picosecond ultrasonics response of metallic thin films," *Phys. Rev. B*, vol. 68, no. 4, pp. 1–6, 2003.

[44] A. Devos and R. Cote, "Strong oscillations detected by picosecond ultrasonics in silicon: Evidence for an electronic-structure effect," *Phys. Rev. B*, vol. 70, no. 12, pp. 1–6, 2004.

[45] R. I. Tobey, E. H. Gershgoren, M. E. Siemens, M. M. Murnane, H. C. Kapteyn, T. Feurer, and K. A. Nelson, "Nanoscale photothermal and photoacoustic transients probed with extreme ultraviolet radiation," *Appl. Phys. Lett.*, vol. 85, no. 4, pp. 564–566, 2004.

[46] R. I. Tobey, M. E. Siemens, M. M. Murnane, H. C. Kapteyn, D. H. Torchinsky, and K. A. Nelson, "Transient grating measurement of surface acoustic waves in thin metal films with extreme ultraviolet radiation," *Appl. Phys. Lett.*, vol. 89, no. 9, 2006.

[47] G. A. Antonelli, P. Zannitto, and H. J. Maris, "New method for the generation of surface acoustic waves of high frequency," *Phys. B Condens. Matter*, vol. 316-317, pp. 377–379, 2002.

[48] T. Saito, O. Matsuda, M. Tomoda, and O. B. Wright, "Imaging gigahertz surface acoustic waves through the photoelastic effect," *J. Opt. Soc. Am. B*, vol. 27, no. 12, p. 2632, 2010.

[49] S. I. Anisimov, B. L. Kapeliovich, and T. L. Perel'man, "Electron emission from metal surfaces exposed to ultrashort laser pulses," *J. Exp. Theor. Phys.*, vol. 39, pp. 375–377, 1974.

[50] L. Jiang and H.-L. Tsai, "Improved Two-Temperature Model and Its Application in Ultrashort Laser Heating of Metal Films," *J. Heat Transfer*, vol. 127, no. 10, p. 1167, 2005.

[51] X. Y. Wang, D. M. Riffe, Y.-S. Lee, and M. C. Downer, "Time-resolved electron-temperature measurement in a highly excited gold target using femtosecond thermionic emission," *Phys. Rev. B*, vol. 50, no. 11, pp. 8016–8019, 1994.

[52] J. Hohlfeld, S.-S. Wellershoff, J. Güdde, U. Conrad, V. Jähnke, and E. Matthias, "Electron and lattice dynamics following optical excitation of metals," *Chem. Phys.*, vol. 251, no. 1-3, pp. 237–258, 2000.

[53] R. H. M. Groeneveld, R. Sprik, and A. Lagendijk, "Femtosecond spectroscopy of electron-electron and electron-phonon energy relaxation in Ag aund Au," *Phys. Rev. B*, vol. 51, no. 17, p. 11433, 1995.

[54] M. Bonn, D. N. Denzler, S. Funk, M. Wolf, S. S. Wellershoff, and J. Hohlfeld, "Ultrafast electron dynamics at metal surfaces: Competition between electron-phonon coupling and hot-electron transport," *Phys. Rev. B*, vol. 61, no. 2, pp. 1101–1105, 2000.

[55] D. J. Griffiths, *Introduction to Electrodynamics*. Prentice Hall, Inc., 3 ed., 1999.

[56] J. H. Poynting, "On the transfer of energy in the electromagnetic field," *Philos. Trans. R. Soc. London*, vol. 175, pp. 343–361, 1884.

[57] P. B. Johnson and R. W. Christy, "Optical Constant of the Nobel Metals," *Phys. Rev. B*, vol. 6, no. 12, pp. 4370–4379, 1972.

[58] J. P. Colombier, F. Garrelie, N. Faure, S. Reynaud, M. Bounhalli, E. Audouard, R. Stoian, and F. Pigeon, "Effects of electron-phonon coupling and electron diffusion on ripples growth on ultrafast-laser-irradiated metals," *J. Appl. Phys.*, vol. 111, no. 2, p. 024902, 2012.

[59] H. Zhang, A. Antoncecchi, S. Edward, I. Setija, P. Planken, and S. Witte, "Unravelling phononic, opto-acoustic and mechanical properties of metals with light-driven hypersound," *Phys. Rev. Appl.*, vol. 10, no. 1, pp. 1–12, 2020.

[60] C. Thomsen, H. T. Grahn, H. J. Maris, and J. Tauc, "Surface generation

and detection of phonons by picosecond light pulses," *Phys. Rev. B*, vol. 34, no. 6, pp. 4129–4138, 1986.

[61] B. Bonello, A. Ajinou, V. Richard, P. Djemia, and S. M. Chérif, "Surface acoustic waves in the GHz range generated by periodically patterned metallic stripes illuminated by an ultrashort laser pulse," *J. Acoust. Soc. Am.*, vol. 110, no. 4, pp. 1943–1949, 2001.

[62] J. L. Rose, *Ultrasonic guided waves in solid media.* Cambridge University press, 2014.

[63] H. Zhang, A. Antoncecchi, S. Edward, P. Planken, and S. Witte, "Ultrafast laser-induced guided elastic waves in a freestanding aluminum membrane," *Phys. Rev. B*, vol. 103, no. 6, pp. 1–10, 2021.

[64] Z.-h. Shen, S.-y. Zhang, and J.-c. Cheng, "Theoretical Study on Surface Acoustic Wave Generated by a Laser Pulse in Solids," *Anal. Chem.*, vol. 17, pp. 204–207, 2001.

[65] A. Aharoni, K. Jassby, and M. Tur, "The thermoelastic surface strip source for laser-generated ultrasound," vol. 92, no. 12, pp. 3249–3258, 2017.

[66] D. H. Hurley, R. Lewis, O. B. Wright, and O. Matsuda, "Coherent control of gigahertz surface acoustic and bulk phonons using ultrafast optical pulses," *Appl. Phys. Lett.*, vol. 93, no. 11, pp. 2006–2009, 2008.

[67] S. A. Maier, *Plasmonics: Fundamentals and Applications.* Springer, 1 ed., 2007.

[68] A. Otto, "Excitation of nonradiative surface plasma waves in silver by the method of frustrated total reflection," *Zeitschrift für Phys.*, vol. 216, no. 4, pp. 398–410, 1968.

[69] E. Kretschmann and H. Raether, "Radiative Decay of Non Radiative Surface Plasmons Excited by Light," *Zeitschrift fur Naturforsch. - Sect. A J. Phys. Sci.*, vol. 23, no. 12, pp. 2135–2136, 1968.

[70] E. Kretschmann, "Die Bestimmung optischer Konstanten von Metallen durch Anregung von Oberflächenplasmaschwingungen," *Zeitschrift für Phys.*, vol. 241, no. 4, pp. 313–324, 1971.

[71] R. H. Ritchie, E. T. Arakawa, J. J. Cowan, and R. N. Hamm, "Surface-plasmon resonance effect in grating diffraction," *Phys. Rev. Lett.*, vol. 21, no. 22, pp. 1530–1533, 1968.

[72] N. Rotenberg, M. Betz, and H. M. van Driel, "Ultrafast control of grating-

assisted light coupling to surface plasmons," *Opt. Lett.*, vol. 33, no. 18, p. 2137, 2008.

[73] A. Brodeur and S. L. Chin, "Ultrafast white-light continuum generation and self-focusing in transparant condensed media," *J. Opt. Soc. Am. B*, vol. 16, no. 4, 1999.

[74] G. Cerullo and S. De Silvestri, "Ultrafast optical parametric amplifiers," *Rev. Sci. Instrum.*, vol. 74, no. 1 I, pp. 1–18, 2003.

[75] J. Hohlfeld, J. G. Müller, S. S. Wellershoff, and E. Matthias, "Time-resolved thermoreflectivity of thin gold films and its dependence on film thickness," *Appl. Phys. B*, vol. 64, no. 3, pp. 387–390, 1997.

[76] H. J. Sielcken and H. J. Bakker, "Probing the ultrafast electron and lattice dynamics of gold using femtosecond mid-infrared pulses," *Phys. Rev. B*, vol. 102, no. 13, pp. 1–8, 2020.

[77] S. Edward, A. Antoncecchi, H. Zhang, H. Sielcken, S. Witte, and P. C. M. Planken, "Detection of periodic structures through opaque metal layers by optical measurements of ultrafast electron dynamics," *Opt. Express*, vol. 26, no. 18, pp. 23380–23396, 2018.

[78] H. J. Eichler, P. Günter, and D. W. Pohl, *Laser-Induced Dynamic Gratings*, vol. 50 of *Springer Series in Optical Sciences*. Berlin, Heidelberg: Springer Berlin Heidelberg, 1986.

[79] J. I. Goldstein, D. E. Newbury, P. Echlin, D. C. Joy, C. E. Lyman, E. Lifshin, L. Sawyer, and J. R. Michael, *Scanning electron microscopy and X-ray microanalysis*. Kluwer Academic/Plenum Publishers, 3 ed., 1978.

[80] T. E. Everhart and R. F. Thornley, "Wide-band detector for microampere low-energy electron currents," *J. Sci. Instrum.*, vol. 37, no. 7, pp. 246–248, 1960.

[81] G. Binnig, C. Quate, and C. Gerber, "Atomic Force Microscope," *Phys. Rev. Lett.*, vol. 56, no. 9, 1986.

[82] S. Adachi, *Optical properties of crystalline and amorphous semiconductors: Materials and fundamental principles*. Springer Science & Business Media, 1999.

[83] G. E. Jellison and F. A. Modine, "Parameterization of the optical functions of amorphous materials in the interband region," *Appl. Phys. Lett.*, vol. 69, no. 3, pp. 371–373, 1996.

[84] O. Matsuda, M. C. Larciprete, R. Li Voti, and O. B. Wright, "Fundamentals of picosecond laser ultrasonics," *Ultrasonics*, vol. 56, pp. 3–20, 2015.

[85] P. Ruello and V. E. Gusev, "Physical mechanisms of coherent acoustic phonons generation by ultrafast laser action," *Ultrasonics*, vol. 56, pp. 21–35, 2015.

[86] P. van Capel, *Ultrafast nonlinear acoustics in crystals and nanostructures*. University of Utrecht, 2008.

[87] M. V. Exter and A. Lagendijk, "Ultrashort Surface-Plasmon and Phonon Dynamics," *Phys. Rev. Lett.*, vol. 60, no. l, pp. 49–52, 1988.

[88] O. B. Wright and V. E. Gusev, "Acoustic generation in crystalline silicon with femtosecond optical pulses," *Appl. Phys. Lett.*, vol. 66, no. 10, pp. 1190–1192, 1995.

[89] M. R. Armstrong, E. J. Reed, K. Y. Kim, J. H. Glownia, W. M. Howard, E. L. Piner, and J. C. Roberts, "Observation of terahertz radiation coherently generated by acoustic waves," *Nat. Phys.*, vol. 5, no. 4, pp. 285–288, 2009.

[90] S. Edward, H. Zhang, I. Setija, V. Verrina, A. Antoncecchi, S. Witte, and P. C. M. Planken, "Detection of hidden gratings through multilayer nanostructures using light and sound," *Phys. Rev. Appl.*, vol. 10, no. 1, p. 1, 2019.

[91] T. F. Crimmins, A. A. Maznev, and K. A. Nelson, "Transient grating measurements of picosecond acoustic pulses in metal films," *Appl. Phys. Lett.*, vol. 74, no. 9, pp. 1344–1346, 1999.

[92] R. W. Wood, "On a remarkable case of uneven distribution of light in a diffraction grating spectrum," *London, Edinburgh, Dublin Philos. Mag. J. Sci.*, vol. 4, no. 21, pp. 396–402, 1902.

[93] H. P. Chen, Y. C. Wen, Y. H. Chen, C. H. Tsai, K. L. Lee, P. K. Wei, J. K. Sheu, and C. K. Sun, "Femtosecond laser-ultrasonic investigation of plasmonic fields on the metal/gallium nitride interface," *Appl. Phys. Lett.*, vol. 97, no. 20, pp. 1–4, 2010.

[94] R. Nuster, G. Paltauf, and P. Burgholzer, "Comparison of surface plasmon resonance devices for acoustic wave detection in liquid," *Opt. Express*, vol. 15, no. 10, pp. 6087–6095, 2007.

[95] K. Katayama, T. Sawada, and Q. Shen, "Detection of photoinduced electronic, thermal, and acoustic dynamics of gold film using a transient reflecting grating method under three types of surface plasmon resonance conditions," *Phys. Rev. B*, vol. 58, no. 13, pp. 8428–8436, 1998.

[96] J. Wang, J. Wu, and C. Guo, "Resolving dynamics of acoustic phonons by surface plasmons," *Opt. Lett.*, vol. 32, no. 6, p. 719, 2007.

[97] N. Rotenberg, J. N. Caspers, and H. M. Van Driel, "Tunable ultrafast control of plasmonic coupling to gold films," *Phys. Rev. B*, vol. 80, no. 24, pp. 1–8, 2009.

[98] H. Raether, "Surface Plasmons on Smooth and Rough Surfaces and on Gratings," *Springer tracts Mod. Phys.*, vol. 111, pp. 1–3, 1988.

[99] L. E. Kreilkamp, I. A. Akimov, V. I. Belotelov, B. A. Glavin, L. V. Litvin, A. Rudzinski, M. Kahl, R. Jede, M. Wiater, T. Wojtowicz, G. Karczewski, D. R. Yakovlev, and M. Bayer, "Terahertz dynamics of lattice vibrations in Au/CdTe plasmonic crystals: Photoinduced segregation of Te and enhancement of optical response," *Phys. Rev. B*, vol. 93, no. 12, pp. 1–10, 2016.

[100] N. Khokhlov, G. Knyazev, B. Glavin, Y. Shtykov, O. Romanov, and V. Belotelov, "Interaction of surface plasmon polaritons and acoustic waves inside an acoustic cavity," *Opt. Lett.*, vol. 42, no. 18, p. 3558, 2017.

[101] V. V. Temnov, "Ultrafast acousto-magneto-plasmonics," *Nat. Photonics*, vol. 6, no. 11, pp. 728–736, 2012.

[102] V. V. Temnov, C. Klieber, K. A. Nelson, T. Thomay, V. Knittel, A. Leitenstorfer, D. Makarov, M. Albrecht, and R. Bratschitsch, "Femtosecond nonlinear ultrasonics in gold probed with ultrashort surface plasmons," *Nat. Commun.*, vol. 4, pp. 3–8, 2013.

[103] J. H. Hodak, I. Martini, and G. V. Hartland, "Observation of acoustic quantum beats in nanometer sized Au particles," *J. Chem. Phys.*, vol. 108, no. 22, pp. 9210–9213, 1998.

[104] J. H. Hodak, A. Henglein, and G. V. Hartland, "Size dependent properties of Au particles: Coherent excitation and dephasing of acoustic vibrational modes," *J. Chem. Phys.*, vol. 111, no. 18, pp. 8613–8621, 1999.

[105] G. V. Hartland, "Coherent vibrational motion in metal particles: Determination of the vibrational amplitude and excitation mechanism," *J. Chem. Phys.*, vol. 116, no. 18, pp. 8048–8055, 2002.

[106] G. V. Hartland, "Coherent Excitation of Vibrational Modes in Metallic Nanoparticles," *Annu. Rev. Phys. Chem.*, vol. 57, no. 1, pp. 403–430, 2006.

[107] Z. Chen and M. F. Decamp, "Measuring optical phonon dynamics in a bismuth thin film through a surface plasmon resonance," *J. Appl. Phys.*, vol. 112, no. 1, 2012.

[108] D. H. Hurley and K. L. Telschow, "Picosecond surface acoustic waves using a suboptical wavelength absorption grating," *Phys. Rev. B*, vol. 66, no. 15, pp. 1–4, 2002.

[109] Q. Li, K. Hoogeboom-Pot, D. Nardi, M. M. Murnane, H. C. Kapteyn, M. E. Siemens, E. H. Anderson, O. Hellwig, E. Dobisz, B. Gurney, R. Yang, and K. A. Nelson, "Generation and control of ultrashort-wavelength two-dimensional surface acoustic waves at nanoscale interfaces," *Phys. Rev. B*, vol. 85, no. 19, pp. 1–8, 2012.

[110] H. N. Lin, H. J. Maris, L. B. Freund, K. Y. Lee, H. Luhn, and D. P. Kern, "Study of vibrational modes of gold nanostructures by picosecond ultrasonics," *J. Appl. Phys.*, vol. 73, no. 1, pp. 37–45, 1993.

[111] M. Colletta, W. Gachuhi, S. A. Gartenstein, M. M. James, E. A. Szwed, B. C. Daly, W. Cui, and G. A. Antonelli, "Picosecond ultrasonic study of surface acoustic waves on periodically patterned layered nanostructures," *Ultrasonics*, vol. 87, pp. 126–132, 2018.

[112] Z. H. Shen, B. Q. Xu, X. W. Ni, J. Lu, and S. Y. Zhang, "Theoretical study on line source laser-induced surface acoustic waves in two-layer structure in ablative regime," *Opt. Laser Technol.*, vol. 36, no. 2, pp. 139–143, 2004.

[113] A. M. Aindow, R. J. Dewhurst, and S. B. Palmer, "Laser-generation of directional surface acoustic wave pulses in metals," *Opt. Commun.*, vol. 42, no. 2, pp. 116–120, 1982.

[114] A. Harata, H. Nishimura, and T. Sawada, "Laser-induced surface acoustic waves and photothermal surface gratings generated by crossing two pulsed laser beams," *Appl. Phys. Lett.*, vol. 57, no. 2, pp. 132–134, 1990.

[115] R. D. Lide, "CRC Handbook of Chemistry and Physics," *J. Am. Chem. Soc.*, vol. 126, no. 5, p. 1586, 2004.

[116] G. K. Ramanandan, G. Ramakrishnan, N. Kumar, A. J. Adam, and P. C. M. Planken, "Emission of terahertz pulses from nanostructured metal surfaces," *J. Phys. D. Appl. Phys.*, vol. 47, no. 37, p. 374003, 2014.

[117] A. Derkachova, K. Kolwas, and I. Demchenko, "Dielectric Function for Gold in Plasmonics Applications: Size Dependence of Plasmon Resonance Frequencies and Damping Rates for Nanospheres," *Plasmonics*, vol. 11, no. 3, pp. 941–951, 2016.

[118] Y. C. Chang, P. Zhou, and J. H. Burge, "Analysis of phase sensitivity for binary computer-generated holograms," *Appl. Opt.*, vol. 45, no. 18, pp. 4223–

4234, 2006.

[119] X. Wei, A. J. Wachters, and H. P. Urbach, "Finite-element model for three-dimensional optical scattering problems," *J. Opt. Soc. Am. A*, vol. 24, no. 3, p. 866, 2007.

[120] M. Besbes, J. P. Hugonin, P. Lalanne, S. van Haver, O. T. Janssen, A. M. Nugrowati, M. Xu, S. F. Pereira, H. P. Urbach, A. S. van de Nes, P. Bienstman, G. Granet, A. Moreau, S. Helfert, M. Sukharev, T. Seideman, F. I. Baida, B. Guizal, and D. Van Labeke, "Numerical analysis of a slit-groove diffraction problem," *J. Eur. Opt. Soc.*, vol. 2, no. Mm, 2007.

[121] A. Haim, S. Bar-Ad, and A. Azoulay, "Elastic characterization of Au thin films utilizing laser induced acoustic Rayleigh waves," *J. Phys. Conf. Ser.*, vol. 278, no. 1, 2011.

[122] R. M. Slayton, K. A. Nelson, and A. A. Maznev, "Transient grating measurements of film thickness in multilayer metal films," *J. Appl. Phys.*, vol. 90, no. 9, pp. 4392–4402, 2001.

[123] V. Verrina, S. Edward, H. Zhang, A. Antoncecchi, S. Witte, and P. C. M. Planken, "Role of scattering by surface roughness in the photoacoustic detection of hidden micro-structures," *Appl. Opt.*, vol. 59, no. 30, 2020.

[124] A. Antoncecchi, H. Zhang, S. Edward, V. Verrina, P. C. M. Planken, and S. Witte, "High-resolution microscopy through optically opaque media using ultrafast photoacoustics," *Opt. Express*, vol. 28, no. 23, p. 33937, 2020.

[125] B. C. Daly, N. C. Holme, T. Buma, C. Branciard, T. B. Norris, D. M. Tennant, J. A. Taylor, J. E. Bower, and S. Pau, "Imaging nanostructures with coherent phonon pulses," *Appl. Phys. Lett.*, vol. 84, no. 25, pp. 5180–5182, 2004.

[126] G. de Haan, V. Verrina, A. J. L. Adam, H. Zhang, and P. C. M. Planken, "Plasmonic enhancement of photoacoustic-induced reflection changes," *Appl. Opt.*, vol. 60, no. 24, pp. 7304–7313, 2021.

[127] G. de Haan, T. J. van den Hooven, and P. C. M. Planken, "Ultrafast laser-induced strain waves in thin ruthenium layers," *Opt. Express*, vol. Submitted, 2021.

[128] M. Rumi and J. W. Perry, "Two-photon absorption: an overview of measurements and principles," *Adv. Opt. Photonics*, vol. 2, no. 4, p. 451, 2010.

[129] P. D. Khang, M. Davoudiniya, L. T. T. Phuong, T. C. Phong, and M. Yarmohammadi, "Optical interband transitions in strained phosphorene," *Phys.*

Chem. Chem. Phys., vol. 21, no. 27, pp. 15133–15141, 2019.

[130] M. Ghorbani-Asl, S. Borini, A. Kuc, and T. Heine, "Strain-dependent modulation of conductivity in single-layer transition-metal dichalcogenides," *Phys. Rev. B - Condens. Matter Mater. Phys.*, vol. 87, no. 23, pp. 1–6, 2013.

[131] W. S. Yun, S. W. Han, S. C. Hong, I. G. Kim, and J. D. Lee, "Thickness and strain effects on electronic structures of transition metal dichalcogenides: 2H-MX 2 semiconductors (M = Mo, W; X = S, Se, Te)," *Phys. Rev. B - Condens. Matter Mater. Phys.*, vol. 85, no. 3, pp. 1–5, 2012.

[132] P. Lu, X. Wu, W. Guo, and X. C. Zeng, "Strain-dependent electronic and magnetic properties of MoS 2 monolayer, bilayer, nanoribbons and nanotubes," *Phys. Chem. Chem. Phys.*, vol. 14, no. 37, pp. 13035–13040, 2012.

[133] H. Peelaers and C. G. Van De Walle, "Effects of strain on band structure and effective masses in MoS2," *Phys. Rev. B - Condens. Matter Mater. Phys.*, vol. 86, no. 24, pp. 1–5, 2012.

[134] E. Scalise, M. Houssa, G. Pourtois, V. Afanas'ev, and A. Stesmans, "Strain-induced semiconductor to metal transition in the two-dimensional honeycomb structure of MoS2," *Nano Res.*, vol. 5, no. 1, pp. 43–48, 2012.

[135] S. Bhattacharyya and A. K. Singh, "Semiconductor-metal transition in semiconducting bilayer sheets of transition-metal dichalcogenides," *Phys. Rev. B - Condens. Matter Mater. Phys.*, vol. 86, no. 7, pp. 1–7, 2012.

[136] A. Kumar and P. K. Ahluwalia, "Semiconductor to metal transition in bilayer transition metals dichalcogenides MX2 (M = Mo, W; X = S, Se, Te)," *Model. Simul. Mater. Sci. Eng.*, vol. 21, no. 6, 2013.

[137] A. P. Nayak, S. Bhattacharyya, J. Zhu, J. Liu, X. Wu, T. Pandey, C. Jin, A. K. Singh, D. Akinwande, and J. F. Lin, "Pressure-induced semiconducting to metallic transition in multilayered molybdenum disulphide," *Nat. Commun.*, vol. 5, no. May, pp. 1–9, 2014.

[138] A. Visibile, R. B. Wang, A. Vertova, S. Rondinini, A. Minguzzi, E. Ahlberg, and M. Busch, "Influence of Strain on the Band Gap of Cu2O," *Chem. Mater.*, vol. 31, no. 13, pp. 4787–4792, 2019.

[139] X. Dou, K. Ding, D. Jiang, and B. Sun, "Tuning and identification of interband transitions in monolayer and bilayer molybdenum disulfide using hydrostatic pressure," *ACS Nano*, vol. 8, no. 7, pp. 7458–7464, 2014.

[140] A. Ramasubramaniam, D. Naveh, and E. Towe, "Tunable band gaps in bilayer transition-metal dichalcogenides," *Phys. Rev. B - Condens. Matter*

Mater. Phys., vol. 84, no. 20, pp. 1–10, 2011.

[141] K. He, C. Poole, K. F. Mak, and J. Shan, "Experimental demonstration of continuous electronic structure tuning via strain in atomically thin MoS2," *Nano Lett.*, vol. 13, no. 6, pp. 2931–2936, 2013.

[142] H. J. Conley, B. Wang, J. I. Ziegler, R. F. Haglund, S. T. Pantelides, and K. I. Bolotin, "Bandgap engineering of strained monolayer and bilayer MoS2," *Nano Lett.*, vol. 13, no. 8, pp. 3626–3630, 2013.

[143] C. R. Zhu, G. Wang, B. L. Liu, X. Marie, X. F. Qiao, X. Zhang, X. X. Wu, H. Fan, P. H. Tan, T. Amand, and B. Urbaszek, "Strain tuning of optical emission energy and polarization in monolayer and bilayer MoS2," *Phys. Rev. B - Condens. Matter Mater. Phys.*, vol. 88, no. 12, pp. 1–5, 2013.

[144] K. Guilloy, N. Pauc, A. Gassenq, Y. M. Niquet, J. M. Escalante, I. Duchemin, S. Tardif, G. Osvaldo Dias, D. Rouchon, J. Widiez, J. M. Hartmann, R. Geiger, T. Zabel, H. Sigg, J. Faist, A. Chelnokov, V. Reboud, and V. Calvo, "Germanium under High Tensile Stress: Nonlinear Dependence of Direct Band Gap vs Strain," *ACS Photonics*, vol. 3, no. 10, pp. 1907–1911, 2016.

[145] N. Egede Christensen and B. O. Seraphin, "Relativistic band calculation and the optical properties of gold," *Phys. Rev. B*, vol. 4, no. 10, pp. 3321–3344, 1971.

[146] P. Szczepanek and R. Glosser, "Piezo-optical constants of gold," *Solid State Commun.*, vol. 15, pp. 1425–1429, 1974.

[147] K. C. Rustagi, "Bilinear optical polarizability of silver," *Nuovo Cim. B Ser. 10*, vol. 53, no. 2, pp. 346–362, 1968.

[148] J. Hohlfeld, D. Grosenick, U. Conrad, and E. Matthias, "Femtosecond time-resolved reflection second-harmonic generation on polycrystalline copper," *Appl. Phys. A*, vol. 60, no. 2, pp. 137–142, 1995.

[149] S. S. Jha and C. S. Warke, "Interband contributions to optical harmonic generation at a metal surface," *Phys. Rev.*, vol. 153, no. 3, pp. 751–759, 1967.

[150] J. Hohlfeld, U. Conrad, J. G. Müller, S.-S. Wellershoff, E. Matthias, and K. H. Bennemann, "Nonlinear Optics in Metals," pp. 219–267, Oxford University, 1998.

[151] I. Nedelcu, R. W. Van De Kruijs, A. E. Yakshin, and F. Bijkerk, "Temperature-dependent nanocrystal formation in Mo Si multilayers," *Phys.*

Rev. B - Condens. Matter Mater. Phys., vol. 76, no. 24, pp. 1–8, 2007.

[152] A. Haase, V. Soltwisch, F. Scholze, and S. Braun, "Characterization of Mo/Si mirror interface roughness for different Mo layer thickness using resonant diffuse EUV scattering," *Opt. Syst. Des. 2015 Opt. Fabr. Testing, Metrol. V*, vol. 9628, p. 962804, 2015.

[153] J. Hrbek, D. G. van Campen, and I. J. Malik, "The early stages of ruthenium oxidation," *J. Vac. Sci. Technol. A Vacuum, Surfaces, Film.*, vol. 13, no. 3, pp. 1409–1412, 1995.

[154] H. Takase, S. Terashima, Y. Gomei, M. Tanabe, Y. Watanabe, T. Aoki, K. Murakami, S. Matsunari, M. Niibe, and Y. Kakutani, "Study of ruthenium-capped multilayer mirror for EUV irradiation durability," *Emerg. Lithogr. Technol. X*, vol. 6151, p. 615135, 2006.

[155] S. Bajt, H. N. Chapman, N. Nguyen, J. Alameda, J. C. Robinson, M. Malinowski, E. Gullikson, A. Aquila, C. Tarrio, and S. Grantham, "Design and performance of capping layers for extreme-ultraviolet multilayer mirrors," *Appl. Opt.*, vol. 42, no. 28, p. 5750, 2003.

[156] S. Bajt, Z. R. Dai, E. J. Nelson, M. A. Wall, J. Alameda, N. Nguyen, S. Baker, J. C. Robinson, J. S. Taylor, M. Clift, A. Aquila, E. M. Gullikson, and N. V. G. Edwards, "Oxidation resistance of Ru-capped EUV multilayers," *Emerg. Lithogr. Technol. IX*, vol. 5751, p. 118, 2005.

[157] P. J. van Zwol, D. F. Vles, W. P. Voorthuijzen, M. Péter, H. Vermeulen, W. J. van der Zande, J. M. Sturm, R. W. van de Kruijs, and F. Bijkerk, "Emissivity of freestanding membranes with thin metal coatings," *J. Appl. Phys.*, vol. 118, no. 21, 2015.

[158] C.-K. Sun, F. Vallée, L. H. Acioli, E. P. Ippen, and J. G. Fujimoto, "Femtosecond-tunable measurement of electron thermalization in gold," *Phys. Rev. B*, vol. 50, no. 20, p. 15337, 1994.

[159] G. Samsonov, *Handbook of the physicochemical properties of the elements*. IFI-Plenum, New York - Washington, 1968.

[160] K. Uozumi, T. Nakada, and A. Kinbara, "Sound velocity and internal friction in vacuum deposited gold films," *Thin Solid Films*, vol. 12, pp. 67–70, 1972.

[161] P. J. Wang, C. C. Shen, K. Y. Chou, M. H. Ho, J. K. Sheu, and C. K. Sun, "Studying time-dependent contribution of hot-electron versus lattice-induced thermal-expansion response in ultra-Thin Au-nanofilms," *Appl. Phys. Lett.*, vol. 117, no. 15, 2020.

[162] K. Y. Chou, C. L. Wu, C. C. Shen, J. K. Sheu, and C. K. Sun, "Terahertz Photoacoustic Generation Using Ultrathin Nickel Nanofilms," *J. Phys. Chem. C*, vol. 125, no. 5, pp. 3134–3142, 2021.

[163] C. Birleanu, M. Pustan, V. Merie, R. Müller, R. Voicu, A. Baracu, and S. Craciun, "Temperature effect on the mechanical properties of gold nano films with different thickness," *IOP Conf. Ser. Mater. Sci. Eng.*, vol. 147, no. 1, 2016.

[164] N. Medvedev and I. Milov, "Electron-phonon coupling in metals at high electronic temperatures," *Phys. Rev. B*, vol. 102, no. 6, pp. 1–22, 2020.

[165] I. Milov, I. A. Makhotkin, R. Sobierajski, N. Medvedev, V. Lipp, J. Chalupský, J. M. Sturm, K. Tiedtke, G. de Vries, M. Störmer, F. Siewert, R. van de Kruijs, E. Louis, I. Jacyna, M. Jurek, L. Juha, V. Hájková, V. Vozda, T. Burian, K. Saksl, B. Faatz, B. Keitel, E. Plönjes, S. Schreiber, S. Toleikis, R. Loch, M. Hermann, S. Strobel, H.-K. Nienhuys, G. Gwalt, T. Mey, H. Enkisch, and F. Bijkerk, "Mechanism of single-shot damage of Ru thin films irradiated by femtosecond extreme UV free-electron laser," *Opt. Express*, vol. 26, no. 15, p. 19665, 2018.

[166] M. Perner, S. Gresillon, J. März, G. Von Plessen, J. Feldmann, J. Porstendorfer, K. J. Berg, and G. Berg, "Observation of hot-electron pressure in the vibration dynamics of metal nanoparticles," *Phys. Rev. Lett.*, vol. 85, no. 4, pp. 792–795, 2000.

[167] Y. Petrov, K. Migdal, N. Inogamov, V. Khokhlov, D. Ilnitsky, I. Milov, N. Medvedev, V. Lipp, and V. Zhakhovsky, "Ruthenium under ultrafast laser excitation: Model and dataset for equation of state, conductivity, and electron-ion coupling," *Data Br.*, vol. 28, p. 104980, 2020.

[168] H. Gleiter, "Nanostructured materials: basic concepts and microstructure," *Acta Mater.*, vol. 48, no. 1, pp. 1–29, 2000.

[169] D. Stauffer and A. Aharony, "Introduction to Percolation Theory," CRC press, 2nd ed., 1994.

[170] D. I. Yakubovsky, Y. V. Stebunov, R. V. Kirtaev, G. A. Ermolaev, M. S. Mironov, S. M. Novikov, A. V. Arsenin, and V. S. Volkov, "Ultrathin and Ultrasmooth Gold Films on Monolayer MoS2," *Adv. Mater. Interfaces*, vol. 6, no. 13, pp. 2–7, 2019.

[171] G. Ramakrishnan and P. C. M. Planken, "Percolation-enhanced generation of terahertz pulses by optical rectification on ultrathin gold films," *Opt. Lett.*, vol. 36, no. 13, p. 2572, 2011.

[172] D. K. Polyushkin, E. Hendry, and W. L. Barnes, "Controlling the generation of THz radiation from metallic films using periodic microstructure," *Appl. Phys. B*, vol. 120, no. 1, pp. 53–59, 2015.

[173] M. Breit, G. Von Plessen, J. Feldmann, S. Grésillon, J. C. Rivoal, P. Gadenne, V. A. Podolskiy, A. K. Sarychev, and V. M. Shalaev, "Experimental observation of percolation-enhanced nonlinear light scattering from semicontinuous metal films," *Phys. Rev. B*, vol. 64, no. 12, p. 125106, 2001.

[174] V. M. Shalaev and A. K. Sarychev, "Nonlinear optics of random metal-dielectric films," *Phys. Rev. B*, vol. 57, no. 20, pp. 265–288, 1998.

[175] P. Gadenne, Y. Yagil, and G. Deutscher, "Transmittance and reflectance in situ measurements of semicontinuous gold films during deposition," *J. Appl. Phys.*, vol. 66, no. 7, pp. 3019–3025, 1989.

[176] Y. Yagil, P. Gadenne, C. Julien, and G. Deutscher, "Optical properties of thin semicontinuous gold films over a wavelength range of 2.5 to 500 μm," *Phys. Rev. B*, vol. 46, no. 4, pp. 2503–2511, 1992.

[177] M. Walther, D. G. Cooke, C. Sherstan, M. Hajar, M. R. Freeman, and F. A. Hegmann, "Terahertz conductivity of thin gold films at the metal-insulator percolation transition," *Phys. Rev. B*, vol. 76, no. 12, pp. 1–9, 2007.

[178] G. Dumpich, S. Friedrichowski, and P. Mikitisin, "Electron transport in percolating gold films," *Thin Solid Films*, vol. 281, no. 1-2, pp. 368–371, 1996.

[179] G. T. Boyd, T. Rasing, J. R. R. Leite, and Y. R. Shen, "Local-field enhancement on rough surfaces of metals, semimetals, and semiconductors with the use of optical second-harmonic generation," *Phys. Rev. B*, vol. 30, no. 10, pp. 519–526, 1984.

[180] J. Hernandez-Rueda, A. de Beurs, and D. van Oosten, "Ultrafast laser ablation of trapped gold nanoparticles," *Opt. Lett.*, vol. 44, no. 13, p. 3294, 2019.

[181] J. Hernandez-Rueda, J. Clarijs, D. Van Oosten, and D. M. Krol, "The influence of femtosecond laser wavelength on waveguide fabrication inside fused silica," *Appl. Phys. Lett.*, vol. 110, no. 16, p. 161109, 2017.

[182] J. Hernandez-Rueda and D. van Oosten, "Transient scattering effects and electron plasma dynamics during ultrafast laser ablation of water," *Opt. Lett.*, vol. 44, no. 7, p. 1856, 2019.

[183] M. Vreugdenhil, D. van Oosten, and J. Hernandez-Rueda, "Dynamics of

femtosecond laser-induced shockwaves at a water/air interface using multiple excitation beams," *Opt. Lett.*, vol. 43, no. 20, p. 4899, 2018.

[184] D. Von Der Linde and K. Sokolowski-Tinten, "Physical mechanisms of short-pulse laser ablation," *Appl. Surf. Sci.*, vol. 154, pp. 1–10, 2000.

[185] B. Rethfeld, D. S. Ivanov, M. E. Garcia, and S. I. Anisimov, "Modelling ultrafast laser ablation," *J. Phys. D. Appl. Phys.*, vol. 50, no. 19, 2017.

[186] B. Y. Mueller and B. Rethfeld, "Relaxation dynamics in laser-excited metals under nonequilibrium conditions," *Phys. Rev. B*, vol. 87, no. 3, p. 035139, 2013.

[187] M. Kaganov, E. Lifshitz, and L. Tanatarov, "Relaxation between electrons and the crystalline lattice," *Sov. Phys. Jetp-Ussr*, vol. 4, no. 2, pp. 173–178, 1957.

[188] S. D. Brorson, A. Kazeroonian, J. S. Moodera, D. W. Face, T. K. Cheng, E. P. Ippen, M. S. Dresselhaus, and G. Dresselhaus, "Femtosecond room-temperature measurement of the electron-phonon coupling constant in metallic superconductors," *Phys. Rev. Lett.*, vol. 64, no. 18, pp. 2172–2175, 1990.

[189] B. N. Chichkov, C. Momma, S. Nolte, F. Von Alvensleben, and A. Tünnermann, "Femtosecond, picosecond and nanosecond laser ablation of solids," *Appl. Phys. A*, vol. 63, no. 2, pp. 109–115, 1996.

[190] R. W. Schoenlein, W. Z. Lin, J. G. Fujimoto, and G. L. Eesley, "Femtosecond studies of nonequilibrium electronic processes in metals," *Phys. Rev. Lett.*, vol. 58, no. 16, pp. 1680–1683, 1987.

[191] D. R. Queen and F. Hellman, "Thin film nanocalorimeter for heat capacity measurements of 30 nm films," *Rev. Sci. Instrum.*, vol. 80, no. 6, 2009.

[192] V. M. Shalaev, "Nonlinear Optics of Random Media," Springer, 2000.

[193] V. M. Shalaev, "Optical Properties of Nanostructured Random Media," Springer, 2002.

[194] Z. Lin, L. V. Zhigilei, and V. Celli, "Electron-phonon coupling and electron heat capacity of metals under conditions of strong electron-phonon nonequilibrium," *Phys. Rev. B*, vol. 77, no. 7, pp. 1–17, 2008.

[195] C. Fourment, F. Deneuville, D. Descamps, F. Dorchies, S. Petit, O. Peyrusse, B. Holst, and V. Recoules, "Experimental determination of temperature-dependent electron-electron collision frequency in isochorically heated warm

dense gold," *Phys. Rev. B*, vol. 89, no. 16, pp. 1–5, 2014.

[196] A. N. Smith and P. M. Norris, "Influence of intraband transitions on the electron thermoreflectance response of metals," *Appl. Phys. Lett.*, vol. 78, no. 9, pp. 1240–1242, 2001.

[197] B. Rethfeld, V. V. Temnov, K. Sokolowski-Tinten, P. Tsu, D. von der Linde, S. I. Anisimov, S. I. Ashitkov, and M. B. Agranat, "Superfast thermal melting of solids under the action of femtosecond laser pulses," *J. Opt. Technol.*, vol. 71, no. 6, p. 348, 2010.

[198] J. K. Chen, W. P. Latham, and J. E. Beraun, "The role of electron-phonon coupling in ultrafast laser heating," *J. Laser Appl.*, vol. 17, no. 1, pp. 63–68, 2006.

[199] J. Yang, Y. Zhao, and X. Zhu, "Theoretical studies of ultrafast ablation of metal targets dominated by phase explosion," *Appl. Phys. A*, vol. 89, no. 2, pp. 571–578, 2007.

[200] C. Kittel, "Introduction to Solid State Physics," John Wiley & Sons, 6th ed., 1986.

[201] D. Perez and L. J. Lewis, "Molecular-dynamics study of ablation of solids under femtosecond laser pulses," *Phys. Rev. B*, vol. 67, no. 18, pp. 1–15, 2003.

[202] P. Lorazo, L. J. Lewis, and M. Meunier, "Thermodynamic pathways to melting, ablation, and solidification in absorbing solids under pulsed laser irradiation," *Phys. Rev. B*, vol. 73, no. 13, pp. 1–22, 2006.

[203] A. Miotello and R. Kelly, "Laser-induced phase explosion: New physical problems when a condensed phase approaches the thermodynamic critical temperature," *Appl. Phys. A*, vol. 69, no. 7, pp. 67–73, 1999.

Summary

Enhanced generation and detection of ultrafast laser-induced acoustic signals

The semiconductor manufacturing industry is continuously trying to increase the number of electrical components that fit on computer chips in order to keep fulfilling Moore's empirical law. Therefore, recently, chip manufacturers started stacking computer chips on top of each other, creating three-dimensional stacks of integrated circuits. During the fabrication of these multi-layer structures, it is crucial that all layers are electrically connected with each other via vertical interconnects. Therefore, accurate alignment of the wafer, on which the electrical components are fabricated, with respect to the illumination source is crucial for the functionality of the chips. To align the wafer so-called "alignment markers" are etched in the bottom layer of the wafer. Optical detection of these alignment markers allows for accurate positioning of the wafer. However, the alignment markers are buried beneath the layers which form the three-dimensional stack of computer chips. After a few (possibly opaque) layers, the alignment markers are no longer optically visible and therefore alignment of the wafer cannot occur. Therefore, as of now, this technique is not suitable for high-volume manufacturing

To overcome this issue, it has been proposed to use laser-induced sound waves to detect the optically buried alignment markers. An ultrashort high-intensity laser pulse illuminates the top surface of the multi-layer stack, which results in the excitation of an acoustic wave inside the sample. The acoustic wave travels through the entire multi-layer stack and reflects off the buried alignment marker. Here, the acoustic wave copies the shape of the alignment marker such that the wavefront of the acoustic wave resembles that of the alignment marker. The acoustic replica of the marker travels back to the top surface where, for a short amount of time,

it deforms the surface in the same spatially periodic manner as the alignment marker. The acoustic replica of the alignment marker can then be optically detected, resulting in an indirect detection of the buried alignment marker. Despite the proven functionality of this technique, a major downside is the fact that the signal strength caused by the acoustic replica of the buried alignment marker is too low for practical applications.

In this thesis, we focus on techniques to enhance the detection and generation of acoustic waves. This thesis can be split into three parts. The first part is described in Chapters 4 & 5. Here we employ a surface plasmon polariton resonance on a gold grating to enhance the detection (Chapter 4) and the generation (Chapter 5) of the acoustic waves. In Chapter 4 we show how the surface plasmon polariton resonance wavelength shifts due to acoustic-wave-induced perturbations of the electron density and grating geometry changes, resulting in strong reflection changes. In Chapter 5 we demonstrate the efficient excitation of acoustic waves by increasing the absorption of the incident light via the surface plasmon polariton resonance. Furthermore, we demonstrate a non-linear increase of the measured signal strength as a function of laser power. This is tentatively attributed to non-linear strain-induced changes of the interband transition threshold from the d-band to the s/p of gold.

The second part of this thesis is described in Chapter 6, here we show the generation of extremely high-frequency acoustic waves in thin layers of ruthenium using the transient grating technique. Similar to optical imaging, the feature size that can be detected using acoustic waves is related to the frequency of the acoustic wave. By increasing the frequency of the acoustic waves, smaller features can be detected. Therefore, we demonstrate how we are able to launch acoustic waves with frequencies of several hundreds of gigahertz on thin Ruthenium layers, with thicknesses ranging from 1.2 nm to 107 nm. We found that, for thin Ruthenium layers, the speed of sound is a strong function of the layer thickness. Furthermore, back-extrapolation of the signal starting from t = 2 ps to t = 0 ps results in an apparent starting phase of $-\pi/2$, which would suggest a non-zero acoustically induced diffraction efficiency at the moment of excitation. As this seems rather unlikely, we speculate that the phase/frequency of the strain wave undergoes dynamic changes in the first 2 ps, due to high lattice temperatures.

One way to generate even stronger acoustic waves would be to simply increase the pump fluence. However, at a certain point, the sample starts to damage due to the increasing pump intensity. Therefore, in the third part and final part of this thesis, described in Chapter 7, we investigate laser-induced damage to nanostructured gold. Here, we show transient pump-probe reflection and transmission measurements during ablation of the gold. Furthermore, we show scanning elec-

tron microscope and optical microscope analysis of the laser-induced crater. We demonstrate that, within 150 ps, the reflection and transmission reach the substrate values, indicating that the gold layer has become optically transparent. We calculate that the absorbed amount of energy exceeds the cohesive energy of the gold atoms, leading to the process of rapid vaporization. Furthermore, we demonstrate that the ablation threshold for nano-structured gold is approximately two orders of magnitude lower than that of continuous gold.

In short, this thesis demonstrates techniques to increase the photo-acoustic signal strength. Both enhanced detection and enhanced excitation using a surface plasmon polariton resonance have been shown. We also demonstrate the ability to generate extremely high-frequency acoustic waves using thin metal layers. Furthermore, high-power laser-induced damage on nanostructured gold has been investigated to better understand the damage mechanism, which is a limiting factor in the excitation of high amplitude acoustic waves.

Samenvatting

Verbeterde generatie en detectie van ultrasnelle laser-geïnduceerde akoestische signalen

De halfgeleiderindustrie is continu bezig met het verhogen van het aantal elektrische componenten dat op een computerchip past, om zo te blijven voldoen aan de empirische wet van Moore. Het is daarom dat, recentelijk, computerchip fabrikanten begonnen zijn met het op elkaar stapelen van computerchips om zo driedimensionale lagen te maken van geïntegreerde schakelingen. Tijdens de fabricage van deze meerlaagse structuren is het cruciaal dat alle lagen elektronisch met elkaar verbonden worden door middel van verticale elektrische connecties. Daarom is het belangrijk voor de functionaliteit van de computerchips dat de wafer, waarop de elektrische componenten gefabriceerd worden, extreem nauwkeurig wordt uitgelijnd ten opzichte van de lichtbron. Om de wafer uit te lijnen bevinden er zich zogeheten *uitlijnmarkeringen* op de onderste laag van de wafer. De wafer kan nauwkeurig worden uitgelijnd na optische detectie van deze uitlijnmarkeringen. Er ontstaat alleen een probleem bij meerlaagse structuren, hierbij worden de uitlijnmarkeringen namelijk begraven onder alle lagen die de gebruikt worden in driedimensionale chips. Na een paar lagen, waarvan sommige zelfs volledig ondoorzichtbaar zijn voor licht, kunnen de uitlijnmakeringen niet meer waargenomen worden en kan de wafer niet worden uitgelijnd.

Om dit probleem op te lossen, is het voorgesteld om laser-geïnduceerde akoestische golven te gebruiken om de optisch begraven uitlijnmarkeringen te detecteren. Hierbij wordt de bovenkant van de meerlaagse structuur belicht met een ultrasnelle hoog intensiteit laser puls. Dit zorgt ervoor dat er een akoestische golf wordt gelanceerd in de meerlaagse structuur. Deze akoestische golf reist door de gehele

structuur heen richting de onderkant en reflecteert terug naar het oppervlak via de uitlijnmarkering. Tijdens deze akoestische reflectie neemt de akoestische golf de vorm over van de uitlijnmarkering, waardoor het golffront van de akoestische golf lijkt op de uitlijnmarkering. Deze akoestische kopie van de uitlijnmarkering reist terug naar het oppervlak waar het, gedurende een hele korte tijd, het oppervlak vervormd naar de vorm van de uitlijnmarkering. De akoestische replica van de uitlijnmarkering kan dan vervolgens optisch gedetecteerd worden, waarna de wafer uitgelijnd kan worden. Ondanks het feit dat het is aangetoond deze techniek werkt, is een groot nadeel dat de optische signaalsterkte van de akoestische kopie van de uitlijnmarkering erg zwak hier. Hierdoor is deze techniek, voor alsnog, niet geschikt voor commerciële/industriële toepassingen.

In dit proefschrift focussen we op technieken om de detectie en generatie van akoestische golfen te verbeteren. Dit proefschrift kan opgesplits worden in drie delen. Het eerste deel wordt beschreven in Hoofdstuk 4 & 5. Hier laten we zien hoe we de detectie (Hoofdstuk 4) en generatie (Hoofdstuk 5) van akoestische golven kunnen versterken door gebruik te maken van een oppervlakteplasmon polariton resonantie. In Hoofdstuk 4 laten we zien hoe de oppervlakteplasmon polariton resonantie golflengte schuift door akoestisch geïnduceerde verstoringen van de electron dichtheid en veranderingen in de tralie geometrie, wat resulteert in sterke reflectie veranderingen. In Hoofdstuk 5 demonstreren we efficiënte excitatie van akoestische golven door oppervlakteplasmon polariton versterkte absorptie van de excitatie laser puls. Verder laten we zien dat er een niet-lineair verband is tussen de gemeten signaalsterkte en het excitatie vermogen. Dit wordt, vooralsnog, toegeschreven aan niet-lineaire veranderingen van de interband overgang energie van de d-band naar de s/p-band van het goud ten gevolge van de akoestische golf.

Het tweede deel van dit proefschrift wordt beschreven in Hoofdstuk 6, waar er wordt besproken hoe hoogfrequente akoestische golven worden opgewekt in extreem dunne lagen rutheen gebruikmakend van de ”transient grating”techniek. Net als bij optische beeldvorming wordt de detectie resolutie van de akoestische golven bepaald door de frequentie van de akoestische golf. Golven met een hogere frequentie kunnen kleinere structuren waarnemen. We laten zien dat, door gebruik te maken van rutheen lagen met een dikte van 1.2 nm tot 107 nm, we akoestische golven kunnen opwekken met frequenties van honderden gigahertz. Hierbij hebben we gevonden dat, voor extreem dunne rutheen lagen, de geluidsnelheid sterk afhankelijk is van de laagdikte. Verder heeft terug extrapolatie van de tijdsafhankelijke response van t = 2 ps naar t = 0 ps tot een schijnbare start fase van de akoestische golf van $-\pi/2$ geleid. Dit zou betekenen dat er akoestisch geïnduceerde diffractie plaats vindt direct na excitatie. Aangezien dit zeer onwaarschijnlijk is, speculeren we dat de fase/frequentie van de akoestische golf dynamisch veranderd

in de eerste twee picoseconden ten gevolge van de hoge roostertemperatuur.

Een eenvoudige manier om nóg sterkere akoestische golven te maken is door simpelweg het pomp vermogen te verhogen. Alhoewel dit inderdaad resulteert in sterkere akoestische golven, zal op gegeven moment het materiaal beschadigd worden door de hoge pomp intensiteit. Daarom bestuderen we in het laatste hoofdstuk van dit proefschrift, Hoofdstuk 7, hoe laser geïnduceerde schade plaatsvindt aan nanogestructureerde lagen goud. We laten pomp-probe metingen zien waarin we de tijdsafhankelijke transmissie en reflectie meten van goud gedurende het beschadigingsproces. Daarbij laten we ook elektronenmicroscopie en optische microscopie beelden zien van de laser-geïnduceerde krater. We ondervinden dat de reflectie en transmissie binnen 150 ps gelijk zijn aan de reflectie en transmissie van het substraat. Dit betekent dat de nanogestructureerde goud laag optisch transparant is geworden. We hebben berekend dat de geabsorbeerde hoeveelheid energie groter is dan de energie die de goud atomen bij elkaar houdt. Dit resulteert in zogeheten ultrasnelle verdamping. De gemeten schade drempel van het nanogestructureerde goud is ongeveer twee ordes van grootte kleiner dan die van continu goud.

Samenvattend, in dit proefschrift laten we technieken zien die de foto-akoestische signaalsterkte vergroten. Zowel versterkte detectie als generatie van de akoestische golven door middel van oppervlakte plasmonen is gedemonstreerd. Verder laten we ook zien hoe extreem hoogfrequente akoestische golven opgewekt kunnen worden in dunne laagjes rutheen. Tenslotte bestuderen we laser-geïnduceerde schade aan nanogestructureerd goud om zo beter begrip te krijgen van laser schade, wat momenteel een limiterende factor is voor de generatie van sterke akoestische golven.

Acknowledgements

First and foremost, I would like to extend my deepest gratitude to my supervisor, Paul Planken. Paul, I met you when I came to ARCNL for the first time for an open house day, where you gave a tour of the lab. I remember talking with you afterward at the coffee machine and we immediately hit it off. Shortly after, I decided that I wanted to do my master's internship in your group, which eventually evolved into my PhD. During the four years of my PhD, I have thoroughly enjoyed working with you, during which I have learned so much from you. I like to think that sometimes I taught you a thing or two as well. You were always there for me when I needed you, giving me confidence when I was insecure and keeping me on track when I got distracted. I will always remember the discussions we had about physics, politics, and life in general. Paul, you truly are and always will be a mentor to me. Thank you for everything.

Nishant, Vanessa, Stephen, and Nick, you were the people who took care of me when I first joined the group during my master's internship. Nishant, to this day I still remember the look on your face when I first put on Justin Bieber's *baby* in the lab, it was priceless. Vanessa, thank you for making me feel at home and part of the group. I really enjoyed working closely together with you during the final stage of your PhD. You are an amazing person, never change. Stephen, you always rose to the occasion when I asked for your help both in and outside of the lab. I will always respect that in you, thank you for your patience and your assistance. Nick, you were my supervisor during my master's internship, you taught me the ropes and helped me understand complex machinery with ease. Seldom have I met someone with such a brilliant mind, and up until the last day of my PhD, I have used the three-layer model you so expertly developed. Wherever you are, I hope you found what you were looking for.

A big part of doing a PhD is that people are always coming and going. Where I saw Nishant, Vanessa and Stephen leave, I also saw Thomas v/d H., Ester, and Lorenzo coming. I have worked with the three of you for the past year and I am

grateful for getting to know each one of you. Thomas v/d H., you are my direct successor and I have spent many hours in the lab training you, similarly as how Nick trained me. I can leave my setup comfortably in your hands, knowing that you will only improve upon it. Not only did I enjoy spending time with you in the lab, but also outside of the lab. Numerous beers have been drunk, and many more will surely follow. Ester, what a great and amazing person you are. Always up for coffee and social activities, chatting my ears off and telling me amazing stories. I have no doubt you will succeed in what you are doing and whatever comes next in life. Lorenzo, my Italian buddy, you always make me laugh. I will never forget how, during one of our online group meetings, I noticed that you were sitting in the bathroom because of the typical bathroom tiles behind you. You sat there because your girlfriend had an important online meeting in the living room, or so you want us to believe.

The last, but definitely not the least, member of our group is Thomas M., our group technician. You were there from the start of my time at ARCNL up until the end. I have shared joy and sorrow with you, I have seen you laugh and cry, as you have seen me laughing and crying. I do not think that in the entire world there are two people who are as different in almost everything as you and me. Nevertheless, a great friendship formed which I will cherish and maintain. Thank you for your kindheartedness and openness, you will forever make your mother proud.

Besides the people in our group, there are a lot of people who made my PhD possible. Rudolf Sprik, my co-promotor. Thank you for being as involved in my PhD as you were, both in the structure of my PhD as in the content of my PhD. You always made me think twice. Irwan Setija, you were my ASML liaison during the phases of my PhD when collaboration with ASML peaked. Never before, have I spent so much time counting samples and meticulously keeping track of them as with you. Thank you for all your insights and for being part of my committee. Auréle Adam, as a co-author of one of my papers you have contributed directly to my PhD, for which I would like to thank you deeply. Not only that but you are also part of my committee, for which I would like to say: merci beaucoup. I would also like to thank the rest of my committee, Erik van Heumen, Huib Bakker, Ben van Linden van den Heuvell and Klaasjan van Druten, who so selflessly decided to spend their time on me. A special thanks goes out to Klaasjan, who has become a part-time member of our group and a very pleasant conversational partner.

An institute such as ARCNL can simply not function without a lot of behind the screens work. For this, I would like to thank Joost, our director, for your unparalleled passion for physics and our shared passion for running. Marjan, our institute manager, thank you for always keeping your door open for me and giving

me advice when I needed it. I would also like to thank the people of the secretariat, Romy, Rosa, Cathelijne, and Marja for their hard work, ARCNL would simply stop existing without you. Thank you as well to all ARCNL technicians, Nick, Laurens, Arend-Jan, Mark, and Bartjan for always helping me out when I asked for it. A special thanks go out to one technician in particular, Reinout. I will never forget your deep appreciation for everything green and beautiful. May you rest in peace.

It is not only staff from ARCNL that made my work possible, a lot of people at our sister institute AMOLF played a crucial role as well. I want to thank all the people from the cleanroom, Andries, Dimitry, Bob, Igor, and Hans. You guys are simply a pleasure to work with. I want to thank Marco for the thousands of lines of code he wrote to make my experiments work and Duncan and Pepijn for everything electronics-related. A general thanks goes out to all the people in HR, the purchasing department, finance, and the facility departments. Besides the people at AMOLF, I would also like to thank other external collaborators such as Dries and Javier, for teaching me everything they know about laser-induced damage. I would also like to thank Alexander Franzen for publicly sharing his Inkscape optical component library. A special thanks goes out to Hao Zhang for so generously sharing your acoustic model and running simulations for me.

It are the people at ARCNL who make the institute into what it is today. So many kind and warm people, you all made my stay at ARCNL a true blessing. Thank you Sylvianne, for our endless foosball games, I had so much fun with you. Ruben, my German partner in crime, drinking beers and hanging out with you was such a blast. Thank you for all the bad jokes, you still owe me a bike. Neha, even though no one has ever butchered my name as you have, we still bonded over hours of drinking coffee and complaining about PhD life. Thank you ever so much for providing me with AFM tech support when I called. John, my Irish friend, what a guy you are. Our opinion on the Irish women may be different, but we bonded nevertheless. Thank you for your humor and I hope that someday you will fix that screen of yours. A thanks goes out to everyone else at ARCNL who made me feel at home: Ale, Maisie, Lars L., Lars B., Joris, Victor, Najmeh, Filippo, Maarten, Maksym and Görsel.

Of course, the people at ARCNL kept me going, but if it wasn't for my friends I don't know what would have happened. Therefore, I want to deeply thank everyone from the ATLP, my oldest and closest friends. Derk, Daan, Youp, Timo, Martijn, Erik, Matthijs, Jessy, and Danny, thank you all for keeping me with both of my feet on the ground and for being there for me, unconditionally. Derk, you, and of course your girlfriend Marinda, are one the most important people in my life. You were there when things went bad and you helped me back up on my feet when I needed it. Besides that, you are such a joy to be around and one of the

most selfless people I know. I love hanging out with you, shooting zombies, and discussing life at our (dinner-)parties. Jessy, one of my best friends, you helped me relax in times of stress and always gave me the best advice when I had to make hard choices. You always make me push myself to my limits and never let me give up. Not only that but there is no one with whom I'd rather go dancing and partying than with you. Martijn, you are the guy with a heart of gold. You are always listening to me whine and moan and you never complain. You were always there to reassure me and calm me down when I got worked up about something, you're an amazing friend. Daan, without a single doubt, you are the friend who makes me laugh the most. Your silly voices and clever remarks always crack me up and I love spending time with you. I enjoy our deep conversations about life, love, family, work, and everything else just as much as I enjoy watching memes with you. I want to thank you all, for making my PhD possible, I could not have done it without you. I love you all.

Apart from my friends from the ATLP, there are a few more people who I would like to personally thank. One of whom is ofcourse Sophie. With you, I don't even know where to start. You are such a wonderful person and truly forever one of my best friends. You and I can forever complain about PhD life and everything around it. But nevertheless, you have stuck with me through thick and thin. Whenever life is beating me down, you are there to invite me over for drinks and offer great company. Countless hangovers and late nights have your name written all over it, thank you, honestly. Jim & Nick, my friends whom I met at the University during our studies. Thank you for everything you've done for me and all of the support you provided me, during my PhD and my time at university. Up until this day, I still enjoy hanging out with you guys.

Friends are an important part of my life, but next to friends, my family plays an equally important role in my life. I am lucky to have not two, but four amazing parents. My mother Saskia, my father Roy, and my bonus-parents Svante and Marjan. I want to thank all of you, for making me into the person I am today. All of you have taught me the things in life I needed to accomplish what I have. I want to thank my dad for always having faith in me and for your unconditional support. Many of the people around me know that I am a bit of a momma's boy, this is indeed *absolutely* true. It is therefore, that I would like to extend a special thanks to my mom. Knowing that, no matter what happens, I can always come home to you.

Next to my parents, I would like to thank my brother and sister, David and Tessa. You are the best brother and sister one could ask for. David, you are the true pinnacle of relaxation. Your attitude of "everything will be alright" has been really helpful in times when I was stressed. Our deep night gaming sessions are a prime

example of how you showed me that I can take time for myself. A special thanks also goes out to your girlfriend, Minke, who is always very passionate at our board game nights. Tessa, my sweet baby sister, thank you for all the amazing parties we went to. You helped me unwind when I was tensed and are always dancing through the night with me. I hope that many more nights of dancing will follow.

A well-deserved thank you is also appropriate for my cousin, neighbor, and friend, Koen. When we were children we bonded over our shared passion for science and everything beta. Later in life, we bonded even more on almost everything else. Thank you for your listening ear during the past 4 years. I want to thank my bonus brothers, Sjoerd, Michiel, and Joris, for hanging out, gaming, and our famous burgers and beer nights. Thank you Jan H., for keeping me motivated to stay physically fit during my PhD. I hope that we may run many more marathons together, and maybe one day I'll finish before you. I also want to thank my family-in-law, Jan K., Wilma, Nina, and Jeroen, for so openly and warmly inviting and accepting me into your family.

And finally, Fleur, the love of my life. It was partially thanks to my PhD that we met in the Bukowski that one famous night. Ever since, you have been the greatest pillar of support anyone could wish for. Thank you for always believing in me, even when I didn't. Thank you for listening to me, talking to me, and being there for me. There have been times where I wanted to just simply give up, but you would not let me. You inspired me to push through and never give up. Thank you for all the times of endless laughter and storytelling. Thank you for playing such an important role in my life. I cannot wait to see what the future has in store for us. Together, we can accomplish anything. Thank you.